E.O. Paton Electric Welding Institute of the National Academy of Sciences of Ukraine

International Scientific-Technical and Production Journal

The Paton WELDING JOURNAL

Issue 3
2021

Published Monthly Since 2000

English Translation of the Monthly «Avtomatychne Zvaryuvannya» (Avtomaticheskaya Svarka/Automatic Welding) Journal Published in Ukrainian and Russian Since 1948

Founders
E.O. Paton Electric Welding Institute
International Association «Welding»

Publisher
International Association «Welding»

Translators
A.O. Fomin, I.M. Kutianova
Editor
N.G. Khomenko
Electron galley
D.I. Sereda, T.Yu. Snegiryova

Address
E.O. Paton Electric Welding Institute,
International Association «Welding»
11 Kazymyr Malevych Str. (former Bozhenko),
03150, Kyiv, Ukraine
Tel.:/Fax: (38044) 200 82 77
E-mail: journal@paton.kiev.ua
www://patonpublishinghouse.com/eng/journals/tpwj

State Registration Certificate
KV 4790 of 09.01.2001
ISSN 0957-798X
DOI: http://dx.doi.org/10.37434/tpwj

Subscriptions
12 issues per year, back issues available.
$384, subscriptions for the printed (hard copy) version, air postage and packaging included.
$312, subscriptions for the electronic version (sending issues of Journal in pdf format or providing access to IP addresses).
Institutions with current subscriptions on printed version can purchase online access to the electronic versions of any back issues that they have not subscribed to.
Issues of the Journal (more than two years old) are available at a substantially reduced price.

CONTENTS

SCIENTIFIC AND TECHNICAL

INDUSTRIAL

https://doi.org/10.37434/tpwj2021.03.01

FATIGUE LIFE OF STEEL 40Kh SPECIMENS AFTER WEAR-RESISTANT SURFACING WITH A SUBLAYER OF LOW-CARBON STEEL

I.O. Ryabtsev, V.V. Knysh, A.A. Babinets and **S.O. Solovej**
E.O. Paton Electric Welding Institute of the NAS of Ukraine
11 Kazymyr Malevych Str., 03150, Kyiv, Ukraine. E-mail: office@paton.kiev.ua

The resistance to fatigue fracture of steel 40Kh after wear-resistant surfacing using PP-Np-25Kh5FMS flux-cored wire with a sublayer of a low-carbon ductile material formed by Sv-08A wire was investigated. The design of the deposited specimens and the procedure of their testing simulated operating conditions of the mill rolls, for surfacing of which PP-Np-25Kh5FMS flux-cored wire is widely used. A comprehensive procedure for evaluating the resistance of multilayer material to fatigue fracture included three stages: determination of cyclic life of specimens after manufacturing surfacing; study of cyclic crack resistance of different metal layers; determination of fatigue life of specimens, which in the course of preliminary tests had fatigue cracks in the deposited layer after repair surfacing. It was established that the cyclic life of the specimens of carbon steel 40Kh, deposited using PP-Np-25Kh5FMS flux-cored wire with a sublayer of low-carbon steel 08kp (rimmed) exceeds the cyclic life of the specimens deposited without a sublayer, approximately by 2 times. The maximum values of stress intensity factor (SIF) (140–180 MPa√m) obtained on the specimens with a multilayer surfacing with a sublayer, are 2–3 times higher than the maximum values of SIF obtained on the specimens without a sublayer, which indicates the rationality of using a low-carbon sublayer to increase the crack resistance of a multilayer material with wear-resistant surfacing. It was shown that performance of repair surfacing according to the scheme of removal and a subsequent remelting of only areas of the metal with fatigue cracks of long-term operating parts does not lead to a significant increase in the cyclic life after repair. This is related to the fact that after long operation, the defect-free layer of deposited metal has a significant level of accumulated fatigue damages. Therefore, to increase the efficiency of repair surfacing, it is recommended to remove not only the metal around the detected fatigue cracks, but the entire deposited layer to the depth of detected fatigue cracks with the subsequent restoration surfacing. 18 Ref., 4 Tables, 7 Figures.

K e y w o r d s : arc surfacing, repair surfacing, ductile sublayer, fatigue life, fatigue cracks, stress intensity factor

Most parts and units of industrial equipment of metallurgical and machine-building industries are operated under the conditions of variable cyclic load [1]. One of such parts is rolls of rolling mills which, depending on operating modes, fail as a result of fatigue, surface wear or combination of the mentioned factors. For example, the rolls of breakdown mills are exposed to thermal fatigue, which leads to the appearance of a grid of small cracks on the surface of rolls, which can further propagate as fatigue cracks. It is difficult to predict the moment of origination and the rate of propagation of defects of such type, so it can lead to the fracture of a roll [1–6]. Annually, on replacement of worn parts and elements of equipment up to 5–30 % from the total cost of manufactured products is spent [5]. This indice can be reduced by extending the life of damaged large-size parts due to repair and restoration works with the use of surfacing the metal layer with improved service properties relative to the base metal.

The technology of manufacturing or repair surfacing can be performed both without surfacing of the intermediate metal layer (sublayer) as well as with it. Thus, in [7], the data on the technology of surfacing specimens of carbon steel 40Kh, simulating the design of a rolling mill, with the use of flux-cored wire PP-Np-25Kh5FMS without a sublayer are given. The authors experimentally established the cyclic life and characteristics of crack resistance of the metal of the deposited specimens. However, it is known that to improve weldability of the base and wear-resistant metal, as well as to reduce residual stresses, it is rational to perform a preliminary surfacing of a sublayer on the base metal with an intermediate value of the thermal expansion coefficient. For this purpose, often surfacing of the intermediate layer of low-carbon and low-alloy materials of type Sv-08A, Sv-08G2S, etc. is used. [8]. To determine the most effective surfacing technology (with or without a sublayer) it is necessary to conduct a comparative evaluation of fatigue life of

I.O. Ryabtsev — https://orcid.org/0000-0001-7180-7782, V.V. Knysh — https://orcid.org/0000-0003-1289-4462,
A.A. Babinets — https://orcid.org/0000-0003-4432-8879, S.O. Solovej — https://orcid.org/0000-0002-1126-5536

multilayer deposited parts and specimens with and without a sublayer.

The calculated determination of fatigue life of multilayer deposited parts is quite complicated. This is explained by several factors. First, surfacing of several layers of the metal different as to chemical composition leads to a complex stress state in multilayer specimens. For example, as a result of redistribution of stresses during surfacing of subsequent layers of metal, the initially obtained residual compressive stresses can be converted into tensile stresses, which negatively affect the fatigue life [2, 9]. Secondly, with an increase in the number of deposited beads and/or layers on the base metal, the probability of formation of such single defects as pores, inclusions, slags, etc., which significantly reduce the fatigue life, increases [10–12]. Therefore, to establish the rationality of using a metal sublayer during surfacing in order to increase the life of multilayer deposited specimens, it is more rational to use experimental procedures for evaluation of fatigue life.

Thus, the aim of this work is an experimental study of the influence of materials and technologies of manufacturing and repair surfacing of wear-resistant working layer and sublayer on the fatigue life of multilayer deposited parts.

Procedures, technologies and investigation materials. To establish the rationality of using a metal sublayer during surfacing in order to increase the fatigue life of multilayer deposited specimens, the technology of surfacing specimens without a sublayer was used, which is described in detail in [7, 13]. The main stages of technology of producing deposited specimens are: preheating of billets of steel 40Kh to 250–300 °C; at first, automatic arc surfacing of a sublayer material with a total thickness of 4–5 mm and a wear-resistant layer with a thickness of ≈ 6 mm; slowered cooling of deposited specimens together with the furnace.

The steel grades of the base metal and the deposited wear-resistant metal layer (steel 40Kh and 25Kh5FMS, respectively) were identical during surfacing of the specimens without a sublayer and with a sublayer. For surfacing of the intermediate layer, a solid low-carbon wire Sv-08A was used, and for surfacing of the wear-resistant layer, flux-cored wire PP-Np-25Kh5FMS with the diameters of 1.8 mm was used. The surfacing mode for all the specimens was the same: I = 220–250 A; U = 26–28 V; V = 18 m/year; beads overlapping ≈ 50 %. According to the abovementioned technology, 3 series of prismatic specimens with dimensions of 350×40×20 mm with the quantity of 3–5 specimens in each series were made. The chemical composition and mechanical properties of the materials used in the work are given in Tables 1 and 2 [14].

The first series of specimens was tested for fatigue until their complete fracture or until reaching the test base of $2\cdot10^6$ cycles of stress changes. Fatigue tests were performed in a test servohydraulic machine URS-20 at a three-point bending with a cycle asymmetry of $R_\sigma = 0$ and a frequency of 5 Hz under the

Table 1. Chemical composition of base and deposited metals [14]

Grade of material	Mass fraction of elements, %							
	C	Mn	Si	Cr	V	Mo	S	P
40Kh	0.36–0.40	0.5–0.8	0.17–0.37	0.8–1.1	–	–	≤0.035	≤0.035
Sv-08A*	0.05–0.12	0.2–0.4	≤0.03	≤0.10	–	–	≤0.04	≤0.04
PP-Np-25Kh5FMS*	0.20–0.32	0.5–1.0	0.80–1.30	4.6–5.8	0.2–0.6	0.9–1.5	≤0.04	≤0.04
4Kh5MFS**	0.32–0.40	0.2–0.5	0.90–1.20	4.5–5.5	0.3–0.5	1.2–1.5	≤0.04	≤0.04

*Mass fraction of elements in the deposited metal is given.

**Data on mechanical properties of the metal deposited with the wires Sv-08A and PP-Np-25Kh5FMS are absent in the literature. Therefore, data for their analogues are given (the closest as to the chemical composition and mechanical properties), respectively to steels 08kp and 4Kh5MFS.

Table 2. Mechanical properties of base and deposited metals [14]

Grade of material	Mechanical properties (after normalization)					
	Conditional yield strength $\sigma_{0.2}$, MPa	Ultimate tensile strength σ_t, MPa	Relative elongation δ, %	Relative reduction in area ψ, %	Impact toughness *KCU*, J/cm^2	Hardness *HV*
40Kh	345	590	12.5	52	7.5	174–217
08 kp**	196	320	33	60	–	≤131
Sv-08A*	1570	1710	12	54	51	444–478

*Data on mechanical properties of the metal deposited with the wires Sv-08A and PP-Np-25Kh5FMS are absent in the literature. Therefore, data for their analogues are given (the closest as to the chemical composition and mechanical properties), respectively to steels 08kp and 4Kh5MFS.

conditions of regular loading. The distance between the supports was 250 mm.

At the second series of specimens cyclic crack resistance was evaluated. To initiate the propagation of a fatigue crack in the deposited metal in the center of the specimen (in the area of maximum applied stresses), a V-shaped notch of 1.0–1.5 mm depth with 0.25 mm radius was made. After that, at a three-point cyclic bending with a maximum level of applied stresses in the cross-section of the specimen being 400 MPa, a fatigue crack was grown until reaching a length of 1 mm on a one of the side faces. The resulted notch with a crack was taken as an initial fatigue crack in the test specimen, which was then used to study the kinetics of fatigue fracture. While performing the fatigue tests on cyclic crack resistance, the length of the propagated fatigue crack was measured using an optical microscope with a division value of 0.01 mm on the two side faces of the specimen and then averaged. The tests were performed until a complete fracture of the specimens.

On the specimens of the third series, the efficiency of applying repair surfacing to increase the residual cyclic life of the specimens, having fatigue cracks in the deposited wear-resistant layer was investigated. The specimens were tested for fatigue at a three-point bending with a cycle asymmetry $R_\sigma = 0$ to the formation of a fatigue crack with a depth of 10–12 mm (when a crack passed through the deposited layers and deepened into the base metal). After that, repairs were carried out applying the method of arc surfacing, which consists of a complete mechanical removal of a fatigue crack and the metal around it and a subsequent remelting of the formed groove. The technology of repair surfacing is described in more detail in [7].

To study the nature of fatigue crack propagation in the deposited specimens after their repair, a metallographic microscope MIM-7 was used, equipped with a video eyepiece SIGETA MCMOS 3100. This video eyepiece is supplied with the software Toupview, used to perform digital processing of the obtained photographs and calculation of crack sizes at magnifications of ×0–×320. Before the measurements, the microscope was calibrated using a micrometer object.

Table 3. Results of fatigue tests of specimens of the first series

Number of specimen	Maximum cycle stresses, MPa	Cyclic life before fracture, cycles
1	500	>2000000
2	500	>2000000
3	600	>2000000
4	600	775100*
5	600	>2000000
*Defect in the fusion zone between the sublayer and wear-resistant layer.		

In addition, before the fatigue test in the specimens after repair surfacing, residual stresses were measured applying a non-destructive acoustic method using a portable ultrasonic stress control device [15].

Results of experiments and their discussion. Initially, two specimens of the first series of carbon steel 40Kh, deposited using flux-cored wire PP-Np-25Kh5FMS with a sublayer of low-carbon steel 08kp, were tested at maximum stress levels of 500 MPa, typical for the specimens made without a sublayer [11]. After operation of specimens during $2 \cdot 10^6$ cycles, no changes in fatigue crack stresses were detected. It should be noted that fracture of the specimens without a sublayer at maximum stress levels of 500 MPa occurred in the range from 560800 to 1420100 cycles of stress changes [11]. The other three specimens, deposited with a sublayer, were tested at the levels of maximum stresses increased to 600 MPa. The results of fatigue tests of the first series of specimens are given in Table 3.

An early fracture of the specimen No.4 of the first series after 775100 cycles was predetermined by the presence of a surfacing defect in the transition zone of a sublayer metal to the metal of a wear-resistant layer. Thus, the defect-free specimens with a sublayer of low-carbon steel withstood more than $2 \cdot 10^6$ cycles of stress changes at maximum stresses of 500–600 MPa. Therefore, the use of a sublayer of low-carbon steel in surfacing of a wear-resistant layer allowed increasing the life of the specimens after manufacturing surfacing by almost 2 times as compared to surfacing of the specimens without a ductile sublayer.

On three specimens of the second series from the sharp notch in a wear-resistant layer of metal, an initial crack with a depth of 1 mm was grown at maximum stress levels of 400 MPa. In the subsequent tests of the specimen also at the levels of maximum stresses of 400 MPa, the length of a fatigue crack and the corresponding number of cycles of a variable load N were recorded.

It was established that the main crack mainly propagates predominantly along the fusion boundary of individual beads. In the process of fatigue fracture, as a result of variable loads of a one metal layer to another in the transition zones, slight side branching from the main crack were observed, which propagated along the fusion line of a wear-resistant metal layer with a sublayer metal (Figure 1) and along the fusion line of a sublayer metal with the base metal (Figure 2). After the crack passed through a wear-resistant layer of metal and a sublayer of a low-carbon steel, the fracture of the specimens occurred on the base metal.

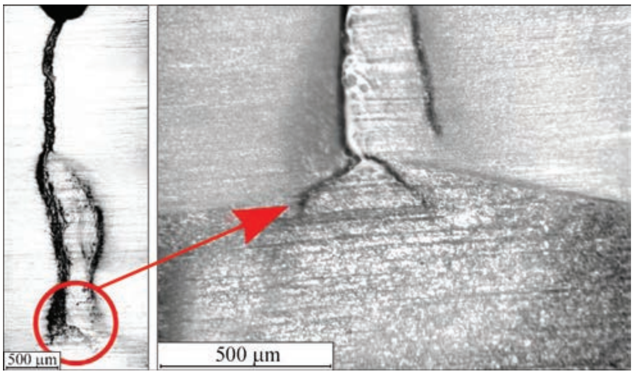

Figure 1. Branching of fatigue crack in the fusion zone of wear-resistant layer and ductile sublayer

This can be explained by several factors. First, in the area of overlapping adjacent deposited beads, the zone of chemical and structural heterogeneity is located, which negatively affects the properties of the material [1]. Secondly, during multibead multilayer surfacing, at the fusion boundary of adjacent beads and layers sharp angles may occur, which will be stress concentrators and, accordingly, initiate the formation of side cracks along the fusion line [16, 17]. After the crack passes through the wear-resistant layer of metal and the sublayer of low-carbon steel, the fracture of the specimens occurred on the base metal. Thus, the same as for the specimens deposited without a sublayer, it was found that the fusion lines of individual beads and layers play an important role in the process of fatigue fracture of deposited parts, as cracks mainly propagate either along the fusion of individual beads, or directly near this boundary (Figure 2). The only difference between these two surfacing technologies in relation to fatigue crack propagation is the formation of small side branching from the main crack (Figures 1, 2).

To construct kinetic diagrams of fatigue fracture (KDFF), the values of the stress intensity factor (SIF) were calculated from the expressions for a three-point load of a prismatic specimen with a cross edge crack [18]. The experimental dependence of fatigue crack growth rate on the SIF range in different layers of

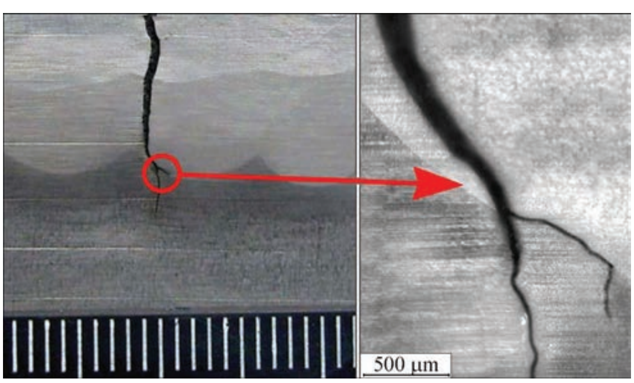

Figure 2. Branching of fatigue crack in the fusion zone of sublayer with base metal

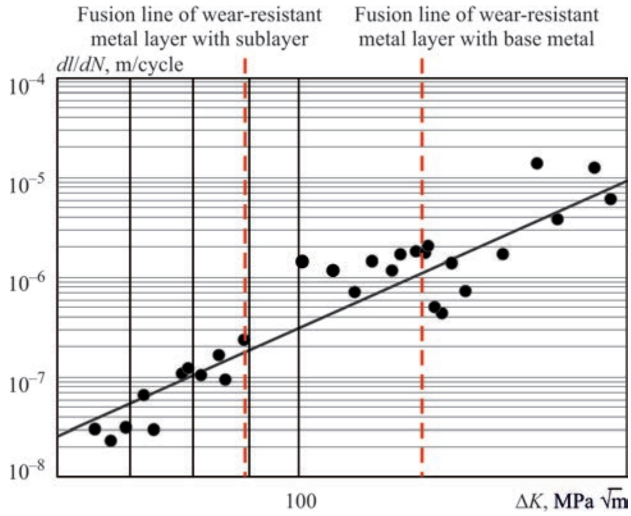

Figure 3. Kinetic diagram of fatigue fracture of multilayer material, formed by wear-resistant surfacing with the use of sublayer of low-carbon steel

metal in a multilayer specimen is given in the form of KDFF (Figure 3). The obtained data show that at the set levels of maximum stresses of 400 MPa, the range of changes in the growth rate of fatigue cracks in the multilayer material corresponds to the linear area of KDFF, and, accordingly, it can be described by the degree dependence of Paris $dl/dN = C(\Delta K)^m$ with the parameters $C = 5.75\cdot10^{-17}$ and $m = 4.87$. The maximum SIF values (140–180 MPa$\sqrt{\text{m}}$) on the specimens with a multilayer surfacing with a sublayer, 2–3 times exceed the maximum SIF values obtained on the specimens without a sublayer [7], which indicates the rationality of using a low-carbon sublayer to increase the crack resistance of a multilayer material with a wear-resistant surfacing.

On the specimens of the third series, at first initiation and propagation of fatigue cracks from probable defects in the deposited wear-resistant metal layer were modeled. Therefore, the specimens were tested under a cyclic loading until the formation of fatigue cracks with a depth of 10–12 mm, which were subsequently removed by repair surfacing. After repair surfacing, residual stresses were measured applying a non-destructive ultrasonic method. Schematic representation of places of residual stress measurement is

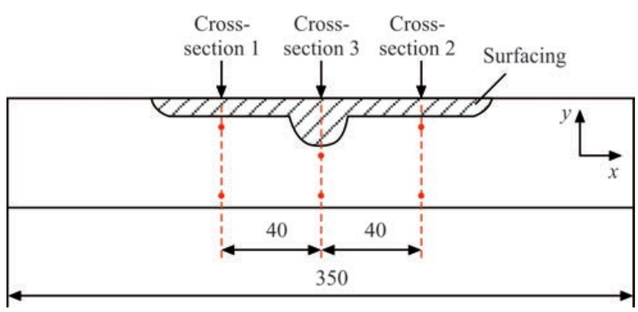

Figure 4. Schematic image of places of measuring residual stresses in the specimen after repair surfacing

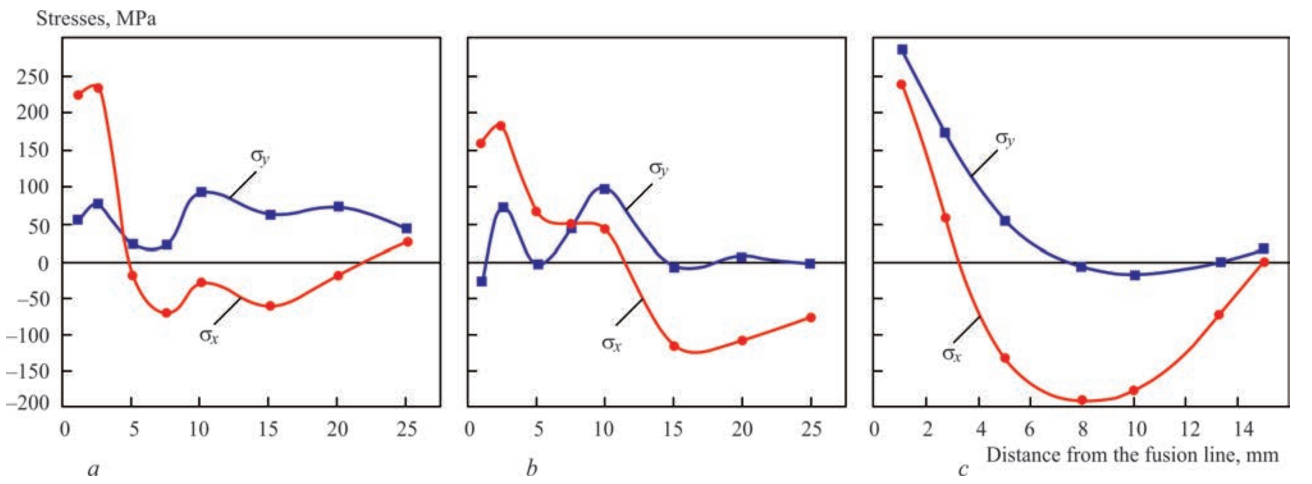

Figure 5. Distribution of residual stresses oriented along σ_x and across σ_y of the specimen after repair surfacing in the cross-section 1 (*a*), 2 (*b*) and 3 (*c*)

shown in Figure 4, and plots of distribution of residual stresses in the initial state and after repair surfacing are given in Figure 5. The measurements of residual stresses, oriented along and across the specimen, were performed from the fusion line of a low-carbon sublayer with the base metal (determined by the macrostructure) deep into the metal. The values of residual stresses given on the plots are averaged over the thickness of the specimen.

The use of ultrasonic quartz sensors of longitudinal and shear waves with a base of measuring 7×7 mm did not allow making measurement of stresses closer than 1 mm to the fusion line of a low-carbon sublayer with the base metal. The maximum longitudinal residual tensile stresses σ_x are located directly in the area of repair surfacing and amount to about 240 MPa at a distance of 1 mm from the fusion line (Figure 5, *b*). At a distance of 40 mm from the place of repair surfacing, the residual longitudinal tensile stresses σ_x at a distance of 1 mm from the fusion line are in the range of 160–220 MPa (Figure 5, *a*, *c*). At a further distance from the fusion line deep into the metal, a zone of residual compressive stresses is formed, which reach the values of up to –70– –120 MPa in the cross-sections 1, 2 and up to –200 MPa in the cross-section 3 (in the area of repair surfacing). A significant volume of deposited metal during repair surfacing leads to the formation of higher transverse residual tensile stresses at 280 MPa in this area as compared to manufacturing surfacing (Figure 5).

After measurements of residual stresses, the specimens of the third series were tested for fatigue at a three-point zero-cycle bending. The cyclic life of the specimens before and after repair surfacing is given in Table 4.

After repair surfacing, initiation and propagation of fatigue cracks in all the specimens of the third series took place at a distance from the repair place. As in the case of manufacturing surfacing, the process of fatigue fracture of the parts restored by surfacing occurred either at the fusion boundary of individual beads, or directly near this boundary, apparently as a result of chemical and structural heterogeneity in this area (Figure 6, *a*).

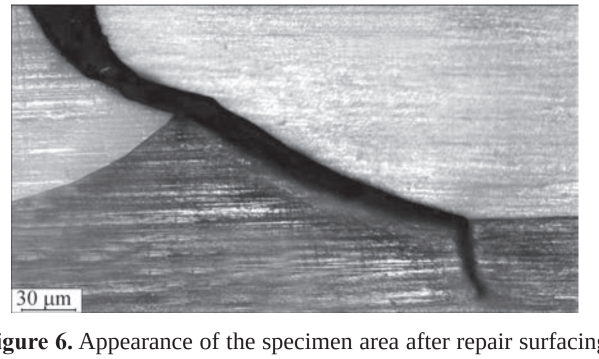

Figure 6. Appearance of the specimen area after repair surfacing with the formed fatigue crack, passing along the boundary between adjacent welded beads

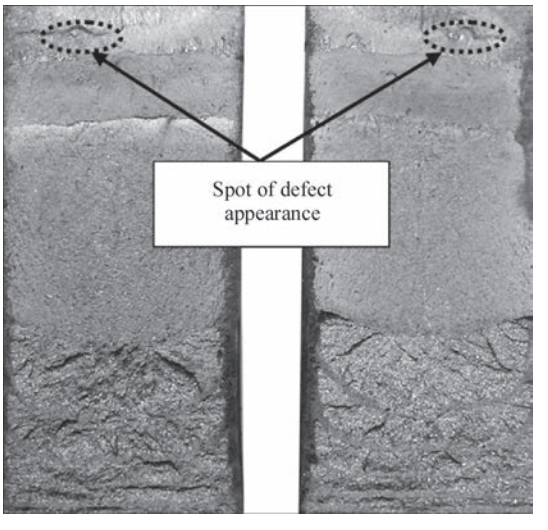

Figure 7. Appearance of fracture surface of the specimen No.10 with a defect along the fusion boundary between the individual layers of the deposited metal, from which fatigue crack was formed

Table 4. Results of fatigue tests of specimens of the third series

Number of specimen	Maximum cycle stresses, MPa	Cyclic life before formation of a crack of 10–12 mm, cycles	Cyclic life after repair surfacing, cycles	Total cyclic life, cycles
9	500	2127600	616300	2743900
10	600	461600	86900	1331100
11	600	2024700	109600	2134300

A low cyclic life of the specimen No.10 before the formation of a through crack with a length of 10–12 mm (Table 4) is predetermined by a technological defect of surfacing, which contributed to the early appearance of a crack inside the specimen (at a distance of 5 mm from the surface) in the fusion zone between individual layers of metal (Figure 7). Subsequently, at first the crack propagated in the wear-resistant metal before reaching the surface, and then in a low-carbon sublayer. After repair surfacing of the specimen No.10, initiation and propagation of a new fatigue crack occurred at 10–20 mm from the place of repair.

In general, it was confirmed that on the specimens No.9 and No.11 (Table 4), the application of repair surfacing to the products with fatigue cracks after their long-term operation does not lead to a significant increase in cyclic life after repair. This is associated with the fact that after long-term operation, the defect-free layer of deposited metal has a significant level of accumulated fatigue damages. Therefore, the repair of only a part of a product damaged by a fatigue crack without a complete removal of the deposited metal layer is inefficient.

However, considering the full cycle of a deposited part existence (manufacturing surfacing, operation, repair surfacing, operation), the proposed technology of repair surfacing using a ductile sublayer allowed increasing the total life of a deposited specimen by approximately 1.4 times as compared to the specimens deposited without a sublayer [7].

Nevertheless, based on the abovementioned data, in order to improve the efficiency of repair surfacing during repair of long-term operated products and to significantly increase the total life, it is recommended to remove not only the metal around the detected fatigue cracks, but the entire deposited layer to a depth of detected fatigue cracks with a subsequent restoration surfacing.

Conclusions

1. The technology of manufacturing and repair surfacing of specimens of carbon steel 40Kh, deposited using flux-cored wire PP-Np-25Kh5FMS with a sublayer of a low-carbon steel 08kp was developed. The non-destructive ultrasonic method for measuring stresses showed that the maximum longitudinal residual tensile stresses are located directly in the area of repair surfacing and amount to about 240 MPa at a distance of 1 mm from the fusion line of a low-carbon sublayer with the base metal. At a distance of 40 mm from the place of repair surfacing, the longitudinal residual tensile stresses at a distance of 1 mm from the fusion line are in the range of 160–220 MPa. A significant volume of deposited metal during repair surfacing leads to the formation of higher transverse residual tensile stresses at a level of 280 MPa in this area as compared to the manufacturing surfacing.

2. It was established that the main crack predominantly propagates along the fusion boundary of individual beads. In the process of fatigue fracture in the transition zones of a one metal layer to another, slight side branching from the main crack were observed, which propagated along the fusion line of the wear-resistant metal layer with the sublayer metal and along the fusion metal layer of the sublayer with the base metal. We suggest that such behavior is caused by the presence of a zone of chemical and structural heterogeneity in the areas of overlap of adjacent welded beads, which negatively affects the properties of materials and stress raisers predetermined by the geometry of adjacent deposited beads, which should be taken into account during development of technique and technology of repair surfacing.

3. The growth rate of fatigue cracks in different layers of metal of a multilayer material was experimentally investigated and the KDFF was constructed. It was established that the range of changes in the growth rate of fatigue cracks in the multilayer material corresponds to the linear area of KDFF, and accordingly can be described by the degree dependence of Paris $dl/dN = C(\Delta K)^m$ with the parameters $C = 5.75\cdot10^{-17}$ and $m = 4.87$. The maximum SIF values (140–180 MPa$\sqrt{\text{m}}$) obtained on the specimens with multilayer surfacing with a sublayer, is 2–3 times higher than the maximum SIF values obtained on the specimens without a sublayer, which indicates the rationality of a low-carbon sublayer to improve the crack resistance of multilayer material with a wear-resistant surfacing.

4. It was established that the cyclic life of the specimens of carbon steel 40Kh, deposited with the use of flux-cored wire PP-Np-25Kh5FMS with a sublayer of a low-carbon steel 08kp exceeds the cyclic life of the specimens deposited without a sublayer approximately by 2 times. Thus, the cyclic life of the specimens without a sublayer at maximum stress levels of 500 MPa is in the range of 561–1420 thou cycles of stress changes, and the cyclic life of the defect-free specimens with a sublayer at maximum stress levels of 500–600 MPa exceeds 2000 thou of cycles.

1. Du Toit, M., Van Niekerk, J. (2010) Improving the life of continuous casting rolls through submerged arc cladding with nitrogen-alloyed martensitic stainless steel. *Welding in the World*, 54(**11–12**), 342–349. DOI: https://doi.org/10.1007/bf03266748
2. Vundru, C., Paul, S., Singh ,R., Yan, W. (2018) Numerical analysis of multi-layered laser cladding for die repair applications to determine residual stresses and hardness. *Procedia Manufacturing*, 26, 952–961. DOI: https://doi.org/10.1016/j.promfg.2018.07.122
3. Gao, F., Zhou, J., Zhou, J. et al. (2017) Microstructure and properties of surfacing layers of dies manufactured by bimetal-gradient-layer surfacing technology before and after service. *The Int. J. Adv. Manuf. Technol.*, **88**, 1289–1297. DOI: https://doi.org/10.1007/s00170-016-8679-0
4. Zhang, J., Zhou, J., Tao, Y. et al. (2015) The microstructure and properties change of dies manufactured by bimetal-gradient-layer surfacing technology. *Ibid*, 80, 1807–1814 (2015). DOI: https://doi.org/10.1007/s00170-015-7170-7
5. Ahn, D.-G. (2013) Hardfacing technologies for improvement of wear characteristics of hot working tools: A Review. *Int. J. of Precision Engineering and Manufacturing*, 14 (**7**), 1271–1283. DOI: https://doi.org/10.1007/s12541-013-0174-z
6. Jhavar, S., Paul, C.P., Jain, N.K. (2013) Causes of failure and repairing options for dies and molds: A review. *Engineering Failure Analysis*, 34, 519–535. DOI: https://doi.org/10.1016/j.engfailanal.2013.09.006
7. Ryabtsev, I.O., Knysh, V.V., Babinets, A.A. et al. (2020) Fatigue life of specimens after wear-resistant, manufacturing and repair surfacing. *The Paton Welding J.*, **9**, 19–25. DOI: https://doi.org/10.37434/tpwj2020.09.03
8. Rjabcev, I.A., Senchenkov, I.K., Turyk, Je.V. (2015) *Surfacing. Materials, technologies, mathematical modeling*. Gliwice, Wydawnictwo politechniki slaskiej.
9. Korotkov V.A. (2017) More efficient surfacing. *Russian Engineering Research*, 37, 701–703. DOI: https://doi.org/10.3103/S1068798X17080093
10. Shao, C., Cui, H., Lu, F., Li, Z. (2019) Quantitative relationship between weld defect characteristic and fatigue crack initiation life for high-cycle fatigue property. *Int. J. of Fatigue*, 123, 238–247. DOI: https://doi.org/10.1016/j.ijfatigue.2019.02.028
11. Liu, H., Yang, S., Xie, C. et al. (2018) Mechanisms of fatigue crack initiation and propagation in 6005A CMT welded joint. *J. of Alloys and Compounds*, **741**, 188–196. DOI: https://doi.org/10.1016/j.jallcom.2017.12.374
12. Zerbst, U., Madia, M., Beier, H.T. (2017) Fatigue strength and life determination of weldments based on fracture mechanics. *Procedia Structural Integrity*, **7**, 407–414. DOI: https://doi.org/10.1016/j.prostr.2017.11.106
13. Ryabtsev, I.A., Knysh, V.V., Babinets, A.A. et al. (2019) Methods and specimens for comparative investigations of fatigue resistance of parts with multilayer surfacing. *The Paton Welding J.*, **2**, 29–34. DOI: https://doi.org/10.15407/tpwj2019.02.05
14. Oberg, E. et al. (1996) *Machinery's Handbook.* 25th Ed. Industrial Press Inc.
15. (2004) *Device for control of mechanical stresses and strains in solid media.* Pat. UA 71637 C2 [in Ukrainian].
16. Kaierle, S., Overmeyer, L., Alfred, I. et al. (2017) Single-crystal turbine blade tip repair by laser cladding and remelting. *CIRP J. of Manufacturing Sci. and Technology*, **19**, 196–199. DOI: https://doi.org/10.1016/j.cirpj.2017.04.001
17. Caccese, V., Blomquist, P. A., Berube et al. (2006) Effect of weld geometric profile on fatigue life of cruciform welds made by laser/GMAW processes. *Marine Structures*, 19(**1**), 1–22. DOI: https://doi.org/10.1016/j.marstruc.2006.07.002
18. Murakami, Yu. (1990) *Reference book on stress intensity coefficients.* In: 2 Vol. Moscow, Mir [in Russian].

Received 05.02.2021

https://doi.org/10.37434/tpwj2021.03.02

MATHEMATICAL MODELING OF RESIDUAL STRESSES IN WWER-1000 ELEMENTS AFTER HEAT TREATMENT

O.V. Makhnenko[1], S.M. Kandala[1], N.R. Basystyuk[1] and M.V. Cherkashin[2]
[1]E.O. Paton Electric Welding Institute of the NAS of Ukraine
11 Kazymyr Malevych Str., 03150, Kyiv, Ukraine. E-mail: office@paton.kiev.ua
[2]«UKRTsNIITMASh» Company
7a Vasylenka Str., 03124, Kyiv, Ukraine. E-mail: ukrcniitmash@ukr.net

Determination of residual life and extension of safe operating life of WWER-1000 internals for a term of up to 60 years beyond the design period is an important scientific and engineering objective for nuclear power industry of Ukraine. During long-term operation the reactor internal elements: reflection shield and cavity are exposed to intensive impact of damaging radiation dose that causes the processes of radiation embrittlement, swelling and creep in the material (08Kh18N10T austenitic steel). Technological residual stresses after welding and subsequent heat treatment should be taken into account at calculation-based substantiation of the safe operating life of reactor internal elements. In the work, mathematical modeling was used to derive residual stress distributions in the volume of the reflection shield and internal cavity after electroslag welding and their redistribution fields after the technological process of postweld heat treatment by the austenitizing mode. It is determined that the residual welding stresses are largely relaxed during austenitizing. In the reflection shield, however, which is of complex geometry with variable wall thickness and cooling channels, high residual stresses develop, due to occurrence of a significant temperature gradient at cooling during austenitizing. These stresses should be taken into account at determination of the residual life of WWER-1000 reactor internals. 8 Ref., 8 Figures.

K e y w o r d s : WWER-1000, reactor internals, reflection shield, internal cavity, electroslag welding, heat treatment, austenitizing, residual stresses

In keeping with design documentation, the elements of reactor internals (RI) of WWER-1000 power unit, namely reflection shield (RS) and internal cavity (IC) are welded structures from 08Kh18N10T austenitic steel. It is known that these structural elements are the most prone to neutron irradiation during long-term operation of the power unit. All the longitudinal welded joints of the above-mentioned RI elements were produced by the technology of electroslag welding (ESW), and IC circumferential welded joints were made by automatic submerged-arc welding.

In keeping with the requirements of normative documentation [1] all the made ESW joints of parts from steels of austenitic class should be subjected to postweld heat treatment by austenitizing mode specified for base metal. At overall heat treatment the welded items are completely placed into the furnace. In keeping with [2], the austenitizing process is steel heat treatment, similar to hardening of carbon steels, which consists of its heating up to the temperature of 1050–1100 °C, short-time soaking at this temperature and further rapid cooling. During heating, chromium and carbon carbides completely dissolve in austenite, while rapid cooling prevents repeated precipitation of carbides. However, in structures with complex geometry, such as RS (variable thickness, cooling channels, etc.), it may lead to appearance of a rather high temperature gradient in the cross-section due to non-uniform cooling and to formation of high residual stresses, accordingly.

At calculated substantiation of extension of WWER-1000 RI life beyond the design period (up to 60 years of operation and longer) it is necessary to take into account the technological residual stresses at structure fabrication. At present the questions of technological residual stresses are not sufficiently well-studied as regards RI elements [3].

Mathematical modeling of thermal processes and viscoelastoplastic deformation of material was used to perform numerical study of formation, relaxation and redistribution of residual stresses during welding and further heat treatment (austenitizing) of RS and IC of WWER-1000 power unit.

ESW technological parameters. Schemes of layout of RS and IC longitudinal welded joints, made by electroslag technology, are shown in Figure 1. Welded joint width is approximately 30 mm, ESW technological parameters, assumed in calculation, are given be-

O.V. Makhnenko — https://orcid.org/0000-0002-8583-0163, S.M. Kandala — https://orcid.org/0000-0002-2036-0498, M.V. Cherkashin — https://orcid.org/0000-0003-0672-5443

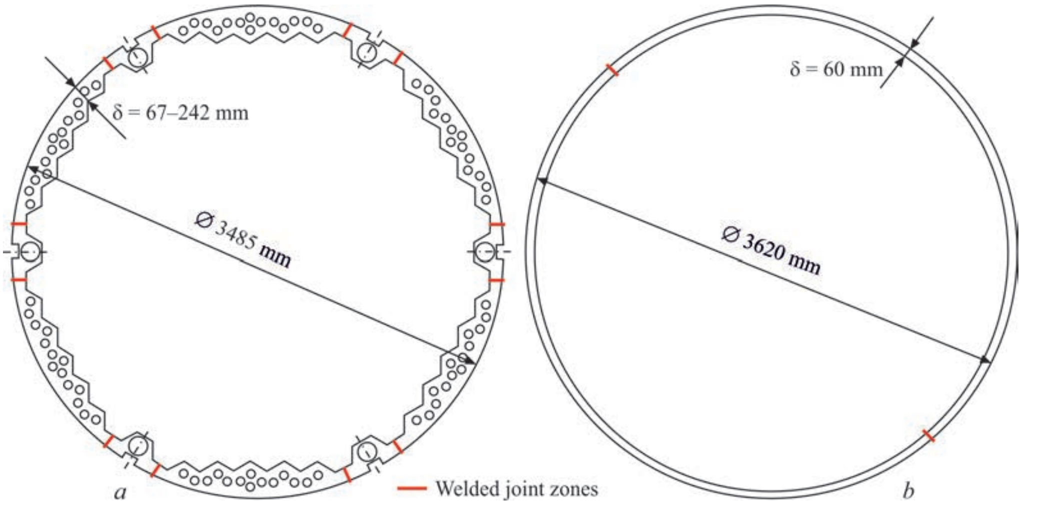

Figure 1. Layout of longitudinal welded joints in the RS (*a*) and IC (*b*) cross-section

low [3]. The power consumed in welding, is equal to approximately 9 kW, while ESW parameters provide sufficient power for heating (~60 %) and melting of weld metal (~40 %).

ESW technological parameters

Welding current, A	600
Voltage, V	46
Electrode feed rate, m/h	230
Welding speed, mm/s	0.42
Depth of liquid metal pool, mm	40
Temperature of liquid metal pool, °C	2000
Nozzle thickness, mm	10
Wire diameter, mm	3
Number of working electrode wires (which are duplicated), pcs	2/2
Flux	48-OF-6
Electrode wire grade	Sv-04Kh19NN11M3
Thermal efficiency of the process, %	85

Description of mathematical model for determination of SSS in welding. The problem of determination of SSS of RI elements was solved using finite element modeling. In view of large dimensions of RS and IC structural elements, as well as presence of cyclic symmetry in their structures, the developed finite-element models are 30 deg sectors, consisting of flat rectangular elements with face size not greater than 5 mm (Figure 2).

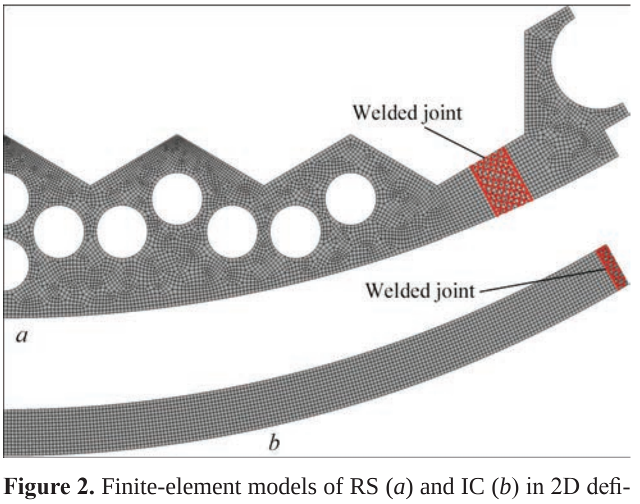

Figure 2. Finite-element models of RS (*a*) and IC (*b*) in 2D definition

The temperature fields at ESW were modeled using the equation of nonstationary heat conductivity, which includes calculation of bulk welding heat source $W(x, y, z, t)$:

$$\frac{\partial}{\partial x}\left(\lambda\frac{\partial T}{\partial x}\right)+\frac{\partial}{\partial y}\left(\lambda\frac{\partial T}{\partial y}\right)+\frac{\partial}{\partial z}\left(\lambda\frac{\partial T}{\partial z}\right)+ +W(x, y, z, t)=c\rho\frac{\partial}{\partial}, \quad (1)$$

where ρ is the material density; c is the specific heat capacity; λ is the coefficient of heat conductivity; T is the material temperature.

The temperature problem was solved with the assumption of quickly-moving heat source that allowed using the two-dimensional finite element model in the RS and IC cross-section.

Boundary conditions on the surfaces of RI elements, allowing for the convective heat exchange with the environment, were assigned in the following form:

$$q=-h(T_{\text{out}}-T), \quad (2)$$

where T_{out} is the ambient temperature; q is the heat flow; h is the coefficient of heat transfer from the surface at convective heat exchange with the environment.

Initial conditions at $t = 0$:

$$W(x, y, z, 0)=, \quad T=20\ ^{\circ}\text{C}, \quad T_{\text{out}}=20\ ^{\circ}\text{C}. \quad (3)$$

Taking into account the «plane strain» hypothesis, solution of the problem for determination of the distributions of spatial components of stresses and strains was obtained using two-dimensional models of RS and inner cavity cross-section in the elastoplastic definition, i.e. the strain tensor can be presented as a sum of tensors [4]:

$$\varepsilon_{ij} = \varepsilon_{ij}^{e} + \varepsilon_{ij}^{p} (i,\ j) = x,\ y,\ z, \quad (4)$$

where ε_{ij}^{e} is the elastic strain tensor; ε_{ij}^{p} is the plastic strain tensor.

Components of tensors of stresses σ_{ij} and elastic deformations ε_{ij}^{e} are related to each other by Hooke's law:

$$\varepsilon_{ij}^{e} = \frac{\sigma_{ij} - \sigma_{ij}\sigma}{2G} + \delta_{ij}(K\sigma + \varphi), \quad (5)$$

where δ_{ij} is the unit tensor ($\delta_{ij} = 0$, if $i \neq j$, $\delta_{ij} = 1$, if $i = j$), $\sigma = \frac{1}{3}(\sigma_{xx} + \sigma_{yy} + \sigma_{zz})$, $G = \frac{E}{2(1+\nu)}$ is the shear modulus; $K = \frac{1-2\nu}{E}$ is the bulk compression module; E is the Young's modulus; v is the Poisson's ratio; φ is the function of free relative elongations caused by temperature change:

$$\varphi = \alpha(T - T_0), \quad (6)$$

where α is the coefficient of relative temperature elongation of material.

Plastic strains are related to the stressed state by an equation of the theory of plastic nonisothermal flow, associated with Mises flow condition:

$$d\varepsilon_{ij}^{p} = d\lambda(\sigma_{ij} - \delta_{ij}\sigma) \quad (i,\ j = x,\ y,\ z), \quad (7)$$

where $d\varepsilon_{ij}^{p}$ is the increment of ε_{ij}^{p} tensor at the given moment of time t, due to the deformation history, stresses σ_{ij} and temperature T; $d\lambda$ is the scalar function which is determined by the flow conditions in the following form:

$$\begin{gathered} d\lambda = 0, \text{ if } f = \sigma_i^2(T) < 0 \text{ or } f = 0, \text{ at } df , 0; \\ d\lambda > 0, \text{ if } f = 0 \text{ and } df > 0; \\ \text{state } f = 0 \text{ is inadmissible,} \end{gathered} \quad (8)$$

where σ_i is the stress intensity

$$\sigma_i = \frac{1}{\sqrt{2}}\Big[(\sigma_{xx} - \sigma_{yy})^2 + (\sigma_{xx} - \sigma_{zz})^2 + \\ +(\sigma_{yy} - \sigma_{zz})^2 + 6(\sigma_{xy}^2 + \sigma_{xz}^2 + \sigma_{xz}^2)\Big]^{\frac{1}{2}},$$

$\sigma_y(T)$ is the yield limit of the material at temperature T.

Equation (7) shows that in order to obtain the results on the components of residual stresses σ_{ij} and strains ε_{ij}, it is necessary to consider the process of development of elastoplastic strains with time, starting from a certain initial state. The method of sequential tracking is traditionally used for this purpose, when for moment t the solution is sought, if complete solution for $(t - \Delta t)$ moment is known, where Δt is the step of tracking the development of elastoplastic strains, within which it can be approximately assumed that this development occurs by a rather simple loading trajectory. In this case, the connection between end increments of the strain tensor $\Delta\varepsilon_{ij}$ and stress tensor σ_{ij}, in keeping with [4] can be written as:

$$\Delta\varepsilon_{ij} = \psi(\sigma_{ij} - \delta_{ij}\sigma) + \delta_{ij}(K\sigma) - b_{ij}, \quad (9)$$

where ψ is the function of the state of material in point (x, y, z) at moment t.

$$\begin{gathered} \psi = \frac{1}{2G}, \text{if } f < 0, \quad \psi = \frac{1}{2G}, \text{if } f = 0, \\ \text{state } f = 0 \text{ is inadmissible,} \end{gathered} \quad (10)$$

b_{ij} is the tensor function of additional strains, which is determined by increase of $\Delta\varphi$ and known results of the previous tracking step:

$$\begin{gathered} b_{ij} = \left[\frac{\sigma_{ij} - \delta_{ij}\sigma}{2G} + \delta_{ij}(K\sigma)\right]_{t-\Delta t} + \\ +\delta_{ij}\Delta\varphi(i,\ j = x,\ y,\ z). \end{gathered} \quad (11)$$

Flow conditions in the form of (7) include significant nonlinearity of the function of material state ψ. The iteration processes are usually used for realization of this type of physical nonlinearity. As a result, at each iteration, the physically nonlinear problem becomes a linear problem of the type of the problem of the theory of elasticity with a variable shear modulus, which is equal to $\frac{1}{2\psi}$, and additional strains b_{ij}. Such a linearized problem is solved using the numerical methods.

Results of modeling the residual stresses at ESW. The developed finite-element mathematical models, taking into account the given technological parameters of ESW and geometrical characteristics of RI elements, were the base for deriving the calculated distributions of temperatures and stresses at different moments of time from the beginning of welding and up to the residual state. Figure 3 shows the distributions of maximum temperatures, when making the longitudinal welded joints of the RS and IC during welding. Even taking into account the features characteristic for single-pass ESW of thick elements, heating is of a local nature with a high temperature gradient in the circumferential direction.

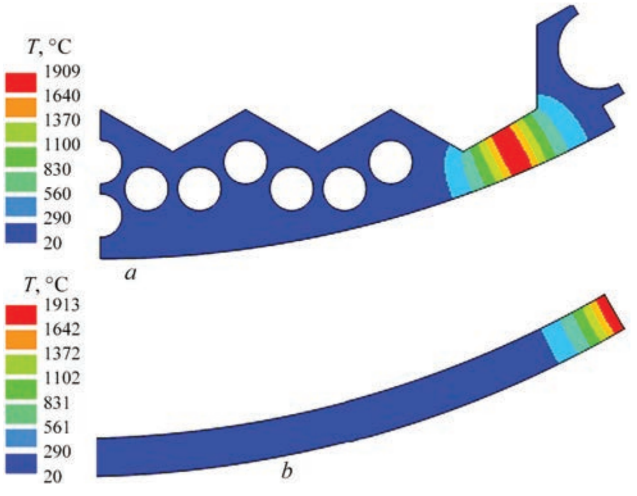

Figure 3. Calculated distributions of maximum temperatures when making longitudinal welded joints of RS (*a*) and IC (*b*)

Obtained results of mathematical modeling of the stressed state showed that the local high-temperature heating at ESW and further cooling leads to formation in the considered RI elements of high residual stresses of up to 230 MPa in the axial direction in the weld zone (Figure 4, *e*, *f*), i.e. up to material yield limit, and to a lower level of residual stresses of up to 50 MPa in the radial (Figure 4, *a*, *b*) and circumferential (Figure 4, *c*, *d*) directions, owing to uniformity of welding heating across the thickness at ESW. Considering the rather large zone of high tensile residual stresses after welding both in the RS and in the IC, it is rational to conduct postweld heat treatment by the austenitizing mode, in order to lower the level of residual welding stresses and to ensure dissolution of chromium and carbon carbides, which form in the HAZ in welding.

Heat treatment modeling. Welded joints of critical structures are subjected to postweld heat treatment. In keeping with the requirements of normative documentation [1], the welded joints of structural elements of NPP equipment from austenitic steel are subjected to heat treatment by the mode of austenitizing (hardening).

In keeping with [5], austenitizing (hardening) of the items should be conducted by the following mode: heating to 1050–1100 °C, parts with up to 10 mm material thickness should be cooled in air, those of more than 10 mm thickness — in water. Complex-shaped welded items should be cooled in air to avoid deformations. Soaking time at heating during hardening is 30 min for items with wall thickness of up to 10 mm, for those of more than 10 mm it is 20 min, +1 min per 1 mm of maximum thickness. The thickness of RS and IC in the welded joint zone is 67 and 60 mm, respectively. Thus, cooling of RI elements during austenitizing was to take place in air and soaking time should be approximately 87 min for the RS and 80 min for the IC.

When conducting mathematical modeling of the process of postweld heat treatment of RI elements, a feature of the developed model for determination of the nonstationary temperature field was convective

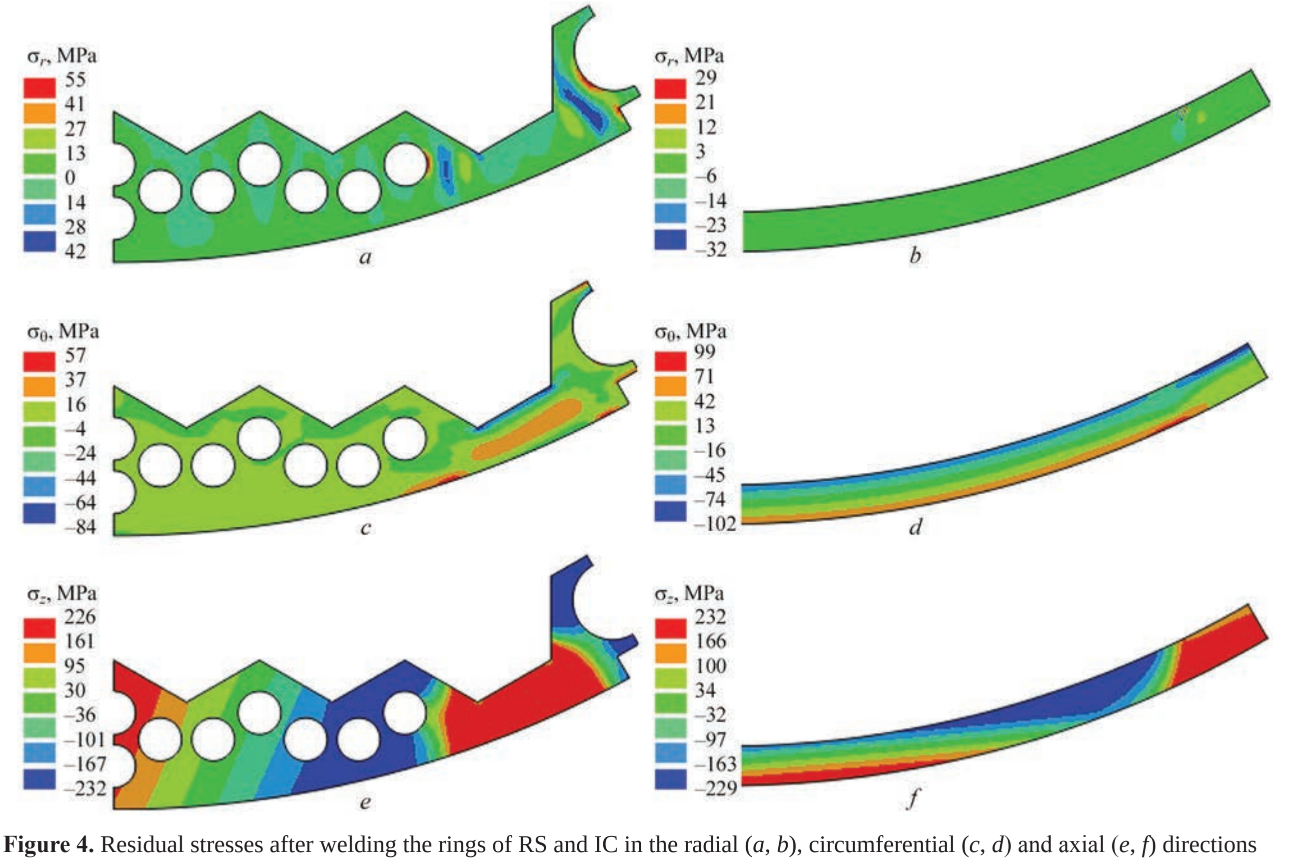

Figure 4. Residual stresses after welding the rings of RS and IC in the radial (*a*, *b*), circumferential (*c*, *d*) and axial (*e*, *f*) directions

heat exchange on the surfaces due to gradual heating of the environment (air) in the furnace, and further rather fast cooling in air. The nonstationary boundary conditions corresponded to uniform increase of the ambient temperature during heating and rapid temperature lowering to 20 °C at cooling.

The heat treatment schedule, namely, changes of ambient temperature during austenitizing of RI elements in the furnace at heating at the rate of 30 °C/h, soaking for 87 min and cooling at a higher rate in air is shown in Figure 5.

Initial and boundary conditions of the boundary value problem of determination of temperature distributions in the RS and IC at heat treatment:

$$\text{at } t = 0\ T_{out}(0) = 20\ °\text{C},\ T(0) = 20\ °\text{C}$$
$$q = -h(T_{out}(t) - T),\ T_{out}(t) = 30\ °\text{C/h}\cdot t,$$
$$T_{out}^{max} = 1100\ °\text{C}.$$

The coefficient of heat transfer from the surfaces of RI elements at convective heat exchange with the environment in the furnace or in air was taken equal to the value of $h = 30$ W/(m^2·°C) under the conditions of natural convection and constant in the entire range of heating and cooling temperature. Radiant heat exchange in the developed model was not modeled separately, and its contribution was taken into account in a certain increase of the heat transfer coefficient.

The long process of heating of welded structural elements to austenitizing temperature causes the processes of high-temperature creep in the material, leading to relaxation of residual stresses in the welded joint zone.

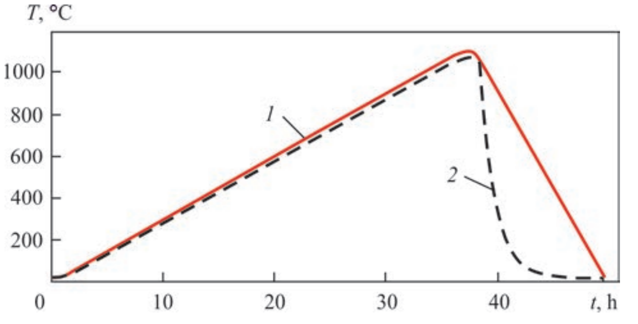

Figure 5. Plot of the change of temperature of RI element material during heat treatment by austenitizing mode: *1* — austenitizing mode; *2* — calculated temperature

In the developed model the problem of determination of SSS at heat treatment was solved in the visco-elastoplastic formulation [4]:

$$\varepsilon_{ij} = \varepsilon_{ij}^{e} + \varepsilon_{ij}^{p} + \varepsilon_{ij}^{cr}\ (i,\ j = x,\ y,\ z),$$

where the creep strain rate was determined using Bailey–Norton law [6]

$$\dot{\varepsilon}_{ij}^{cr} = A\sigma_{eq}^{n}. \tag{12}$$

For 08Kh18N10T austenitic steel at the temperature of 700 °C (973 K) the following coefficients can be taken: $A = 6.948\cdot10^{-14}$, $n = 6.22$ at determination of the rate of temperature creep strain [7]. In view of absence of data on creep of RI element material at higher temperatures in the developed model of determination of their SSS at heat treatment the abovementioned coefficients were taken for the entire high-temperature heating range above 700 °C temperature. This raises the conservatism of the calculation results, as at higher temperatures the creep processes proceed more intensively.

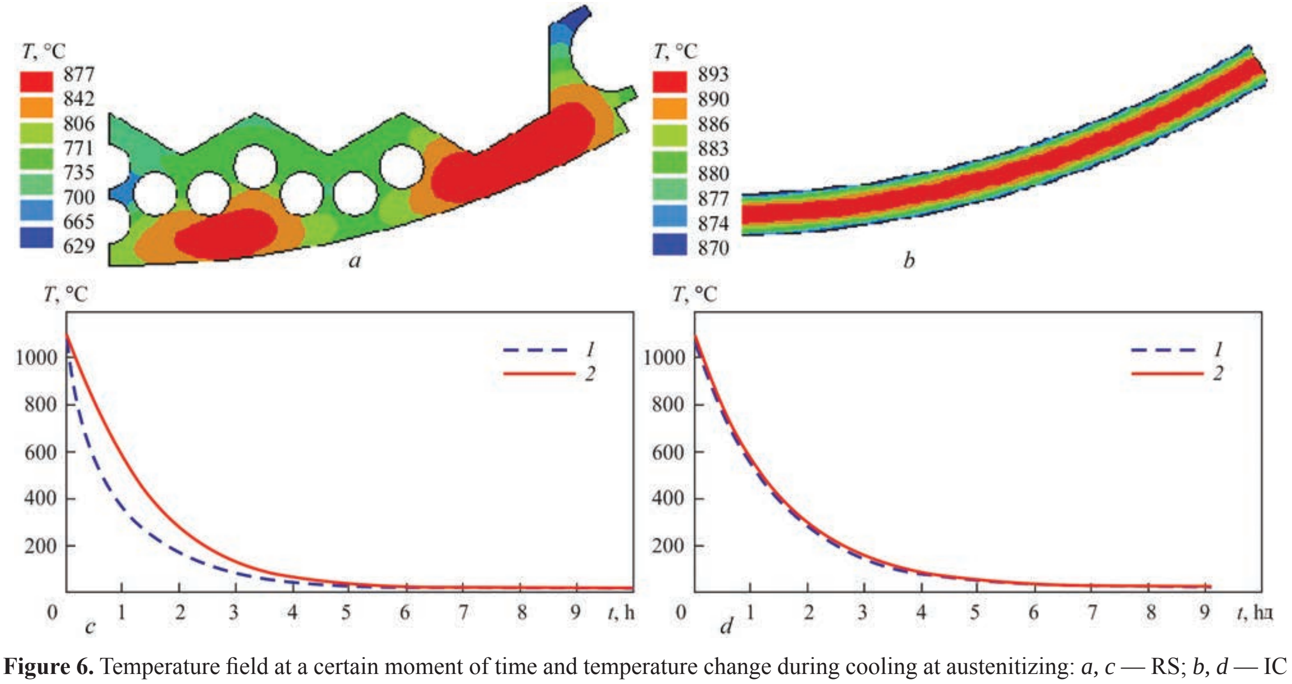

Figure 6. Temperature field at a certain moment of time and temperature change during cooling at austenitizing: *a*, *c* — RS; *b*, *d* — IC (*1* — on the surface; *2* — internal volume)

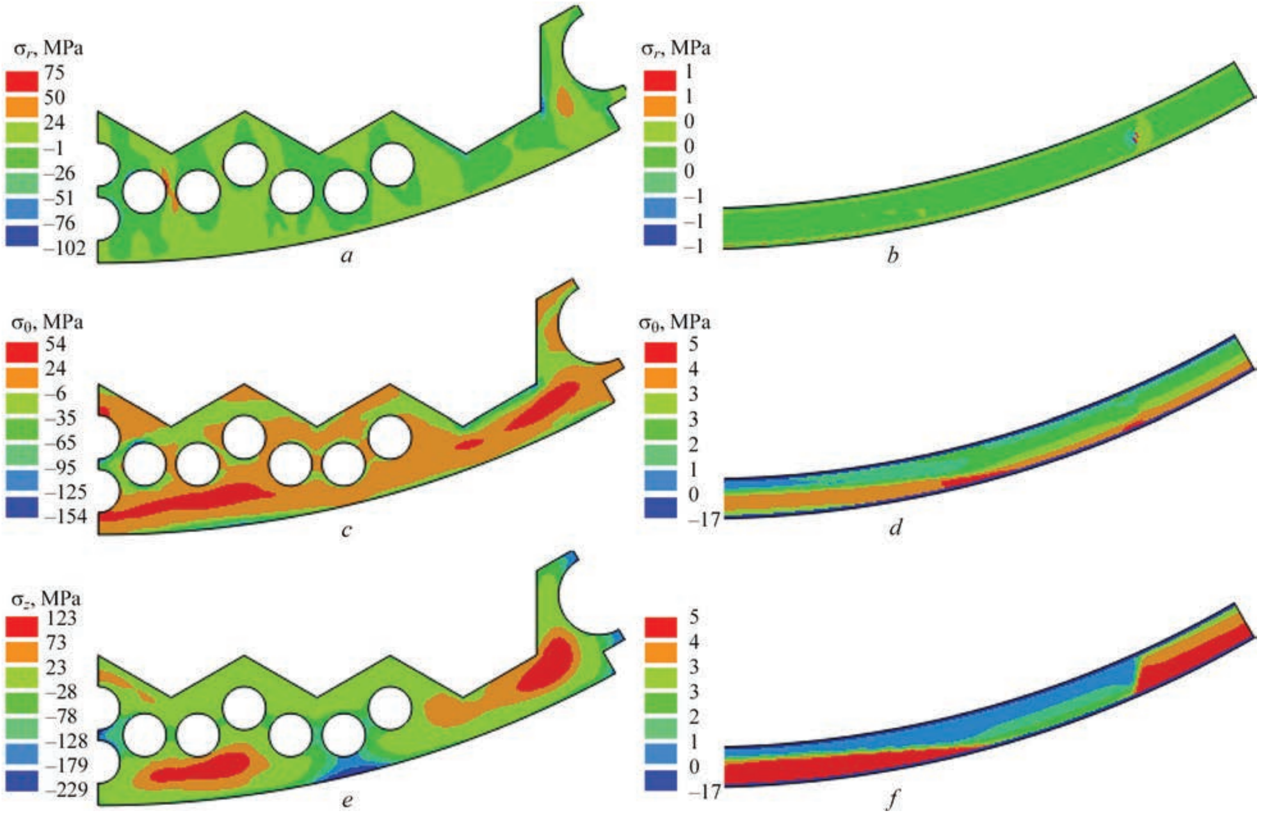

Figure 7. Residual stresses after welding and austenitizing of RS and IC in the radial (*a*, *b*), circumferential (*c*, *d*) and axial directions (*e*, *g*)

It should be noted that the RS cross-section differs from that of the IC by its nonuniform thickness, as the internal surface of the RS follows the reactor core boundary, while the presence of cooling channels promotes cooling of RS material in operation. Such geometrical irregularity influences the nonuniform cooling of the structure as a result of intensive heat exchange from the surfaces during cooling in air at heat treatment, that creates a temperature gradient of up to 250 °C (Figure 6, *a*, *c*) on the RS boundaries and in its internal volume, and, consequently, leads to formation of residual stresses after the austenitizing process (Figure 7, *a*, *c*, *e*). The inner cavity, owing to a uniform wall thickness, is characterized by a constant temperature gradient in the radial direction and absence of the gradient in the circumferential direction.

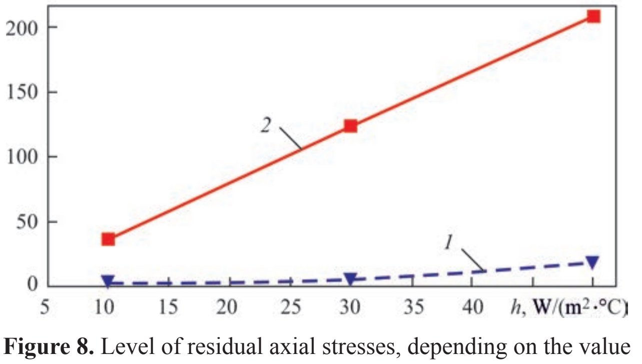

Figure 8. Level of residual axial stresses, depending on the value of heat transfer coefficient: *1* — IC; *2* — RS

Temperature difference on the surfaces and in the internal volume during cooling in air at heat treatment is not higher than 25 °C that does not lead to formation of high residual stresses (Figure 7, *b d*, *f*).

In the RS the highest residual stresses, both compressive (up to –230 MPa) and tensile (up to 120 MPa) are observed in the axial direction (Figure 7, *e*), and in the circumferential direction tensile residual stresses reach 55 MPa. Such a high level of residual stresses must be taken into account during determination of the residual life of RI elements when conducting the calculation-based substantiation of extension of the service life of WWER-1000 reactors.

As regards the IC, as a result of postweld heat treatment by austenitizing mode the residual welding stresses relax almost completely during long-term heating up to high temperatures, and rather low residual stresses in the range of (–17–5) MPa (Figure 7, *b*, *d*, *f*) form at the stage of rapid cooling, taking into account the low temperature gradient by thickness (Figure 6, *b*, *d*), due to IC regular cylindrical shape with a constant wall thickness. Such a low level of residual stresses cannot be ignored at calculation-based determination of the residual life of RI elements.

It should be noted that there is little published data, describing the temperature dependence of the coefficients of heat transfer from the surface of stainless steel parts at heating up to high temperatures. In keeping with [8], the coefficient of heat transfer at still air cooling can reach 150 W/(m^2·°C) for 1100 °C temperature. In such a case high residual plastic strains and stresses can form at cooling of RI elements during austenitizing.

Evaluation of the effect of average coefficient of heat transfer from the surface assumed in calculations, on the level of maximum residual stresses after RS and IC heat treatment by the austenitizing mode was performed. Modeling was conducted at the values of average coefficient of heat transfer of 10, 30 and 50 W/(m^2·°C). Figure 8 shows the dependence of the level of maximum residual stresses in the axial direction on the coefficient of heat transfer, which is characterized by a considerable rise at increase of the coefficient of heat transfer. For a more accurate assessment of the effect of austenitizing process on residual stresses in RI elements, it is necessary to have precised coefficients of heat transfer for stainless steel. Taking them into account can have a considerable effect on determination of the residual life of WWER-1000 RI.

Conclusions

1. At calculation-based substantiation of extension of the life of WWER-1000 RI beyond the design period (up to 60 years of operation and longer), it is necessary to take into account the technological residual stresses. Mathematical modeling of thermal processes and viscoelastoplastic deformation of the material was used to perform a numerical study of formation, relaxation and redistribution of residual stresses during welding and further heat treatment of structural elements of WWER-1000 RS and IC.

2. Results of mathematical modeling showed that postweld heat treatment of RI elements (RS and IC) by the austenitizing mode (T = 1100 °C) allows significantly relaxing the residual welding stresses. However, high geometrical irregularity of the RS affects the nonuniformity of cooling in the structure volume at intensive heat exchange in air that leads to appearance of a temperature gradient and, consequently, formation of high residual stresses that should be taken into account at determination of the life of WWER-1000 RI.

1. (1989) PNAE G-7-009–89: *Equipment and pipelines of nuclear power installations. Welding and overlaying, general provisions.* Moscow, ENERGOATOMIZDAT [in Russian].
2. Rakhmilevich, Z.Z., Radzin, I.M., Faramazov, S.A. (1985) *Reference book of mechanics of chemical and petrochemical production.* Moscow [in Russian].
3. Makhnenko, O.V., Mirzov, I.V., Porokhonko, V.B. (2016) Modeling of residual stresses, radiation swelling and stressed state of in-service WWER-1000 reactor baffle. *The Paton Welding J.*, **4**, 32–38. DOI: https://doi.org/10.15407/tpwj2016.04.03
4. Makhnenko, V.I. (1976) *Computational methods of investigation of welded stress and strain kinetics.* Kiev, Naukova Dumka [in Russian].
5. (2004) STP 26.260.484–2004: *Heat treatment of corrosion-resistant steels and iron-nickel-based alloys in chemical engineering.* OJSC «NIIKHIMMASH» [in Russian].
6. Rabotnov, Yu.N. (1966) *Creep of structural elements.* Moscow, GIFML [in Russian].
7. Margolin, B.Z., Gulenko, A.G., Kursevich, I.P., Buchatskii, A.A. (2006) Modeling for fracture in materials under long-term static creep loading and neutron irradiation. Pt 2: Prediction of creep rupture strength for austenitic materials. *Strength of Materials*, 38(**5**), 449–457.
8. Nemchinskiy, A.L. (1953) *Thermal calculations of heat treatment*. Leningrad, Sudpromgiz [in Russian].

Received 01.03.2021

https://doi.org/10.37434/tpwj2021.03.03

ELECTRIC ARC SPRAYING OF INTERMETALIC Fe–Al COATINGS USING DIFFERENT SOLID AND POWDER WIRES

Yu.S. Borisov, A.L. Borisova, N.V. Vihilyanska, I.A. Demyanov and **O.M. Burlachenko**
E.O. Paton Electric Welding Institute of the NAS of Ukraine
11 Kazymyr Malevych Str., 03150, Kyiv, Ukraine. E-mail: office@paton.kiev.ua

The mechanism of formation and structure of coatings based on the system iron-aluminium, sprayed by electric arc method using wires of solid cross-section and a flux-cored wire were investigated. The grain-size composition, structure and microhardness of particles (spraying products of electrode wires of iron and aluminium) captured from the spraying jet, as well as structure, phase composition and microhardness of electric arc coatings of the system iron-aluminium were studied. It was found that during spraying of Fe + Al and Fe + AlMg wires, the interaction of particles in the jet does not occur and the products of spraying represent particles of iron and aluminium with the appropriate hardness. In this case, the formation of intermetallics in the coatings also does not occur and they have a heterogeneous structure consisting of the components based on iron and aluminium. It was found that intermetallic FeAl structure is formed only after heat treatment of sprayed coatings at 650 °C. During spraying of flux-cored wire FCW(Fe–Al) in the process of melting the sheath and the filler, the interphase interaction occurs, which results in the formation of coatings with a microhardness of 2460 ± 290 MPa, the main phase of which is intermetallic Fe_3Al. 21 Ref., 1 Table, 6 Figures.

Keywords: electric arc spraying, intermetallic, iron-aluminium, coating, solid cross-section wire, flux-cored wire, microstructure

Alloys based on iron aluminides belong to the promising structural materials designed to operate at temperatures of 600–1000 °C. They are characterized by a low cost, high resistance to wear, corrosion and oxidation also in aggressive sulfur-containing environments [1, 2].

The use of alloys based on iron aluminide as protective coatings is largely predetermined by the possibility of increasing the service life of different elements of mechanisms operating under the conditions of increased wear and corrosion, reducing the cost of coated products as compared to high-alloy steels, as well as the possibility of using simple and inexpensive technology of their spraying [3, 4]. These materials own their properties to an ordered crystalline structure with strong chemical bonds in combination with a close package of atoms, which leads to an increased resistance to creep, recrystallization and high-temperature corrosion as compared to traditional metal alloys [5].

Coatings based on Fe-Al intermetallics are produced by thermal spraying methods: plasma [6], high-velocity oxygen fuel [7] and detonation [8]. In these methods, as spraying materials intermetallic powders produced by spraying [9], mechanical alloying and mechanochemical synthesis are used [10, 11].

An alternative method of producing iron-aluminium coatings is electric arc spraying (EAS), in which coatings are formed as a result of combined spraying of Fe- and Al-containing wires. In the case when as spraying materials composite wires FeAl [12] or flux-cored wires (FCW) [4] are used, consisting of an iron sheath with an aluminium powder filler, as a result of spraying, in the coatings interaction of melts of iron and aluminium with the formation of intermetallic phases Fe_3Al and FeAl occurs. In spraying using combined spraying wires of a solid cross-section, coatings with a pseudo-alloy structure are formed [13]. In particular, in spraying using wires of iron and aluminium, coatings consist of initial components of iron and aluminium, their oxides and solid solutions based on Fe and Al [14]. In this case, the synthesis of intermetallic phases Fe_xAl_y does not occur or their presence does not exceed 5 wt.% [15], and the formation of intermetallics Fe_2Al_5, Fe_3Al and FeAl occurs in the case of further heat treatment of coatings at 650 °C [14].

At the PWI, the studies of peculiarities of forming electric arc coatings based on the Fe–Al system have been carried out since the 1990s. The electric arc coatings of the steel-aluminium system containing 10 % of aluminium, which were developed by the authors [16], were used by the Lviv branch of the Central De-

Yu.S. Borisov — https://orcid.org/0000-0002-6019-8464, A.L. Borisova — https://orcid.org/0000-0002-7376-3370,
N.V. Vihilyanska — https://orcid.org/0000-0001-8576-2095, I.A. Demyanov — https://orcid.org/0000-0003-4536-9971,
O.M. Burlachenko — https://orcid.org/0000-0003-2277-4202,

sign Bureau «Soyuzenergoremont» to protect screen pipes of boilers from a high-temperature ($T \leq 550$ °C) sulfur corrosion at a weak gas abrazive wear and were successfully operated at Burshtyn, Transnistria and Kryvyi Rih GRES-2 power plants during the period of 1–4 years.

The use of ferrochromaluminium-based flux-cored wires in EAS method allows producing coatings with a high level of physical and mechanical properties (σ_{adh} = 20.4 MPa, Young's modulus (E) is $7.83 \cdot 10^{-4}$ MPa, porosity is 4 ± 0.7 %, fatigue limit of steel 45 with coating (σ_{-1}) is 220 MPa) [17]. The developed coatings were successfully applied for restoration of parts of agricultural machinery of a number of enterprises in Moldova [18].

In [19] it is noted that the comparison of coatings deposited by thermal spraying methods from compact wires with the same ones from flux-cored wires or flexible rods shows that the latter provide a set of higher service properties. At the same time, until nowadays detailed studies and comparison of features of formation of intermetallic coatings from compact and powder materials were not carried out.

The aim of the work is to study the peculiarities of intermetallic Fe–Al coatings formation in the conditions of electric arc spraying with the use of dissimilar and flux-cored wires.

Materials and methods of investigations. Spraying of coatings of the Fe–Al system was performed applying electric arc method using EM-14M metallizer. The coating was produced by a combined spraying of solid cross-section wires (steel wire Sv08A and aluminium wire A99; steel wire Sv08A and aluminium AMg6 alloy wire). To spray coatings based on Fe–Al intermetallics, a flux-cored wire was manufactured, consisting of a sheath of steel St08kp (rimmed) and a filler — Al powder of grade PA-4.

The calculation to form the flux-cored wire with the composition 86 Fe + 14 Al (wt.%), consisting of a tubular metal sheath St08kp and Al powder, consists in calculation of the required bulk density of Al powder, in which the powder uniformly fills the entire cavity of the metal pipe with a diameter of 303 cm. The bulk density of Al powder, which provides a uniform filling of the volume of the inner cavity of the pipe, is calculated by the formula

$$\gamma_{\mathrm{b.d.Al}} = \frac{P}{V_{\mathrm{t}}},$$

where P is the mass of Al powder (14 g); V_{p} is the volume of the cavity of the metal pipe formed from the strip St08kp, which is calculated by the formula

$$V_{\mathrm{t}} = S_{\mathrm{t}} L_{\mathrm{t}},$$

where S_{p} is the cross-sectional area of the metal pipe, which is calculated by the formula

$$S_{\mathrm{t}} = \frac{\pi D^2}{4} = 0.785 \cdot 0.303^2 = 0.072\ \mathrm{cm}^2,$$

and L_{p} is calculated by the formula

$$L_{\mathrm{t}} = \frac{P_{\mathrm{t}}}{B\delta\gamma_{\mathrm{st}}},$$

where P_{p} is the mass of the pipe (86 g); B is the width of the strip (1.2 cm); δ is the thickness of the strip (0.04 cm); γ_{st} is the density of St08kp (7.8 g/cm^3).

Hence:

$$L_{\mathrm{t}} = \frac{86}{1.2 \cdot 0.04 \cdot 7.8} = 229.7\ \mathrm{cm},$$

$$V_{\mathrm{t}} = 229.7 \cdot 0.072 = 16.54\ \mathrm{cm}^3,$$

$$\gamma_{\mathrm{b.d.Al}} = \frac{14}{16.54} = 0.85 \frac{\mathrm{g}}{\mathrm{cm}^3}.$$

As a result of the calculations, it was found that to form the flux-cored wire from a mixture of 86Fe + 14Al (wt.%), which corresponds to the formula of Fe_3Al intermetallic, it is necessary to use Al powder with a bulk density of 85 g/cm^3. To produce such a powder, the initial Al powder (bulk density is 1.3 g/cm^3) was treated in an attrition mill for 75 min at a speed of 400 rpm and the ratio of the mass of the balls to the mass of the charge 7:1 with addition of zinc stearate in the amount of 2 wt.% to achieve a bulk density of powder of 0.85 g/cm^3.

The filling factor of the manufactured flux-cored wire FCW(Fe–Al) amounts to 16 %. The structure of the wire is presented in Figure 1.

The diameter of the used wires of both solid cross-section and flux-cored wire was 2 mm.

Based on the studies of peculiarities of the formation of coatings from dissimilar wires [13] and considering the literature data [14], for electric arc spraying

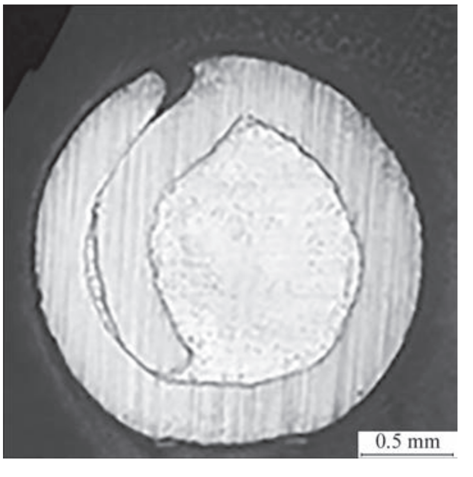

Figure 1. Structure of flux-cored wire FCW (Fe–Al)

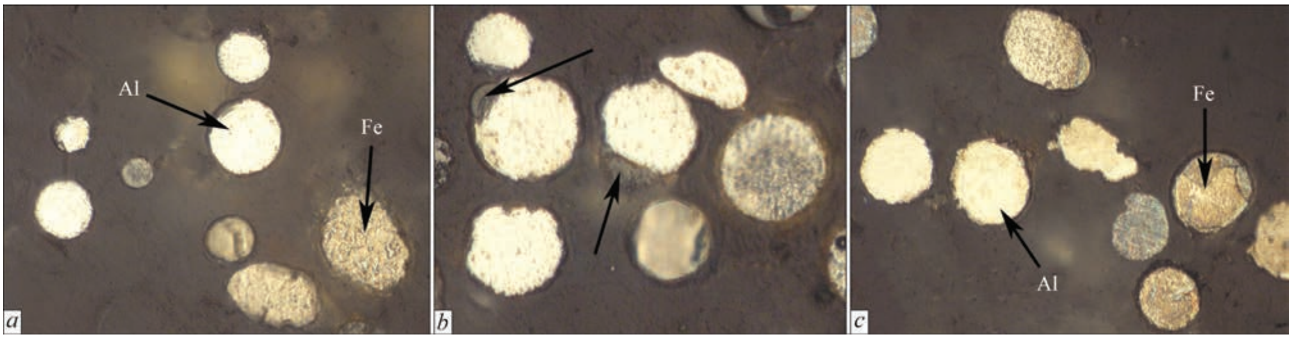

Figure 2. Microstructure of products of wires spraying: *a, b* — Fe + Al; *c* — Fe + AlMg; *a, c* — ×400; *b* — ×800

of coatings based on Fe-Al intermetallics, the following technological parameters of the process were selected: current is 200 A, voltage on the electrodes is 38 V, compressed air pressure is 0.65 MPa, spraying distance is 200 mm. This spraying mode provides a stable melting process of the used electrode wires.

In order to study the nature of the development of the processes of interaction of melt particles in the wires, formed by spraying dissimilar wires of a solid cross-section Fe + Al and Fe + AlMg, during movement at spraying distance between each other and with the environment, determination of their sizes and investigation of the structure of spraying products was collected in a water bath with the sizes of 500×500×200 mm. The bath is installed under a jet of a sprayed material at a distance of 200 mm. In the produced weldment, the structure and dispersion of particles were investigated applying the metallographic method by measuring their size on metallographic sections by means of an optical microscope. To detect the microstructure, etching of metallographic sections of powder particles was performed with 10 % alcohol solution of nitric acid for 4–5 min.

During metallographic examinations, the Neophot-32 optical microscope with a device for digital photography was used, and microhardness measurements were performed in the PMT-3 device. X-ray structure analysis (XSPA) of the coatings was performed by means of the DRON-3 diffractometer in CuK_α-radiation with a graphite monochromator at a step movement of 0.1° and an exposure time at each point of 4 s, with the following computer processing of the obtained digital data.

Characteristics of products of a combined spraying of Fe + Al and Fe + AlMg wires

Parameters of particles, μm	Sv08A + Al		Sv08A + AMg6	
	Fe	Al	Fe	AlMg
Grain-size composition of spraying products, %				
<40	18	35	23	30
40–50	19	25	22	28
50–60	18	18	18	20
60–70	12	8	12	12
70–80	12	8	9	8
80–90	8	1	6	1
90–100	7	2	5	1
>100	6	3	5	1
Average size of particles, μm				
d_{av}	63	52	59	51
Microhardness, MPa				
$HV_{0.05}$	2570±810	320±90	2790±590	470±110

Results of investigations. The study of the microstructure of particles of products of a combined spraying of Fe + Al and Fe + AlMg wires showed that they consist of iron and aluminium particles (Figure 2), i.e. interaction between iron and aluminium particles during spraying process was not detected. The particles are mostly spherical in shape, but particles of irregular elongated shape are also found. The microhardness of sprayed particles corresponds to either the microhardness of pure iron (2500–2700 MPa), or pure aluminium (300–500 MPa).

On some aluminium particles a presence of dome-shaped formations of solid and hollow structure is observed, which are located on their surface (indicated by arrows in Figure 2, *b*). Probably, these formations represent aluminium oxide, as far as when particles are passing through the spraying jet, on the surface of aluminium particles an oxidation process with the formation of an oxide film develops. A similar phenomenon is observed during plasma spraying of aluminium-containing materials [20].

The characteristics of the products of combined spraying of Fe + Al and Fe + AlMg wires are presented in Table.

The study of the size of the sprayed particles (Table) showed that the main fraction of aluminium particles (~ 60 %) has a size of <50 μm, iron (~ 50 %) is 40–70 μm, the average size of aluminium particles is 51–52 μm, iron is 59–63 μm. It is known that the size of particles of the products of spraying metal melts mainly depends on the value of their surface tension [21]. Therefore, this difference in the dispersion of the products of spraying dissimilar wires (Fe and Al) is associated with the fact that aluminium has a lower coefficient of surface tension (σ_{Al} = 914 MJ/m^2) than iron (σ_{Fe} = 1850 MJ/m^2), and in the process of a com-

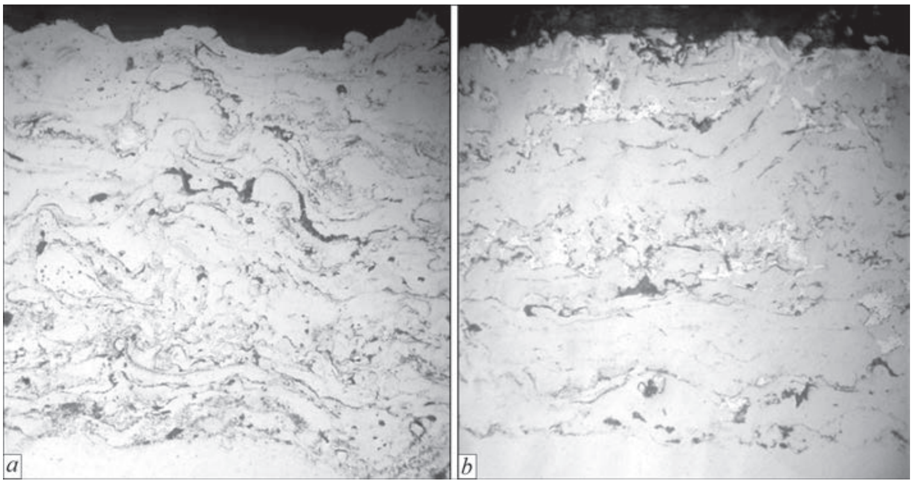

Figure 3. Microstructure of electric arc coatings (×200): *a* — Fe + Al; *b* — Fe + AlMg

bined spraying a more intensive spraying of the aluminium melt occurs. No significant difference in the dispersion of the products of spraying wires of pure aluminium and aluminium AMg6 alloy was detected because of a slight difference in their coefficients of surface tension.

As a result of metallographic (Figure 3) and XSPA (Figure 4) analyzes of sprayed coatings, it was found that the coatings, produced by combined spraying of Sv08A wires with aluminium (Fe + Al) and Sv08A with aluminium AMg6 alloy (Fe + Al) consist of a mixture of iron and aluminium. The microhardness of the areas of coatings Fe + Al and Fe + AlMg based on iron is 2400–2600 MPa and aluminium is 700–800 MPa.

It is known that the formation of Fe-Al intermetallics can be achieved by heat treatment of the coatings produced by combined spraying of iron and aluminium wires [14]. In this work, the heat treatment of the Fe + AlMg coating was carried out at a temperature of 650 °C for two hours with the following cooling in water. The time of treatment was chosen from the calculations of the diffusion coefficient of aluminium into iron in a solid phase. In this mode of heat treatment in the coating, the formation of intermetallic phases Fe_2Al_5, Fe_3Al and FeAl (Figure 4, *c*) occurs,

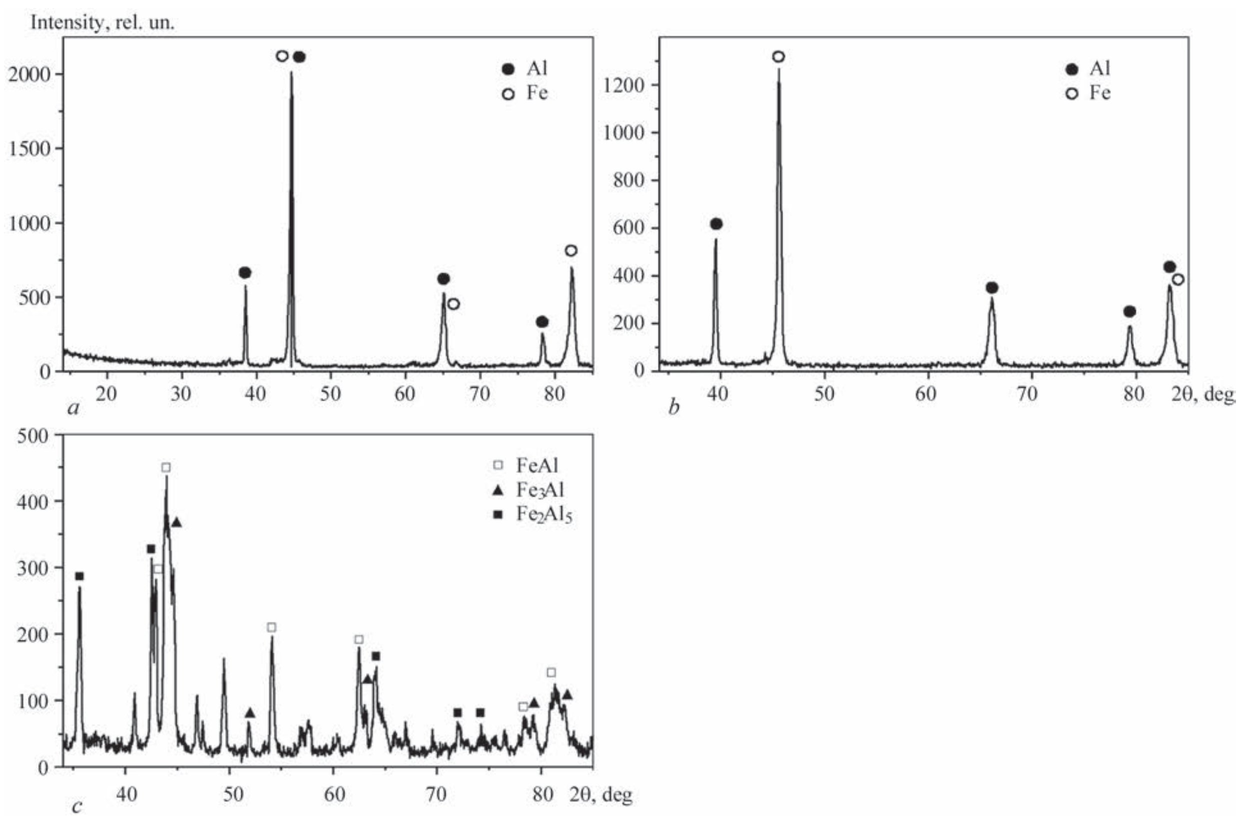

Figure 4. X-ray patterns of electric arc coatings: *a* — Fe + Al; *b* — Fe + AlMg; *c* — Fe + AlMg after treatment

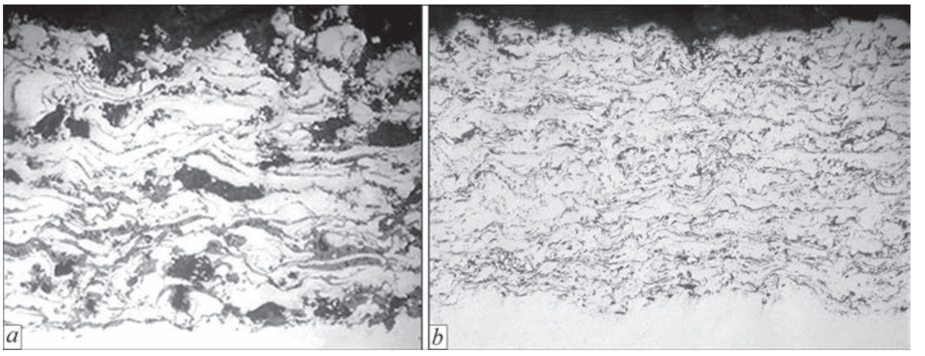

Figure 5. Microstructure (×400) of Fe + AlMg electric arc coating after heat treatment (*a*) and from flux-cored wire FCW (Fe–Al) (*b*), ×200

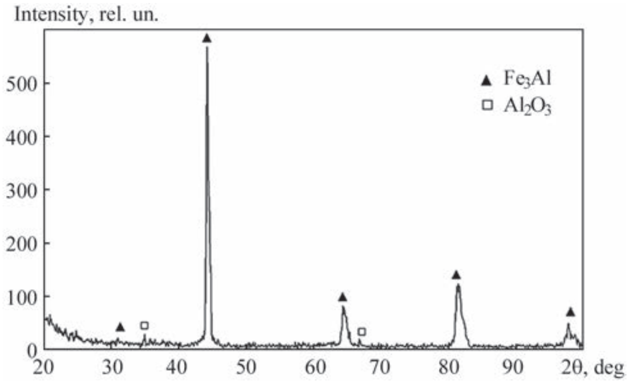

Figure 6. X-ray pattern of electric arc coating produced by spraying flux-cored wire FCW (Fe–Al)

whereas pure aluminium and iron were not detected applying the method of XSPA.

Comparing the microstructure of the coating after heat treatment (Figure 5, *a*) with the coating before heat treatment (Figure 3, *b*), an increase in strongly pronounced oxide interlayers with the presence of porosity along the boundaries of the lamellae is observed. At the same time pure aluminium and iron are not observed in the coating, and it consists of diffusion layers of lamellar structure. This indicates a complete proceeding of diffusion processes during heat treatment at the selected mode. The microhardness of the Fe + AlMg coating after heat treatment amounts to 2750 ± 760 MPa.

In the case of spraying flux-cored wire containing Al (FCW (Fe–Al)) powder as a filler, in the microstructure interlayers of pure aluminium of the coating are not observed (Figure 5, *b*). This suggests that all the aluminium powder in the spraying process reacted with the melt of steel sheath or oxidized. The microhardness of the coating amounts to 2460 ± 290 MPa.

XSPA of the FCW (Fe–Al) coating (Figure 6) showed that it consists of Fe_3Al phase, for which the flux-cored wire composition with the impurities of aluminium Al_2O_3 oxide was intended. This indicates that in the process of spraying FCW, a complete interaction of the steel sheath melts with the aluminium filler with the formation of intermetallic and a slight oxidation of aluminium particles occurs.

Conclusions

1. The study of the process of dispersion of melts of dissimilar Fe and Al wires in the conditions of electric arc spraying showed that as a result of combined spraying of wires, the interaction of particles during movement in the flow does not occur, and the spraying products consist of separate particles of iron and aluminium. The dispersion of the products of spraying wires of iron and aluminium is determined by the values of the surface tension of the melts of these materials and their average size is 59–63 μm during the use of Sv08A wire and 51–52 μm in the case of using A99 and AMg6 wires.

2. During deposition of coatings applying electric arc method in the case of combined spraying of iron and aluminium wires, the structure of the coating consists of Fe and Al lamellae. The intermetallic FeAl-structure of the coating in this case is formed by heat treatment of the coating at 650 °C for two hours.

3. When using a flux-cored wire consisting of a steel sheath and a filler (aluminium powder), intermetallic coatings are formed in the process of electric arc spraying, the main phase of which is Fe_3Al, which is a product of interfacial interaction between the sheath melts (Fe) and the powder filler (A1).

1. Deevi, S.C., Sikka, V.K. (1996) Nickel and iron aluminides: An overview on properties, processing, and applications. *Intermetallics*, 4(**5**), 357–375. DOI: https://doi.org/10.1016/0966-9795(95)00056-9
2. Stoloff, N.S. (1998). Iron aluminides: Present status and future prospects. *Mater. Sci. and Engin., A*, 258(**1–2**), 1–14. DOI: https://doi.org/10.1016/s0921-5093(98)00909-5
3. Yang, D.-M., Tian B.-H., Cao Y. (2011) Microstructures and properties of FeAl coatings prepared by LPPS, APS and HVOF. In: *Proc. of ITSC'2011*, 1229–1234.
4. Xu, B., Zhu, Z., Ma, S. et al. (2004) Sliding wear behavior of Fe–Al and Fe–Al/WC coatings prepared by high velocity arc spraying. Wear, 257(**11**), 1089–1095. DOI: https://doi.org/10.1016/j.wear.2004.05.012
5. Guilemany, J. M., Cinca, N., Casas, L., Molins, E. (2009) Ordering and disordering processes in MA and MM intermetallic

iron aluminide powders. *J. of Mater. Sci.*, 44(**8**), 2152–2161. DOI: https://doi.org/10.1007/s10853-009-3296-z

6. Borisov, Yu.S., Borisova, A.L., Vigilyanska, N.V. et al. (2020) Coatings based on Fe–Al intermetallics produced by the methods of plasma and supersonic plasma gas-air spraying. *The Paton Welding J.*, **7**, 29–37. DOI: https://doi.org/10.37434/as2020.07.04
7. Guilemany, J.M., Cinca, N., Fernández, J., Sampath, S. (2008) Erosion, abrasive, and friction wear behavior of iron aluminide coatings sprayed by HVOF. *J. of Thermal Spray Technol.*, 17(**5-6**), 762–773. DOI: https://doi.org/10.1007/s11666-008-9252-7
8. Borisov, Yu.S., Borisova, A.L., Astakhov, E.A. et al. (2017) Detonation coatings of intermetallic powders of Fe-Al system produced using mechanical alloying. *The Paton Welding J.*, **4**, 23–29.
9. Prasad, Y.V.R.K., Sastry, D., Sundar, R., Deevi, Seetharama (2001) Optimization of hot workability and hot deformation mechanisms in FeAl and Fe_3Al based alloys. In: *Proc. of the Int. Symp. on Structural Intermetallics*.
10. *Rajath* Hegde, M.M., Surendranathan, A.O. (2009) Synthesis, characterization and annealing of mechanically alloyed nanostructured FeAl powder. *Frontiers of Materials Sci. in China*, 3(**3**), 310–318. DOI: https://doi.org/10.1007/s11706-009-0021-4
11. Borisov, Yu.S., Borisova, A.L., Burlachenko A.N. et al. (2017) Structure and properties of alloyed powders based on Fe_3Al intermetallic for thermal spraying produced using mechanochemical synthesis method. *The Paton Welding J.*, **9**, 33–39.
12. Matvejshin, E.N. (2009) Strength and tribotechnical properties of iron-aluminium and copper-aluminium metalized coatings. *Problemy Tribologii*, **4**, 54–57 [in Russian].
13. Borisov, Yu.S., Vigilyanskaya, N.V., Demyanov, I.A. (2013) Study of effect of electric arc spraying modes on structure and properties of pseudoalloy coatings. *The Paton Welding J.*, **12**, 9–15.
14. Chen, Y., Liang, X., Wei, S. et al. (2009) Heat treatment induced intermetallic phase transition of arc-sprayed coating prepared by the wires combination of aluminium-cathode and steel-anode. *Applied Surface Science*, 255(**19**), 8299–8304. DOI: https://doi.org/10.1016/j.apsusc.2009.05.142
15. Chmielewski, T., Siwek, P., Chmielewski, M. et al. (2018) Structure and selected properties of arc sprayed coatings containing in-situ fabricated Fe–Al intermetallic phases. *Metals*, 8(**12**), 1059. DOI: https://doi.org/10.3390/met8121059
16. Borisova, A.L., Gubenko, B.G., Kostin, V.A. et al. (1990) Peculiarities of formation and structure of electrometallized coatings of steel-aluminium system. *Avtomatich. Svarka*, **8**, 41–44 [in Russian].
17. Borisova, A.L., Mitz, I.V., Kleyman, A. (2000) Arc sprayed coatings of ferroalloy-base flux-cored wires.: In: *Proc. of the 1st Int. Thermal Spray Conf. on* Thermal Spray Surface Engineering Via Applied Research (Montreal, Canada).
18. Borisova, A.L., Mitz, I.V., Kleyman, A.Sh. (1990) Influence of aluminium on structure and physicomechanical properties of coatings from flux-cored wires with ferrochromium filler. In: *Strength of parts of agricultural technique. Transact.*, Kishinev, 27–33 [in Russian].
19. Borisov, Yu.S., Korzhik, V.N. Kozyakov, I.A. (1995) Flame coatings of Fe–B system from flux-cored wires and flexible cords. *Avtomatich. Svarka*, **12**, 12–25 [in Russian].
20. Kulik, A.Ya., Borisov, Yu.S. et al. (1985) *Thermal spraying of composite powders*. Leningrad, Mashinostroenie [in Russian].
21. Ageev, V.A., Belashchenko, V.E., Feldman, I.E., Chernoivanov, A.V. (1989) Analysis of methods for control of parameters of sprayed particles in electric arc metallization. *Svarochn. Proizvodstvo*, **12**, 30–32.

Received 09.02.2021

https://doi.org/10.37434/tpwj2021.03.04

PECULIARITIES OF EMERGENCY FAILURE OF A PROCESS PIPELINE

M.D. Rabkina, V.A. Kostin and **T.G. Solomiichuk**
E.O. Paton Electric Welding Institute of the NAS of Ukraine
11 Kazymyr Malevych Str., 03150, Kyiv, Ukraine. E-mail: office@paton.kiev.ua

Analysis of failure of process pipeline, including a study of the properties, chemical composition and structure of the metal of welded joints, as well as the center of fracture and nature of crack propagation, made it possible to establish the most probable causes that led to its premature failure. It is assumed that such reasons are: a defect in a longitudinal weld; residual stresses in the pipe resulting from local heat treatment of the assembly circular weld; and probable longitudinal stresses arising from pipeline sagging between the supports. Ref. 9, 4 Tables, 7 Figures.

Keywords: technological pipeline; longitudinal and circumferential welded joints; defects in welded joints; lacks-of-fusion; structural heterogeneity; lamellar tearing; destruction

Pipeline failure, shutdown and accidents, as well as the extent and consequences of emergencies in gas and oil pipelines, both main and in-plant ones, largely depend on the quality and properties of pipe metal [1, 2]. During performance of complex pressure test of a technological pipeline (after operation for about 2.5 years on the whole) by technical nitrogen under pressure $P = 10^2$ MPa [3], its emergency depressurization took place. Data analysis suggested that the main factors, which could lead to pipeline destruction, alongside the possible nonconformity of the metal proper to the specified requirements, probably are: heat treatment of site circumferential welded joints (high-temperature tempering — heating up to the temperature of 760 ± 20 °C at three-hour soaking) that is conducted at welding of pipe sections; temperature mode of the process line, at which the pipe temperature in the destruction zone periodically varied from ambient temperature to 500 °C; and presence of bending stresses in the support zone.

Figure 1. Fragment of the dismantled pipe with fracture region and marks for cutting out templates for investigations and mechanical testing

Previous visual analysis of the destruction mode showed that fracture propagated both in base metal and in the HAZ, as well as in the circumferential site weld (Figure 1). Here, the failure center was not determined. Pipes were supplied for mounting in the form of sections from several shells after welding in the manufacturing plant. Then these sections were welded by site circumferential welds.

The objective of the studies was establishing the conformity of the initial material parameters to the specified (standard) values, detection of failure center, nature of crack propagation, as well as clarifying the possible causes for depressurizing of the process pipeline.

Investigation methods. Samples for investigations were prepared from templates cut out of a defective section of the pipe of process pipeline of 1020 mm diameter with 10 mm wall thickness.

Determination of chemical composition of metal of the fragments was conducted in X-ray fluorescent

Table 1. Chemical composition of X12CrMo5 steel, wt.%

Sample	C	Si	Mn	S	P	Cr	Ni	Cu	Mo	Ti
Outer side	0.13	0.27	0.48	0.008	0.020	4.6	0.30	0.13	0.55	<0.01
Inner side	0.13	0.27	0.48	0.008	0.022	4.6	0.30	0.13	0.56	<0.01
EU Certificate data	0.117	0.27	0.46	0.001	0.008	4.76	0.27	0.20	0.59	0.0061N
15KhM GOST 200072–74	0.15	<0.5	<0.5	<0.025	<0.03	4.5–6.0	<0.6	<0.2	0.45–0.60	<0.03

M.D. Rabkina — https://orcid.org/0000-0003-3498-0716, V.A. Kostin — https://orcid.org/0000-0002-2677-4667,
T.G. Solomiichuk — https://orcid.org/0000-0002-3038-8291

spectrometer CEP-01 «Elvax Light» and carbon analyzer GOU-1. Results of spectral analysis of pipe areas are given in Table 1, which shows the content of the chemical element in the selected sample.

For metallographic studies the microsections were polished with diamond pastes of different dispersity. The microstructure was detected by chemical etching of the microsections in 4 % solution of nitric acid. Analysis of the type of microstructures, as well as their photographing, was performed in NEOPHOT-32 microscope at different magnifications with application of digital photocamera OLYMPUS.

Obtained results and their discussion. Analysis of chemical composition of base metal (Table 1) showed that the pipe metal corresponds to steel of X12CrMo5 grade that reflects the chemical composition of metal of this steel manufactured by different foreign companies (Acroni, Bohler Welding Group, Tien Tai Electrode Co. Ltd., etc.). On the whole, analysis results are close, and correspond to the local analog of medium-chromium steel 15Kh5M.

Here, the somewhat lowered content of chromium and copper, as well as higher content of carbon in the metal, compared with the data of LAVIMONT BRNO Certificate should be noted. Presence of chromium in the solid solution determines formation of phase components, and also influences increase of strength properties, and metal susceptibility to brittle fracture, respectively. Note the considerable increase of sulphur and phosphorus, compared to the Certificate data. More over, based on EU Standard, sulphur content should not be higher than 0.005 %. Moreover, the Certificate does not specify the titanium content which is linked to nitrogen content, and which was detected in the presented fragments.

Metallographic analysis of the pipe base metal showed that its structure consists of ferrite matrix, alloyed by chromium and molybdenum, and dispersed carbides. Traces of general corrosion in the form of rust islands are observed both from the side of the pipe outer and inner surface. At intensive etching the carbide phase becomes more noticeable. In addition, in the middle sections along the sheet thickness, particularly in the longitudinal direction, the structural inhomogeneity of metal is clearly revealed in the form of alternating narrow dark and wider light bands, which is probably related to different content of carbon (Figure 2).

Macrostructure of welded joints is shown in Figure 3. The shape of the longitudinal weld looks like a cone. It is quite probable that prebending of the edges was not performed during pipe forming from a sheet. Considering that the longitudinal welds, having such a shape, are spaced around the ring at sequential joining

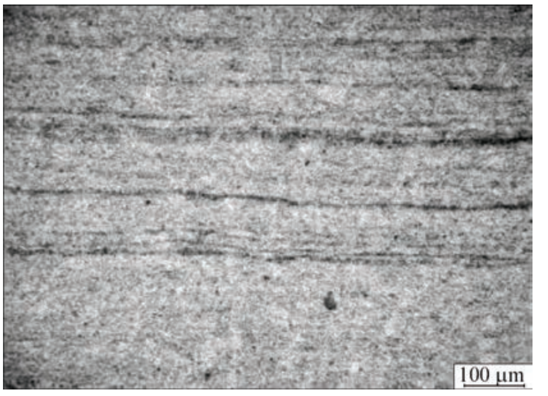

Figure 2. Base metal microstructure

of the shells by a site weld, additional welding stresses are known to develop because of violation of conjugation of the surfaces being welded. Circumferential site welds (Figure 3, *b*) also have certain defects. First, the height of the reinforcement bead, which should not be more than 2.5–4.0 mm, exceeds these values in a number of cases, similar to the longitudinal welded joint. Moreover, a lot of lacks-of-penetration and considerable contraction of the root layer are found.

It should be noted that at comparison of longitudinal welded joints made at the manufacturing plant and circumferential welded joints, made in site, rather high-quality performance of plant joints, compared with site butt joints, is found. However, analysis of welded joint microstructure allowed revealing the zones of lack-of-fusion also in the longitudinal weld. So, a defect was detected in the transverse microsection of the longitudinal welded joint, which is located on the boundary of the filling layer and by its shape repeats the contour of the bead in the weld pool (Figure 4). The defect area (in the plane, shown in the photo) reaches the size of 0.3×2 mm.

Despite the fact that the main problems in welding of high-strength steels are related to the fact that the welded joints are susceptible to cold cracking [4], this defect of the welded joint belongs to the category of defects of interbead lack-of-fusion. At the same time,

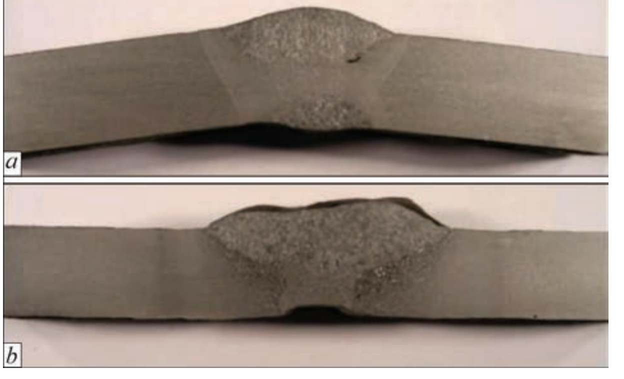

Figure 3. Macrostructure of welded joints: longitudinal (*a*) and circumferential (site) (*b*)

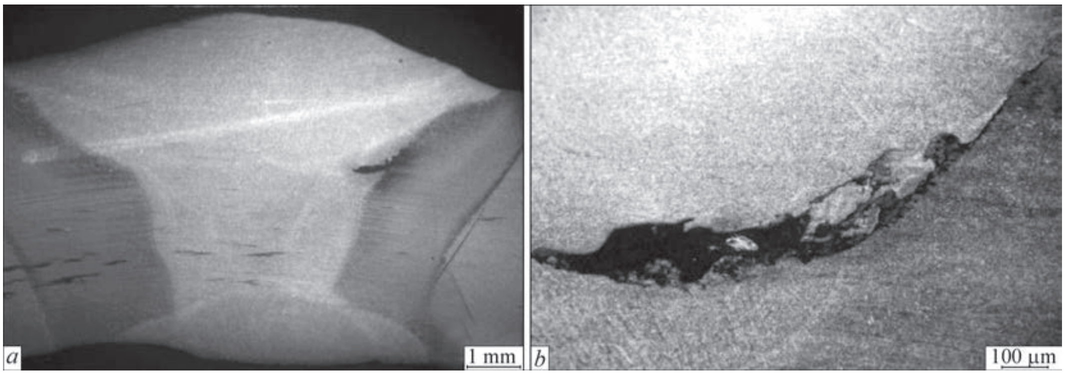

Figure 4. General view of the cross-section of the longitudinal welded joint (*a*) and interbead lack-of-fusion (*b*)

Figure 5. Delamination in the fracture of samples at tensile testing of longitudinal welded joints

similar defects are absent in the site welded joint in the part of the pipe, preserved after failure (Figure 3, *b*).

The microstructure of the circumferential weld metal is similar to that of the longitudinal weld, and also consists of a ferrite matrix, alloyed by chromium and molybdenum and finely-dispersed carbides.

Analysis of the results of mechanical testing showed that the metal of the studied pipe fragments has high strength characteristics at a sufficient level of ductility (Table 2). Here, the metal is practically isotropic in the sheet plane. However, as will be shown below, at tensile testing of welded joints no delamination was found in the sample neck (Figure 5) that is, most probably, due to anisotropy in Z-direction [5–7].

For evaluation of welded joint resistance to static and dynamic loads, the samples were cut out from both the longitudinal and circumferential welded joints (Table 3). As at tensile testing of welded joints fracture runs far from the deposited metal of the weld in all the cases, in the area of transition from the HAZ to the base metal, the mechanical characteristics (Table 3) represent the properties of the base (Table 2), rather than the deposited metal. Here, the yield limit, ultimate strength and relative elongation are 15–20 % higher in the longitudinal joints than in the circumferential ones.

Obtained results showed that unlike tensile testing (Table 3), at impact toughness testing of base metal the anisotropy phenomenon is manifested also in the

Table 2. Results of tensile testing of the base metal

Sample orientation	Yield limit σ_y, MPa	Ultimate strength σ_t, MPa	Relative elongation δ_5, %	Reduction in area ψ, %
Along the pipe axis	516.8–518.6	677.1–678.8	24.1–24.7	77.5–77.9
In the circumferential direction	515.1–516.8	674.3–676.4	24.8–25.3	73.3–77.5

Table 3. Results of tensile testing of welded joints

Welded joint	Yield limit σ_y, MPa	Ultimate strength σ_t, MPa	Relative elongation δ_5, %	Reduction in area ψ, %
Circumferential	451.5–485.5	590.4–629.6	18.9–19.7	72.0–75.1
Longitudinal*	520.1–560.9	667.0–672.5	23.5–24.0	73.0–73.1
*Delamination is observed in the rupture site.				

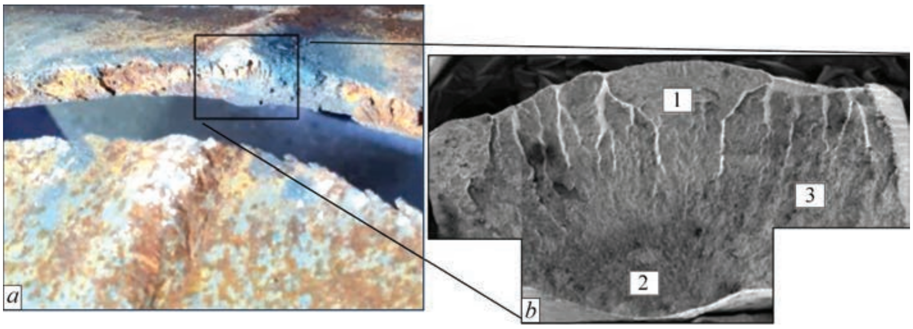

Figure 6. Appearance of a sample with the area of the start of pipe fracture in the longitudinal weld (*a*) and of the crack initiation region (*b*); *b* — ×10

rolling plane (Table 4). It leads, first of all, to different values of impact toughness along and across the rolling direction at room temperature, as well as to the spread of values at different testing temperatures [7].

Analysis of the influence of notch location on impact toughness values showed that at testing temperature of 20 °C at the notch location in the weld center, the impact toughness values of the longitudinal weld are 5 times higher than similar values of the circumferential weld, and at testing temperature of –10 °C they are more than 9 times (Table 4).

Note the inadmissibly low values of impact toughness of the site weld, particularly at minus temperature. So, for instance, in keeping with [8], the value of impact toughness in welded joints on samples with a sharp notch (*KCV*) in the weld center and on the fusion line at minimum service temperature should be not less than 29.4 J/cm^2 for pipes of 610–1020 mm diameter and 39.2 J/cm^2 for pipes of 1067–1420 mm diameter.

As the curvilinear shape of the fusion zone should be taken into account when making the notch in it, the spread of the results can be considered natural. However, in this case also the higher and more stable values of impact toughness of the longitudinal joint should be noted, as well as unstable values of impact toughness of the site joint, particularly at testing temperature of –10 °C (Table 4).

Thus, the performed laboratory studies that include determination of chemical and structural composition of the metal, allow stating that the pipe metal corresponds to the medium-chromium steel of X12CrMo5 grade. Here, it should be noted that mechanical testing revealed some indications of rolled stock anisotropy in the transition to the HAZ, which are manifested, primarily, in typical delamination of base metal that agrees with the concepts presented in work [5]. As regards the weld metal, extremely low and unstable values of impact toughness of site welded joints were established at impact bend testing, particularly, at minus temperature. At the same time, a defect in the form of interbead lack-of-fusion was revealed in the longitudinal weld. As will be shown below, this defect could exactly be one of the triggers, which led to fracture of the studied process pipeline.

Investigations of fracture surface. Visual-optical analysis of a fragment of broken pipe showed that the area of maximum opening of the crack is located in the region of the longitudinal weld crossing the HAZ of the circumferential weld (Figure 6). Here, it was found that the macroscopic features of the crack passing, namely the chevron pattern, change from one direction to the opposite one exactly in this region that was classified as the point of the start of pipe destruction.

Comparison of macro- and microstructure of the longitudinal welded joint (Figure 3, *a*; Figure 4) and morphology of fracture surface (Figure 6, *b*) allowed distinguishing three main areas in the destruction center: *1* — facing layer with filling layers; *2* — root layer; *3* — near-weed zone.

The facing layer is characterized by the dendritic structure in the fracture (Figure 6, *b*) that formed during liquid metal solidification in welding. Along-

Table 4. Results of impact bend testing of Charpy samples (*KCV*)

Number	Area of sample cutting out	Point of making the notch	*KCV*, J/cm^2	
			–10 °C	20 °C
1	Circumferential weld	Fusion zone	15.0–60.0	22.9–32.4
		Weld center	8.3	25.9–29.4
2	Longitudinal weld	Fusion zone	29.3–50.8	59.1–95.2
		Weld center	36.0–78.6	157.6–157.7
3	BM in the longitudinal direction	–	34.2–54.5	139.5–149.1
4	BM in the circumferential direction	–	32.7–34.5	159.7–280.2

Note. Notch through pipe wall thickness.

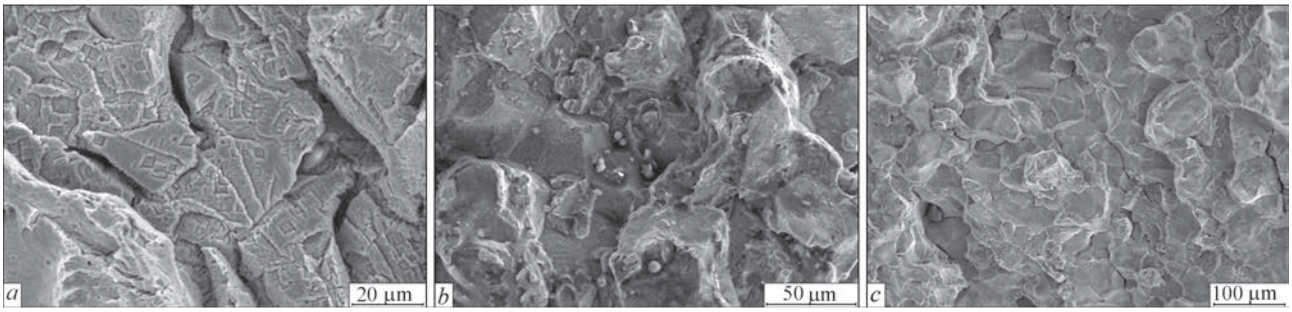

Figure 7. Fracture mode: *a* — facing weld; *b* — root weld; *c* — near-weld zone

side fracture in the primary dendritic structure, also cleavage facets and twins, characteristic of the secondary structure, are observed in the fracture [9]. In both the cases, formation of secondary cracks is in place (Figure 7, *a*, *b*), which cross the fracture surface. Presence of a viscous component in the fracture in the form of river pattern should be also noted. Appearance of secondary cracks, combined with tough regions against the background of overall brittleness is indicative of instability of crack propagation.

Analysis of fracture in the root layer showed that fracture occurred on the boundaries of secondary grains and has a stone-like nature (Figure 7, *b*). This region turned out to be strongly oxidized. Appearance of corrosion products is obviously related to the results of diffusion penetration of active elements (oxygen, hydrogen, carbon) into the root weld from the inner surface of the pipe in operation.

The fracture surface in the near-weld zone (Figure 7, *c*) is also characterized by stone-like fracture with enrichment by sulphur and phosphorus between the grains.

Thus, considering the possibility of appearance of underbead defects in the longitudinal welded joint (Figure 3, *a*; Figure 4), it is possible that such lacks-of-fusion or solidification microcracks could provoke initiation of brittle cracks at the initial stage of destruction. Their further propagation was, probably, promoted by a number of other reasons, for instance, presence of residual welding stresses due to violation of postweld heat treatment; failure to follow the pressing mode; poor design of pipeline fitting, etc. Here, the macrocrack propagated from the destruction center to both sides around the pipe ring which indicates that the axial stresses in the pipe under the impact of internal pressure are much higher then the hoop stresses. This assumption requires further study.

Conclusions

1. It is determined that the base metal of the broken pipe fragment belongs to medium-chromium steel by its composition that corresponds to local analog 15Kh5M, with a typical microstructure, consisting of equiaxed ferrite base, alloyed by chromium and molybdenum and dispersed carbides.

2. It is shown that crack propagation from the start of its initiation to both sides around the ring occurs in the brittle mode that is indicative of a typical chevron-type pattern of the fracture surface, which can be related to presence of high residual stresses, most probably due to violation of their relieving technology.

3. It is found that the start of fracture is located in the point of the longitudinal weld crossing the HAZ of the circumferential (site) weld, and it was triggered by defects in welds, in particular, interbead lacks-of-fusion. Here, exceeding the normative values of the reinforcement bead height was detected, which is inherent to both kinds of joints. More over, a lot of lacks-of-penetration are found that is, largely, characteristic for a site circumferential weld.

1. *Girgin* Serkan, K. (2015) *Elisabeth Lessons Learned from Oil Pipeline Natech Accidents and Recommendations for Natech Scenario Development – Final Report*. ©EU. Abstract, Published.
2. Kushnareva, O.V., Golubaev, D.V. (2018) Analysis of accident causes on objects of main gas-and-oil pipelines*:* Problems and solutions. *Master's J.*, **1**, 37–43.
3. Kuznetsova, N.V., Krasnokutsky, A.N. (2012) Experience of calculation and design of transfer pipelines. *Tekhnologii Nefti i Gaza*, **3**, 54–59 [in Russian].
4. Lobanov, L.M., Poznyakov, V.D., Makhnenko, O.V. (2013) Formation of cold cracks in welded joints from high-strength steels with 350-850 MPa yield strength. *The Paton Welding J.*, **7**, 8–13.
5. Lobanov, L.M., Girenko, V.S., Rabkina, M.D. (2001) Anisotropy of crack resistance characteristics as one of the causes of crack initiation in welded bridge spans. In: *Diagnostics, life and reconstruction of bridges and building structures,* Transact., Lviv, Kamenyar, Issue 3, 138–147 [in Russian].
6. Farber, V.M., Khotinov, V.A., Belikov, S.V. et al. (2016) Separations in steels subjected to controlled rolling, followed by accelerated cooling. *Physics of Metals and Metallography*, 117, 407–421.
7. Usov, V.V., Girenko, V.S., Rabkina, M.D. et al. (1993) Influence of crystallographic texture on anisotropy of fracture characteristics of low-alloyed steel of controlled rolling. *Fizikokhimicheskaya Mekhanika Materialov,* **2**, 47–52 [in Russian].
8. *TU 1381-003-47966425–2006: Steel longitudinal welded pipes with an outer diameter of 610–1420 mm* [in Russian].
9. Fellous, J. (1982) *Fractography and atlas of fractograms.* Moscow, Metallurgiya [in Russian].

Received 01.02.2021

https://doi.org/10.37434/tpwj2021.03.05

INVESTIGATION OF TEMPERATURE STATE OF COPPER PLATES IN THE WELD ZONE AT FRICTION STIR WELDING

M.A. Polieshchuk, A.V. Shevtsov, I.V. Dotsenko, V.M. Teplyuk, O.V. Kolisnichenko and **L.M. Malakhova**
E.O. Paton Electric Welding Institute of the NAS of Ukraine
11 Kazymyr Malevych Str., 03150, Kyiv, Ukraine. E-mail: office@paton.kiev.ua

Chromel-alumel thermocouples were used to study the temperature state of 10 mm copper plates at simulation of the process of friction stir welding. Thermocouples were welded on in blind holes located along the line of welding tool movement that allowed recording the copper temperature at the moment of weld formation in different welding modes. In the studied range of variation of process parameters, the metal temperature is mainly influenced by the area of interaction of the welding tool working surface with the plate, while the speed of tool rotation has a minor effect. At the moment of weld formation the metal temperature varied from 528 up to 980 °C in different modes. 13 Ref., 3 Tables, 3 Figures.

Keywords: friction stir welding, copper plates, thermocouples, welds, formation temperature

Relevance and objective of the work. A new technology of joining metal materials – friction stir welding (FSW), patented by The Welding Institute (Great Britain) in 1991, has been developed recently [1]. This technology is realized, using a special rotating tool (Figure 1), which is immersed into the butt of the parts being welded, and moves along it. The working part (*1*) of this tool has a central rod — pin (*2*), designed for heating by friction the edges being welded. Located above the pin is the shoulder (*3*), which forms the weld. The tool working part is fastened in mandrel (*4*), which is inserted into the welding machine spindle.

Heating of edges being welded is performed due to the tool friction against their surfaces. The heat created by friction and deformation, heats the metals being joined to a plastic state, while the linear movement of the rotating tool, leads to stirring of the plasticized metal volumes, resulting in joint formation. The shape, dimensions and hardness of the material of the tool working part are determined by the welded material grade and its thickness.

FSW technology differs from all kinds of fusion welding by absence of the liquid metal phase in weld formation zone, the solidification of which may lead to defects in the form of shrinkage and liquation cracks and porosity. Thus, this technology allows obtaining a better quality weld, and also joining dissimilar metals and alloys, which cannot be welded by other welding methods. FSW technology was first created for welding relatively low-melting materials, mainly aluminium alloys [2]. Work on FSW application for copper [3] and steels [4, 5] began somewhat later.

When developing the FSW technology, it is important to know the temperature level in the zone of weld formation. This information allows determining the optimal process parameters of welding, namely frequency and speed of the tool linear movement, and also assessing the resistance of the material of its working part. Unfortunately, the main scope of data on metal temperature in the zone of weld formation is assessed by the results of measurement of metal temperature in the zone located in immediate vicinity of the weld.

The maximum values of temperature at FSW of some metals, published by different authors, are summarized in Table 1. One can see from the Table that

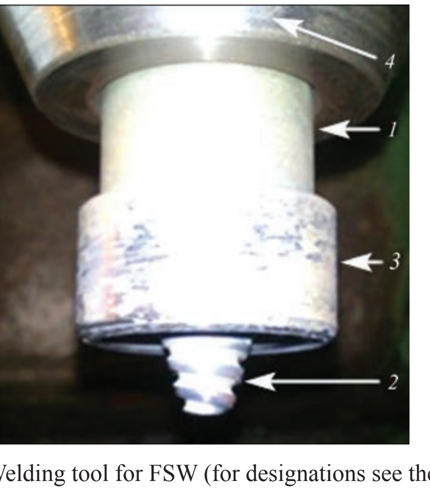

Figure 1. Welding tool for FSW (for designations see the text)

M.A. Polieshchuk — https://orcid.org/0000-0002-5992-4641, A.V. Shevtsov — https://orcid.org/0000-0001-9599-4842, I.V. Dotsenko — https://orcid.org/0000-0002-1040-0409, V.M. Teplyuk — https://orcid.org/0000-0002-0463-0689, O.V. Kolisnichenko — https://orcid.org/0000-0003-4507-9050, L.M. Malakhova — https://orcid.org/0000-0003-1388-6536

Table 1. Metal temperature in the vicinity of welds at FSW

Number	Alloy	Measurement location	Temperature, °C	Ref.
1	AA6061-T6	On weld surface and in the center	425	[6]
2	AA7075-T651	~0.6 mm (0.02") below the top that is adjacent to the stirring zone	475	[6]
3	AA6061-T6	–	310	[6]
4	AA1050	Close to the lower limit of stirring zone	310	[6]
5	AISI-1018	Interface of the shoulder and processed item	990	[6]
6	AA2195-T8	Region adjacent to pin edge	450	[6]
7	AZ-31	In the HAZ	360	[6]
8	Pure copper C1 1000	Same	530	[7]
9	Pure copper Cu-OF	Region adjacent to pin edge	850	[3]
10	Al alloy 1561	On the boundary of weld metal with base metal	475	[8]

all the given in it temperature values are below the solidus temperature of the respective alloys.

PWI is working to develop FSW technologies for different metals [9, 10]. Particular attention is given to problems of welding copper and its alloys by FSW method, as these materials are widely used in metallurgical engineering for manufacture of different types of water-cooling crucibles [11]. In addition, the structures of welds from dissimilar metals with different solubility of elements in the solid phase were studied for the case of protective layer deposition on copper bases [12].

Materials and procedure of investigations. At development of optimal process parameters of FSW of copper detailed studies of the temperature state of copper plates in the zone of weld formation were conducted. Temperature measurement and recording was performed at simulation of FSW process on rectangular plates from M1 copper 10 mm thick with application of chromel-alumel thermocouples, installed in blind holes made in the plate body. The holes were made to have such depth that the distance from the thermocouple junction to the pin edge passing above it, was not more than 1 mm. Thermocouple junctions were fastened to the hole bottoms by capacitor-discharge welding, and their cold ends were connected to signal amplifier. After amplification the thermo-EMF signal was saved in the computer through analog-digital amplifier NI USB-6009, National Instrument. The sampling rate was 2 s^{-1}. Labview development environment was used for organizing the recording and visualization of temperature change during the entire technological process. This measurement schematic allowed simultaneously recording the readings of four thermocouples with 10 % calculation error. In order to record the temperature, two thermocouples were located along the line of welding tool movement, thermocouple No.1 was placed in the point of pin immersion into the plate body, while thermocouple No.2 was located at 40 mm distance from it. Testing was preceded by calibration of thermocouples, fastened in the plate body at 0 and 100 °C. Temperature, recorded by the thermocouples, was compared with the readings of control thermometer of TR-101 grade with division value of 0.1 °C. The error of metal temperature measurement did not exceed 4 %.

Two welding tools with the same shoulders of 34 mm diameter and pins of different dimensions were used during investigations. One tool had a larger pin with 16 mm diameter of the base, 5.5 mm tip diameter and 8.5 mm height. The other one had a pin of smaller dimensions of 10, 3.5 and 6.5 mm, respectively. The axis of weld tool rotation was deviated from the vertical by 1.5° to the side opposite to the direction of horizontal movement.

Two groups of experiments were conducted. In the first group, just the pin was immersed into the plate body, while the shoulder was at 0.1 mm distance from its surface. In the second group of experiments a standard FSW process was simulated.

Investigation results and discussion. In the first group, the process started from the pin immersion into the plate surface above the point of location of thermocouple No.1. Before that 0.1 mm foil was pasted to the plate surface in this site. At the moment the shoulder lower edge touched the foil, the tool immersion was stopped, and its horizontal movement was began in the direction of thermocouple No.2. During investigations temporary cutting off was performed in the graphs of thermocouple readings: the first at the moment of the pin edge touching the plate surface, the second — at the moment of the start of the tool horizontal movement, and the third — at the moment of the pin passing over the second thermocouple. Table 2 gives the values of FSW process mode parameters: welding tool rotation frequency (RF), its horizontal movement speed (MS), as well as the specified shape of welding tool working parts with a large (LP) and small (SP) pins. In addition, the Table gives the maximum temperature values, recorded in these modes by the first thermocouple (t_1) and second thermocouple (t_2).

Two curves of temperature change in the studied points of the copper plates were derived in each FSW mode. Figure 2 shows examples of temperature curves, obtained in the first (*a*) and second (*b*) process modes of

FSW (see Table 2). At other modes, graphs of a similar shape were obtained that differ by the values of maximum temperature recorded by the thermocouples.

In the point of immersion of the welding tool into the plate body, copper temperature starts increasing right after the pin edge touches its surface (cut-off 1). As the pin goes down, the temperature rises and reaches its maximum at the moment the introduction process is over. After the start of horizontal movement of the working tool (cut-off point 2) the temperature in this site decreases, because of removal of the heat evolution source from the measurement point. Temperature curves, recorded by the first thermocouples, show that at the moment of the welding tool immersion, the heat evolves predominantly due to friction. This is confirmed by analysis of maximum temperature values in these sites at FSW in different modes (see Table 2). Indeed, the maximum temperature value mainly depends on the area of friction surface, while the influence of the frequency of welding tool rotation is insignificant.

The graphs of the change of copper temperature, fixed by thermocouples No.2, show that the start of temperature increase in these points lags behind the readings of the first thermocouple, as the heat is transferred to them due to heat conductivity. The delay time is determined by the velocity of temperature propagation in copper. After the start of horizontal movement of the welding tool, the power of the heat evolution source rises owing to additional heat from plastic deformation of metal near the pin. In the graphs, these temperature changes are reflected in the form of increase of the angle of inclination to the horizontal axis of temperature curves in thermocouples No.2. When the welding tool moves closer to the locations of the other thermocouples, further increase of the rate of temperature rise takes place. The magnitude of metal temperature reaches the maximum values at the moment of the pin passing over thermocouple No.2 (cut-off 3).

Analysis of temperature values, given in Table 2, shows that the plate temperature in the locations of thermocouples No.2 is approximately 100 °C higher than in the points of the pin immersion. It is obvious that temperature increase in the location of thermocouple No.2 is the result of additional heat evolution, associated with plastic deformation of the plate material. This temperature essentially depends on the pin dimensions, i.e. on the area of interaction of the welding tool working part with the plate material. Maximum temperature was recorded by us at simulation of FSW with 1000 rmp frequency of the tool rotation. No influence of the speed of horizontal movement of the welding tool working part was found in the studied range.

Table 2. FSW mode parameters in the first group of experiments

Mode number	Pin shape	RF, rpm	MS, mm/min	t_1, °C	t_2, °
1	SP	800	40	216	312
2	LP	800	40	438	557
3	LP	800	50	441	559
4	LP	1000	40	456	571

Analysis of temperature curves, given in Figure 2 suggested that two variants of heating the edges of the products being welded are possible at FSW of metal materials with high heat conductivity. At linear movement speeds smaller than the linear velocity of temperature propagation in the welded product material, metal preheating occurs ahead of the tool front, so that additional heat evolution from the tool operation takes place in more heated regions. Metal temperature at the moment of weld formation will rise with their length. If the welding tool speed is higher than the velocity of temperature propagation, metal preheating ahead of the rotating front is absent, and increase of weld formation temperature will not occur along the division line.

The velocity of temperature propagation in metals is determined by the thermal diffusivity, which is numerically equal to the ratio of the coefficient of heat conductivity to specific heat, and has the dimension of m^2/s. This coefficient should be regarded as the surface area, ahead of the front of which increase of the metal

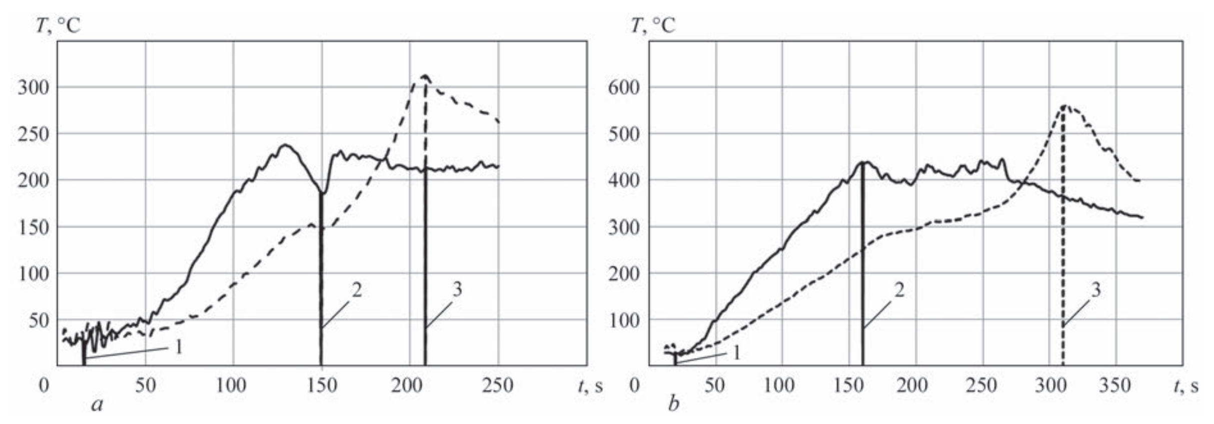

Figure 2. Graphs of the change of copper plate temperature during FSW: *a* — 800/40 SP; *b* — 800/40 LP (solid line shows temperature changes in the points of pin immersion; intermittent — in the location of the second thermocouple); 1, 2, 3 — temporary cut-offs (for description see the text)

Table 3. FSW mode parameters in the second experimental series

Mode parameters	Mode number									
	1	2	3	4	5	6	7	8	9	10
RF, rpm	800	800	800	1000	1000	1000	800	800	1000	1000
MS, mm/min	40	40	40	50	50	50	40	40	40	50
TD, mm	0.36	0.4	0.6	0.2	0.4	0.6	0.3	0.5	0.2	0.35
IA, mm^2	180.88	194.96	280.77	130.88	194.96	280.77	160.13	235.11	130.88	177.55
t_1, °C	–	–	–	–	–	–	644	588	428	660
t_2, °C	700	710	900	530	780	980	670	695	528	715

initial temperature occurs in a unit of time. Theoretically, for a semi-closed body such a surface will be a widening half-sphere, in the center of which a point heat source is acting. For plates, such a surface will be the upper spherical segment of the half-sphere, the height of which is equal to the plate thickness. The radius of the half-sphere that expanded per a unit of time, can be regarded as the linear velocity of temperature propagation over the surface of the body or plates.

For different copper grades, the thermal diffusivity is in the range of 111.0–115.0 mm^2/s [13]. Here, the theoretical linear velocity of temperature propagation for copper plates 10 mm thick is equal to 108 mm/min on average. However, the real linear velocity of temperature propagation in the copper plates at FSW can be smaller than the theoretical value, as the working surface of the welding tool does not create a point heat source, while the plate proper is lying on a metal substrate with another thermal diffusivity value that makes corrections in the total surface area of the half-sphere spherical segment.

The real velocity of temperature propagation in the copper plates 10 mm thick in different FSW modes was assessed by us experimentally. For this purpose, the lapse of time between the moments of the beginning of metal temperature rise in the points of location of thermocouples No.1 and No.2 was determined in the temperature curves (Figure 2). These data were the basis for determination of the average velocity of temperature propagation for all FSW modes. This velocity was equal to approximately 100 mm/min. Thus, the speed of horizontal movement of the welding tool of 100 mm/min, can be optimal to ensure a constant temperature in the joint zone along the entire weld length for the copper plates 8 to 12 mm thick (although this assumption requires additional experimental verification). In the second group of experiments, simulation of the standard FSW process with different frequency of rotation and speed of welding tool movement and different area of interaction of its working part with the plate, was performed. This area was determined by the depth of the trace left by the shoulder on the plate surface after welding, using the tool drawing in SOLIDWORK design program.

Thus, considering the errors, arising at measurement of all the parameters, which determine FSW modes (rotation frequency, movement speed, trace depth, accuracy of placing the thermocouples in the plate body), the overall computed error of temperature measurements, when performing the second group of experiments, was equal to 20 %. Specific parameters of the studied FSW modes are given in Table 3, which additionally shows the shoulder trace depth (TD) and area of the tool interaction with the plate (IA).

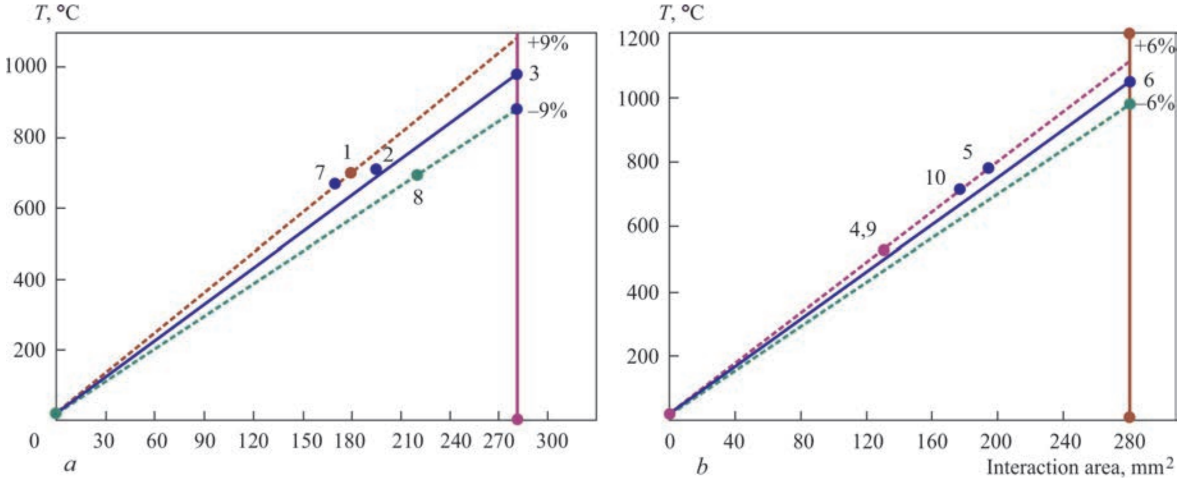

Figure 3. Dependence of copper temperature on interaction area: *a* — RF 800 rpm; *b* — 1000 (point numbers correspond to FSW modes, Table 3)

The shape of temperature curves, derived in all FSW modes in the second series of experiments, is similar to those given in Figure 2. An essential point of difference is the value of metal temperature. This temperature is lower than that of copper melting in all FSW modes, given in the table. At metallographic studies no cast structures were found in the weld cross-sections even in FSW modes, at which the metal temperature reached 900 and 980 °C. Thus, the results of experimental studies convincingly confirm that at FSW of copper the liquid metal phase is absent at the moment of weld formation.

In the studied range of process parameters variation at FSW, the metal temperature at the moment of weld formation mainly depends on the area of welding tool interaction with the plate body.

Figure 3 shows the graphs of these dependencies at welding tool rotation frequencies of 1000 (*a*) and 800 rmp (*b*). These graphs are plotted by generalization of maximum values of metal temperature at the respective rotation frequency (Table 3). The error of plotting the graphs was smaller than the computed error of temperature measurement in the conducted experiments. One can see from the graphs that the metal temperature changes significantly at minimum change of the depth of welding tool immersion into the plate body. This fact accounts for a wide range of experimental values of metal temperature at the moment of weld formation at FSW of specific metal materials given in publications. In the studied range, the frequency of welding tool rotation has a minor influence on metal temperature at weld formation. No influence of the change in the speed of welding tool movement from 40 to 50 mm/min was found.

The next paper will give the results of studying the metal temperature at the moment of weld formation in a wide range of change of rotation frequency and speed of welding tool horizontal movement, as well as distribution of temperature values in the weld cross-section.

Conclusions

1. At FSW of copper, the temperature of weld formation is mainly determined by the area of interaction of the working part of the welding tool with the plate body. In the studied range at minimal interaction area, the copper temperature in the site of weld formation is equal to 528 °C, and at maximum temperature it reaches 980 °C.

2. In the studied range, the rotation frequency of the welding tool has a minor influence on copper temperature in the sites of weld formation.

3. Analysis of thermal cycles at FSW of plates from materials with high heat conductivity at different process parameters of welding suggests two variants of weld formation. They differ by the nature of the change of metal temperature along the welds at the moment of their formation, depending on speeds of horizontal movement of the welding tool. At tool speeds, which exceed the linear velocity of temperature propagation in the welded product material, the metal temperature during weld formation will remain constant along their entire length. Such a variant of weld formation at FSW of copper plates of 8–12 mm thickness, by preliminary estimates, is possible at speeds of the tool horizontal movement, exceeding 100 mm/min. At tool movement speeds lower than the linear velocity of temperature propagation in the welded product material, the metal temperature at the moment of weld formation will rise with their length. In this case, forced cooling of the welded product should be used, in order to obtain sound welds.

1. Thomas, W.M. (1991) *Friction stir butt welding.* Pat. 9125978.8 GB, Publ. 01.12.91.
2. Dawes, C., Thomas, W. (1995) *TWI Bull.*, **6**, Nov/Dec.
3. Savolainen, K. (2012) *DPh: Friction stir welding of copper and microstructure and properties of the weld.* Aalto University publication series 13/2012.
4. Manish P. Meshram, Basanth Kumar Kodli, Suhash R. (2014) Dey: Friction stir welding of austenitic stainless steel by pcbn tool and its joint analyses. In: *Proc. of 3rd Int. Conf. on Materials Processing and Characterization (ICMPC 2014).*
5. Brian T. Thompson. (2010) *Thesis: Tool degradation characterization in the friction stir welding of hard metals.* The Ohio State University.
6. De P.S., Kumar N., Mishra R.S. (2005) Fundamentals of Friction Stir Welding. *ASM Handbook*. **6A**, 186–199.
7. Hwang, Y.M., Fan, P.L., Lin, C.H. (2010) Experimental study on friction stir welding of copper metal. *J. Materials Proc. Technology*, **210**, 1667–1672.
8. Pavlova, V.I., Alifirenko, E.A., Osokin, E.P. (2009) Study of temperature-time conditions of welding heating, structure and properties of metal of butt joints from aluminium-magnesium alloy produced by friction stir welding. ISSN 1994-6716. *Voprosy Materialovedeniya*, **4**, 60. St.-Petersburg, TsNII KM Prometey [in Russian].
9. Grigorenko, G.M., Poleshchuk, M.A., Adeeva, L.I. et al. (2016) Peculiarities of structure of Cu-Cu, Ni-Cu and steel-Cu joints produced by overlap friction stir welding method. *The Paton Welding J.*, **5–6**, 75–80.
10. Krasnovsky, K., Khokhlova, Yu.A., Khokhlov, M.A. (2019) Influence of tool shape for friction stir welding on physico-mechanical properties of welded joints of EN AW 6082-T6 aluminium alloy. *Ibid*., **7**, 9–15 [in Russian].
11. Grigorenko, G.M., Adeeva, L.I., Tunik, A.Yu. et al. (2015) Restoration repair of slab copper moulds of MCCB. Structure and properties of metal in the joint zone. *Sovrem. Elektrometal.*, **1**, 44–49 [in Russian].
12. Grigorenko, G.M., Adeeva, L.I., Tunik, A.Yu. et al. (2014) Structural features of FSW joints of metals with different element solubility in the solid phase. *The Paton Welding J.*, **4**, 13–23.
13. https://www.bnl.gov/magnets/Staff/Gupta/cryogenic-datahandbook/Section 15.pdf

Received 02.02.2021

https://doi.org/10.37434/tpwj2021.03.06

IMPROVEMENT OF THE SURFACING TECHNOLOGY FOR LARGE-SIZED BACKUP ROLLS OF HOT ROLLING MILLS

L.K. Leshchinskyi, V.M. Matviyenko, V.P. Ivanov, K.K. Stepnov and **E.I. Vozyanov**
Azov State Technical University
7 Universytetska Str., 87555, Mariupol, Ukraine. E-mail: matviyenkovn@gmail.com

It is shown that when surfacing large-sized backup rolls of hot rolling mills made of 90KhF steel, the limited weldability of steel leads to the need to select the thermal mode of surfacing that ensures the required performance of the deposited layer. The choice of materials and technology of deposition of the transition zone from the base metal to the working layer determines appearance of hardness dips and formation of a «soft interlayer», which leads to occurrence of spalling. Elimination of such dips depends on the choice of the deposition mode of each of the layers, in accordance with the composition and size of the electrodes used. It is shown that application of 1.0 mm thick 08kp, 30KhGSA, 25Kh5FMS strip electrode for surfacing makes it possible to obtain a smooth (without dips and bursts) change in hardness by the height of the multilayer composition, which contributes to an increase in spalling resistance when the height of the deposited layer decreases during the operation of the roll. The high efficiency of the surfaced backup rolls was confirmed during industrial development of the surfacing technology of the rolls and their long-term operation in the hot rolling mill. The developed and implemented route scheme for movement of the deposited and new backup rolls (the share of deposited rolls reached 30 %) in the roughing group of stands of mill 2000 of the Cherepovets Metallurgical Plant made it possible to ensure the operating time of surfaced rolls commensurate with that of new rolls as to the tonnage of rolled products. 12 Ref., 4 Tables, 2 Figures.

Keywords: backup rolls, 90KhF steel, surfacing, underlayer, transition zone, composition of layers, hardness, spalling of the surfaced layer, strip electrode, surfacing mode, hot rolling mill, roughing stand, roll route, operating time of surfaced rolls

When developing the surfacing technology for large-sized forming rolls with barrel diameter of 800–1600 mm and 1500–4500 mm length, it should be taken into account that the extent of wear may require deposition of not less than 12–15 layers [1–6]. The zone of transition from the roll material to the working layer should form in the first deposited layers of such a composition. The correspondence of mechanical properties of this zone to applied loads and its cracking resistance depend on the structure and properties of the near-weld zone of the HAZ, chemical composition of the deposited metal that forms the transition zone, absence of hardness dips and peaks here [7]. Therefore, the task of selection of materials and technology of deposition of the zone of transition from the base metal to the working layer is regarded as one of the main problems, as performance of the surfaced backup rolls largely depends on it.

In the thermal mode of deposition of large-sized backup rolls from high-carbon steel, selection of preheating temperature has the most important role, which it is rational to consider for several roll steels: 40Kh (40KhN), 55Kh (55KhNM) and 90KhF which differ by carbon content and weldability (cracking susceptibility). In order to lower the cracking susceptibility of the roll, thermal mode of surfacing is used which reduces the probability of formation of hardening structures in the HAZ metal, and surfacing materials are applied, which allow increasing the metal ductility, lowering diffusible hydrogen concentration and level of residual tensile stresses. Proceeding from cold cracking susceptibility, carbon equivalent C_c is a characteristic used for assessment of weldability [8]. Mathematical description of this value is proposed, with consideration of the minimum critical time of weld metal cooling, dependent on the cooling rate and required for a complete martensite transformation:

$$C_e = C + (Mn + Si)/6 + (Cr + Mo + V + W)/5 + + (Ni + Cu)/15.$$

Results of calculation of carbon equivalent values by the dependence proposed by IIW, are given in Table 1.

Long-time process of concurrent heating results in thermal equilibrium of the roll being surfaced, and its cooling rate becomes considerably lower than the critical value. For forming rolls, the concurrent heating temperature is selected significantly higher than that of martensite transformation M_s (see Table 1). For 90KhF steel having a high stability of overcooled

L.K. Leshchinskyi — https://orcid.org/0000-0002-7473-7510, V.M. Matviyenko — https://orcid.org/0000-0002-8713-1630,
V.P. Ivanov — https://orcid.org/0000-0003-3339-7633, E.I. Vozyanov — https://orcid.org/0000-0002-2034-1270

Table 1. Carbon equivalent of roll steels

Steel grade	Carbon content, %	Carbon equivalent C_c	Temperature of martensite transformation M_s, °C	Critical cooling time Δt_m, s*
40Kh	0.36–0.44	0.74	280	–
50KhNM	0.50–0.60	0.98	260	2000
90KhF	0.80–0.90	1.35	240	–

*By calculated data of [8].

austenite, the concurrent heating temperature of 380–400 °C provides isothermal conditions for complete decomposition of austenite and determines formation of pearlite structure [6].

It is advisable to consider the influence of metal composition and surfacing technology on the properties of the zone of transition from the base metal (90KhF steel) to the working layer, having, first of all, more precisely determined the real content of carbon in the first deposited layers. With this purpose, it is necessary to determine the degree of weld dilution by base metal (previous layer) for the applied wire and strip electrode dimensions, as well as parameters of the mode of backup roll deposition (Table 2). At deposition of an underlayer on 90KhF steel, using 5 mm Np-30KhGSA wire the carbon content in the underlayer is equal to 0.64 %, and at the possible application of split electrode it is not less than 0.42 % (Table 3). Even with thorough following of the surfacing technologies, which become much more complicated, as well as the required preparation of surfacing materials, it is difficult to ensure the necessary technological strength, while preventing cracking. In the structure of 30KhGSA underlayer, deposited on 90KhF steel, at a high content of carbon, the martensite is characterized by a higher dislocation density and lower ductility. Such a structure of the underlayer fails in the intergranular cleavage mode with regions of tough pit fracture through the grain, then in 90KhF steel the fracture runs along the boundaries of surface-melted grains, and then it goes into intragranular cleavage [9].

Table 3. Carbon content in 1–3 layers at deposition on 90KhF steel (γ = 0.55)

Layer number	Carbon content, %	
	Np-30KhGSA	Sv-18KhGS
1	0.64	0.57
2	0.48	0.39
3	0.40	0.30

Cracking susceptibility decreases noticeably at deposition of an underlayer on a roll from 90KhF steel, using Sv-18KhGS wire. Compared to application of Np-30KhGSA wire, lowering of carbon content in the underlayer (below 0.60 %) (Table 3) does not lead to appearance of hardness dip at transition from bainite-martensite structure of the underlayer to pearlite structure of 90KhF steel. Carbon content of 0.18–0.22 % in the electrode is probably the maximum admissible one in the case of deposition of an underlayer on 90KhF steel. Note that a smooth transition from 40Kh steel to the deposited working layer of 25Kh5FMS without dips was obtained at application of PP-Np-12GKhMF wire for underlayer deposition [10]. In the case of application of this wire for surfacing of 90KhF steel the carbon content (at share of participation γ = 0.37) is equal to 0.35 % in the first layer, and 0.15 % in the third layer. At the same time, at deposition on steel with 0.67 % C, up to 1.20 % Mn, 0.40 % Si, and 0.15 % V, using flux-cored wire PP-AN-180MN (12Kh1NMFS), the deposited layer is characterized by finely-dispersed bainite-martensite structure, and high crack resistance [11]. Here, for 50KhS, 40KhGS, 35KhGS, 32Kh2GMS, 30KhG3MF, 30Kh2M2NF metal compositions, which form in the underlayer at surfacing of high-carbon or medium-carbon steel, the temperature of the start of martensite transformation is markedly lower than that of concurrent heating at surfacing of large-sized forming rolls [4, 6].

Appearance of deposited layer spalling on two backup rolls of hot rolling mill 1700 of Mariupol Ilich Metallurgical Works [7], is associated with metal hardness dip as a result of formation of a «soft inter-

Table 2. Parameters of the mode of underlayer deposition on backup roll from 90KhF steel

Electrode grade	Electrode dimensions, mm	Current, A	Penetration depth h_p, mm	Ratio of penetration depth to layer thickness h_p/δ	Share of dilution γ
08kp (rimmed)	50×0.5	450–550	1.5	0.37	0.23
08kp	40×1.0	500–600	1.9	0.47	0.45
30KhGSA	40×1.0	500–650	2.3	0.48	0.45
Sv-18KhGS	Ø5	600–700	9.0	1.50	0.55
Np-30KhGSA	Ø5	600–700	9.0	1.50	0.55
Np-30KhGSA	2×Ø4	700–850	6.0	1.20	0.37
PP-Np-12Kh1G1NM	Ø3.6	350–400	3.0	0.60	0.37

Note. Voltage of 30–32 V; υ_s = 15 m/h (for strip); υ_s = 30 m/h (for wire).

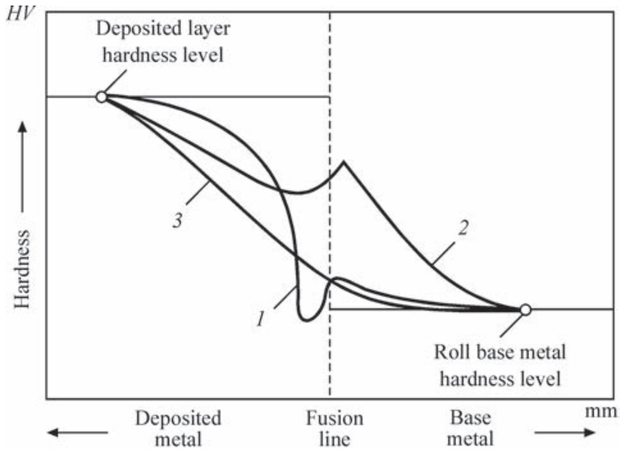

Figure 1. Nature of hardness distribution by the depth of the transition zone: *1* — with hardness dip in the underlayer region; *2* — with hardness increase near the fusion line; *3* — with smooth change of hardness from the underlayer to the working layer

layer» in the transition zone. Such a dip was observed both on the roll and on the reference sample (base metal is 90KhF steel, 08kp strip electrode of 50×0.5 mm cross-section was used in both cases for underlayer deposition). It should be noted that while in the reference sample reliable penetration was ensured and absence of lacks-of-fusion was controlled, during the process of underlayer deposition on the backup roll appearance of lack-of-fusion was quite probable that can provoke spalling. Thickness of «soft interlayer», as one can see from work [7, Figure 1], is not more than 3.5–4.0 mm, its hardness is lower than that of the base metal, which is followed by its abrupt increase up to the level of working layer hardness. Unlike the surfacing process, formation of «soft interlayer» in welds is related to the nature of the welding process, or to application of electrodes, for instance, of austenitic class, when the mechanical properties of weld metal differ markedly from those of the base metal (high-strength steel). In a multilayer composition, deposited on a backup roll, formation of a «soft interlayer» is not related to the nature of the process, but it caused by disadvantages of the surfacing technology. So, it was not taken into account that in case of deposition of an underlayer by a thin strip electrode, the penetration is minimal, and it is difficult to ensure reliable fusion with the substrate material. More over, the mode of deposition of the next layers, which ensures absence of dips in the zone of transition from the underlayer to the working layer, was not specified.

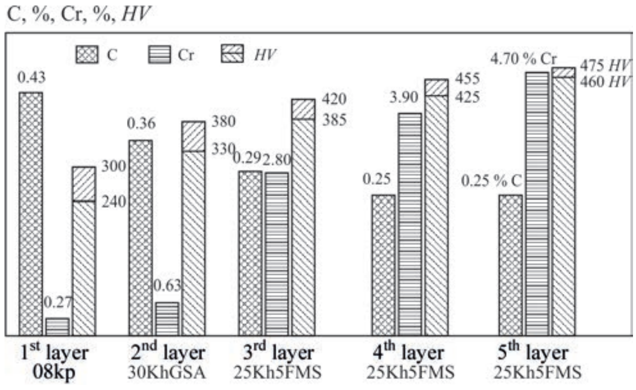

Figure 2. Chemical composition and hardness of transition zone layers at deposition with 40×1.0 mm strip electrodes on 90 KhF steel

When 1.0 mm strip electrodes are used, the substrate penetration depth (compared to 0.5 mm thick strip) becomes 1.5–1.7 times greater [5] that improves the fusion reliability, and abruptly lowers the probability of appearance of both defects of lack-of-fusion type, and hardness dips in the transition zone. At deposition of an underlayer on 90KhF steel by 08kp strip electrode the ferrite-pearlite structure fails in the viscous pit mode with tear regions. Deposition of the second layer by 30KhGSA strip, and then by 25Kh5FMS strip ensures a smooth transition of hardness from the underlayer to the working layer (Figure 1, curve *3*). The obtained layer compositions are characterized by satisfactory weldability that at the temperature of concurrent heating of the roll (up to 400 °C) allows preventing the deposited metal cracking.

The results of measurement of the transition zone extent on the deposited samples correspond to the presented in Figure 1 nature of hardness change for different variants of the technology of transition zone surfacing (Table 4).

Figure 2 presents the data for evaluation of changes in carbon, chromium content and hardness in the deposited layers of the transition zone at surfacing with 08kp, 30KhGSA, 25Kh5MFS strip electrodes of 40×1.0 mm cross-section (base metal share $\gamma = 0.45$).

Application of 25Kh5FMS strip for working layer deposition allows producing deposited metal with the structure of batch martensite with rather dispersed martensite racks. Hardness after deposition was *HV* 410 (*HSD* 58), impact toughness — 0.33 MJ/m^2, dynamic coefficient of stress intensity — 28.4 MPa·m$^{1/2}$, and fracture mode was transcrystalline

Table 4. Parameters of the transition zone for different variants of hardness distribution

Variant number	Nature of hardness distribution in the transition zone	Dimensions of the transition zone, mm
1	With hardness dip in underlayer region	4.0
2	With hardness rise near the fusion line	5.0
3	With a smooth change of hardness from the underlayer to the working layer	6.0–7.0

cleavage [9]. When this material is used for roll surfacing, it is necessary to take into account the effect of tempering after surfacing on hardness and crack resistance. Conducted studies show that the optimum tempering temperature was 600 °C. At this temperature the deposited metal hardness rises up to *HV* 450 (*HSD* 62). On the other hand, impact toughness is equal to 0.35 MJ/m^2, and the dynamic coefficient of stress intensity is 30.0 MPa·$m^{1/2}$.

Technology of surfacing large-sized backup rolls that ensures a smooth change of hardness by the deposited layer height became widely accepted in the Cherepovets Metallurgical Plant [4]. It required mastering Plant's own production of standard and new compositions of the surfacing strip [12]. Mastering the technology of surfacing large-sized backup rolls, their operation experience in the roughing stand of hot rolling mill 2000 of the Cherepovets Metallurgical Plant, allowed bringing the share of deposited rolls to ~30 % of the entire fleet. Considering the performance of the surfaced and new backup rolls, and correspondence of load distribution in the roughing stand, an optimal ratio of the surfaced and new rolls was selected. The Plant proposed, developed and realized the optimal route of the roll moving on the stands. Due to that the average operating life (in rolled stock tonnage) of the surfaced backup rolls of hot rolling mill 2000 is equal up to 85 % (by the Plant data) relative to new rolls produced by NKMP and UHMP.

Conclusions

During the research it was found that:

1. At multilayer surfacing of backup rolls formation of the transition zone from base metal to the working layer is determined by an optimum combination of the deposited layer composition and mode of each layer deposition. Substantiated selection of such a combination that allows for the surfacing method and mode, electrode composition and geometry, influences the degree of underlayer dilution by the base metal, and by the previous and next layers for the second and third layer. It allows preventing the hardness dips in the entire extent of the transition zone.

2. The proposed and realized scheme of formation of a multilayer composition, deposited by strip electrode on large-sized backup rolls for hot rolling, provides a smooth distribution of hardness by the deposited metal height.

3. Development of the technology of surfacing large-sized backup rolls, mastering the production of strip electrodes, and long-term operation of the surfaced rolls confirmed their ability to ensure a high level of surfaced roll operating life in rolled stock tonnage. Obtained experience of development and realization of the route of movement of the surfaced and new backup rolls in mill 2000 at the Cherepovets Metallurgical Plant should be further analyzed and disseminated.

1. Ryabtsev, I.A., Kondratiev, I.A., Vasiliev, V.G. et al. (2010) Investigation of structure and service properties of deposited metal for reconditioning and strengthening of rolling mill rolls. *The Paton Welding J.*, **7**, 12–15.
2. Balakleets, I.A., Filippov, V.S., Shebanits, E.N. et al. (2012) Current trends in the manufacture and operation of rolls. *Metall i Lityo Ukrainy*, **2**, 50–54 [in Russian].
3. Gostev, K.A. (2008) Modern rolls at rolling mills 2000 of Cherepovetsky and Magnitogorsky Iron and Steel Works. *Metallurg*, **9**, 52–55 [in Russian].
4. Danilov, L.I., Skorokhvatov, N.B., Sobolev, V.F. et al. (2004) Increase of the service life of the back-up rolls of a 2000 hot strip mill at JSC «Severstal». *Chyornaya Metallurgiya*, **8**, 68–69 [in Russian].
5. Samotugin, S.S., Leshchinskiy, L.K., Mazur, V.A., Samotugina, Yu.S. (2013) *Tool materials. Properties and hardening*. Mariupol, PSTU [in Russian].
6. Gulakov, S.V., Nosovskiy, B.I. (2005) *Surfacing of working layer with the regulated distribution of properties*. Mariupol, PSTU [in Russian].
7. Leshchinskiy, L.K., Gulakov, S.V., Nosovskiy, B.I., Stepnov, K.K. (1977) Causes of fracture of the deposited working layer of back-up rolls. *Avtomatich. Svarka*, **3**, 19–23 [in Russian].
8. Kostin, V.A. (2012) Mathematical formulation of carbon equivalent as a criterion for evaluation of steel weldability. *The Paton Welding J.*, **8**, 11–16.
9. Leshchinsky, L.K., Samotugin, S.S., Pirch, I.I., Komar, V.I. (1990) *Plasma surface hardening*. Kiev, Tekhnika [in Russian].
10. Ryabtsev, I.A., Babinets, A.A., Gordan, G.N. et al. (2013) Structure of multilayer samples, simulating surfaced tools for hot deforming of metals. *The Paton Welding J.*, **9**, 41–45.
11. Gajvoronsky, A.A., Poznyakov, V.D., Markashova L.I. et al. (2012) Influence of deposited metal composition on structure and mechanical properties of the reconditioned railway wheels. *Ibid*., **8**, 16–22.
12. Leshchinsky, L.K., Ivanov, V.P., Maslov, A.A. (1997) *Strip electrode for hardfacing*. Pat. 2087589 RU, Int. Cl. B23K020/227 [in Russian].

Received 02.02.2021

https://doi.org/10.37434/tpwj2021.03.07

INVESTIGATION OF STRUCTURE, MECHANICAL AND THERMOPHYSICAL PROPERTIES OF ELECTRON BEAM MODIFIED WELDS ON COPPER PARTS OF LANCES

V.M. Nesterenkov[1], **V.I. Zagornikov**[1], **Yu.V. Orsa**[1], **S.D. Zabolotnyi**[2] and **A.S. Belyaev**[2]
[1]E.O. Paton Electric Welding Institute of the NAS of Ukraine
11 Kazymyr Malevych Str., 03150, Kyiv, Ukraine. E-mail: office@paton.kiev.ua
[2]V.M. Bakul Institute for Superhard Materials of the NAS of Ukraine
2, Avtozavodska Str., 04074, Kiev, Ukraine. E-mail: alcon@ism.kiev.ua

The study of real operating conditions of the lance for oxygen blasting shows that in its head part, located near reaction zones of the converter, high thermal stresses arise caused by nonuniform heating of different parts of the unit. The nozzles of the head are intensively cooled by water and oxygen, and the tip of the lance, on the contrary, is heated by thermal radiation of a liquid metal pool. Namely, thermal stresses along with mechanical loads (reaction of return effect from oxygen jets flowing from the nozzles) cause a premature destruction of the welds joining the lance nozzles with its tip. The need in developing electron beam welding of components of copper lances is predetermined by disadvantages of using traditional method of their welding — argon-arc method, which does not provide satisfactory properties of welded joints and their stability during operation of a product. The use of electron beam welding in the manufacture of lance heads for oxygen blasting allows increasing their service characteristics by alloying welding pool with the elements, having a deoxidizing effect on a liquid copper. At the same time, in order to increase the service life of lance heads, it is necessary to reduce the level of thermal stresses in them. The latter becomes possible if in terms of thermal conductivity the weld metal is as close as possible to the base metal. The paper presents the results of mechanical tests of electron beam welded joints produced on M1 copper using different alloying inserts. On the basis of studies of microstructure and character of fractures of the modified electron beam welds, the influence of alloying inserts on their operational properties was established. Together with the specialists from the ISM of the NASU, a procedure for conducting investigations on thermal conductivity of welded joints was developed and measurements of thermal conductivity coefficients for the joints produced on M1 copper by AAW and EBW methods using alloying inserts was performed. Computer simulation of the temperature field arising in the areas of welded joints in the conditions of operation of copper lances was also performed. 12 Ref., 1 Table, 8 Figures.

Keywords: electron beam welding, weld modification using alloying inserts, metallographic and factographic examinations, thermal conductivity, coefficient, porosity

Operating conditions of converter lances for oxygen blasting are much more rigid than those of blast furnace lances. A typical design of an oxygen blast lance body consisting of an outer head (*1*), an inner shell (*2*) and a central (*3*) and five side (*4*) nozzles is shown in Figure 1.

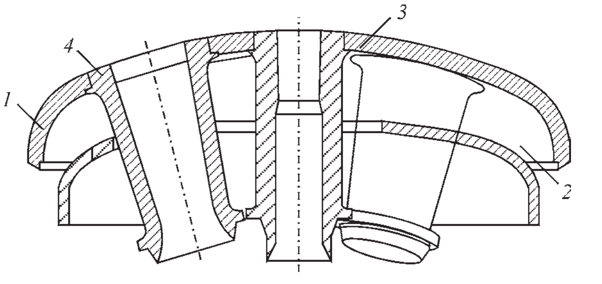

Figure 1. Typical design of body oxygen blast lance (see description in the text)

The nozzles of the head are intensively cooled by water and oxygen, and the tip of the lance, on the contrary, is heated by a thermal radiation of a liquid metal pool. Even its inner surface, which is well washed by water, can be heated up to 170 °C in the process of converter melting. The outer surface, facing the mirror of metal, is heated to a temperature of 400–500 °C and higher. Electron beam welding has a prospect of improving the operating characteristics of welded joints on copper [1–6]. However, such a weld defect as porosity does not allow realizing the advantages of this welding method quite effectively, because under the conditions of rigid temperature stresses and mechanical loads, under which the lance

V.M. Nesterenkov — htts://orcid/org/0000-0002-7973-1986, V.I. Zagornikov — htts://orcid/org/0000-0003-0456-173X,
Yu.V. Orsa — htts://orcid/org/0000-0002-1208-4171, S.D. Zabolotnyi — htts://orcid/org/0000-0003-1287-8454,
A.S. Belyaev — htts://orcid/org/0000-0002-7997-1509

head operates, the pores in the weld cause its premature fracture. In EBW of copper an intensive removal of gases proceeds, which do not have a time to be evolved from the metal of the welding pool, forming pores or concentrating in microcontinuities, which creates a high pressure and leads to crack initiation [1–8]. Among the possible causes of porosity in EBW of oxygen-free copper, the authors of [9, 10] mention evaporation of elements with a high vapor elasticity. Such a well-known metallurgical method of reducing porosity as refining remelting is not always effective in the case of welding, because it can cause excessive deformations and inner stresses in welded structures. Another metallurgical method to avoid the porosity consists in alloying welding pool with the elements that improve the solubility of gases in a liquid metal or bind them into stable compounds. In EBW of copper it is rational to carry out alloying of a welding pool by aluminium and titanium as they differ by a low vapour elasticity as compared to copper and have a deoxidizing effect on a liquid copper in the process of welding.

The aim of the work consisted in evaluation of strength and thermophysical properties of modified electron beam welded joints of copper lances.

Procedure of investigations. In order to reduce pore formation in welds, EBW of copper specimens with a thickness of 18 mm was performed using alloying inserts in the form of a thin (0.05 and 0.1 mm) foil. Welding of the specimens was performed in the EBW installation of type UL-209m, equipped with the ELA-60 power unit (60/60 kW). The structural-phase characteristics were studied using a set of experimental methods of modern metals science, including optical metallography (microscopes «Versamet-2» and «Neophot-32»), analytical scanning microscopy (SEM-515 of PHILIPS Company). The hardness of the phase components was measured in a microhardness tester M-400 of LECO Company, the load was 1 N.

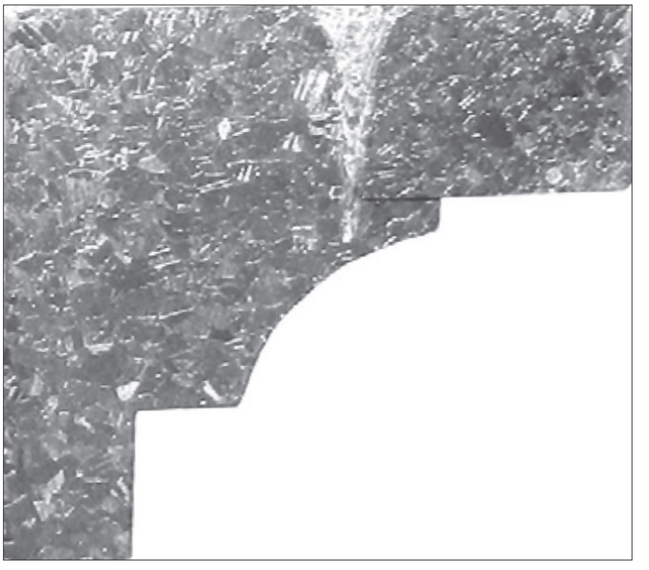

Figure 2. Welded joint with a thickness δ = 18 mm of lance and oxygen blasting. EBW conditions: U_p = 60 kV; I_b = 197 mA; v_w = = 7.5 mm/s; + ΔI_f = 5 mA, A_{circ} = 0.8 mm; L_{op} = 200 mm

Mechanical properties of welded joints such as a value of ultimate strength, proof strength and relative elongation of welded joints were determined at a room temperature on round specimens according to GOST 6996–66 type II, impact toughness was determined on the specimens with a Charpy-type notch. The structures of the arc weld and the modified electron beam welds were compared. In addition to metallographic examinations of the effect of alloying inserts on the microstructure of welded joints, their fractographic analysis was carried out. The examinations were ended in comparative measurements of a thermal conductivity coefficient of arc and modified electron beam welds. The measurement of thermal conductivity of welded joints was carried out with the participation of specialists and in the laboratory equipment of the ISM of the NASU.

Discussion of results. In the design of the welded unit, a «locking» joint is used, which allows preserving the advantage of electron beam welding and the possibility of removing root defects of the weld

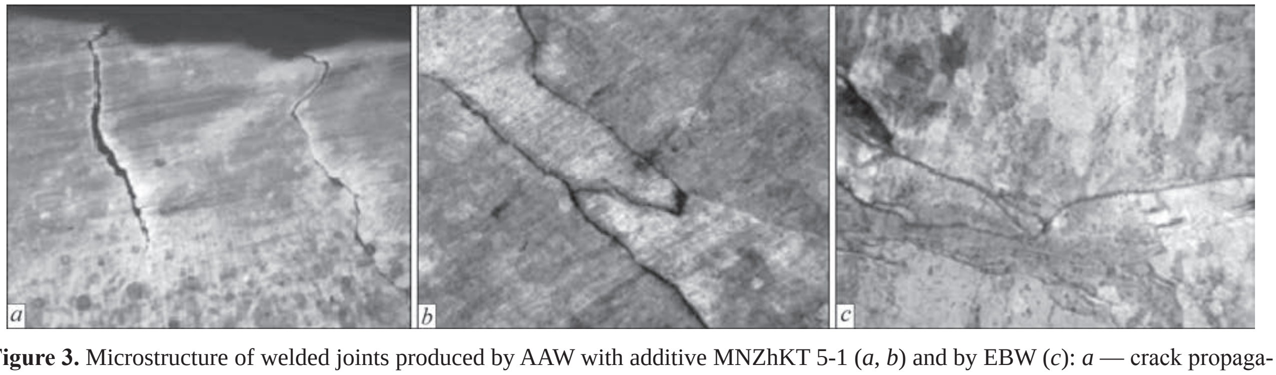

Figure 3. Microstructure of welded joints produced by AAW with additive MNZhKT 5-1 (*a*, *b*) and by EBW (*c*): *a* — crack propagation from the surface deep into the weld (×50); *b* — cracks in the central part of the weld (×200); *c* — thickening of grain boundaries in the root part of the weld, probably eutectics Cu + C_2O (×400)

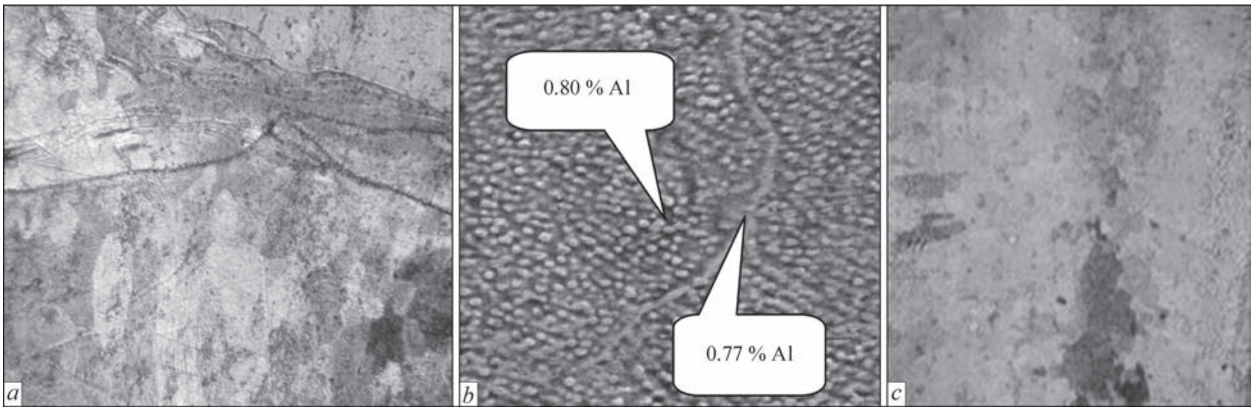

Figure 4. Microstructure of welded joint produced by EBW on M1 copper with AD-0 insert: *a* — weld root (×400); *b* — middle part of the weld (×2020); *c* — VT1-0, upper part of the weld (×100)

from the area of acting service loads. Previous studies (Kravchuk L.A. and Rusynik M.O., PWI) showed that using rigid modes of EBW, it is possibile to optimize the shape and quality of the weld. The obtained shape of the non-through weld is shown in Figure 2.

Electron beam welds and their HAZ differ favorably from arc welds in sizes and width and a smaller number of defects (Figure 3).

The grains in the metal of the argon-arc weld are large (mostly 500–700 μm, grains of 250 μm in size are more rare). At the same time, the structure of the electron beam weld consists of rounded grains that are by an order of value smaller and larger in the upper part of the weld (~ 70 μm), which are refined to ~ 48 μm at the weld root. The grain size in the near-weld zone and the base metal does not differ (on average 200–220 μm). The introduction of titanium and aluminium into the weld promotes producing of a fine-grained primary structure with a minimum width of intercrystalline boundaries. It is known that aluminium belongs to the elements, which are soluble in copper, its impurities in small concentrations can not be detected under a microscope, as far as they are included in a solid solution. With introduction of up to 1 % of aluminium (AD-0) to the weld, its structure almost does not change, but at the same time the hardness of the weld metal, which reaches *HV*–1030–1050 MPa increases. The heat-affected-zone does not have an expressed structure and represents large grains of irregular shape with a twin structure. As a result of metallographic examinations of the structure of welded joints produced on M1 copper alloy using alloying inserts from AD-0 alloy together with the positive effect of introduction of aluminium into the weld (significant reduction in the number and sizes of pores), microcracks were detected, located along the grain boundaries. This is most probably associated with the appearance of weak compounds with a low ductility, in this case eutectics or mixtures of $\alpha(Cu) + Cu_2O$ at the grain boundaries (Figure 4, *a*). In most cases, at a limited mutual solubility of copper and aluminium, it is extremely difficult to avoid the formation of stable intermetallic phases, which have high hardness and brittleness. To determine the chemical composition of these compounds, the method of scanning electron microscopy was used. During the quantitative analysis of the chemical composition of the welded joint metal, an increased (up to 2.5 %) aluminium content was detected. From the works of V.Ya. Agarkov and other authors [5, 6], it is known that a further increase in the aluminium content reduces the strength of the weld metal. Technological measures were taken to reduce the mass fraction of aluminium in the welded joint by reducing thickness of the alloying insert from 0.1 to 0.05 mm. Repeated analysis of the chemical composition of the thickened grain boundaries showed the aluminium content at the level of 0.56–0.77 % (Figure 4, *b*). Microcracks located along the grain boundaries were also not detected.

It is obvious that by changing the mass fraction of aluminium in the cast zone of the weld, it is possible to control the parameters of the primary structure and, as a consequence, the final microstructure of the weld metal. The use of VT1-0 titanium alloy inserts in EBW of copper also significantly affected the structure and hardness of the produced welds. The structure of the weld consists of a light matrix and a large number of dispersed precipitations (Figure 4, *c*). A number of precipitations in the center of the weld is greater than near the fusion line. The matrix represents a solid solution based on copper, and dispersed precipitations are obviously presented by copper titanites. On the specimens with VT1-0 titanium insert, the carried out chemical analysis (scanning electron microscopy) showed that the elemental composition in the depth of the weld does not change, as well as during aluminium alloying. The weld metal contains 0.89–1.23 % of Ti (the rest is copper).

An increase in microhardness in the weld root as compared to its middle part is observed. On all the

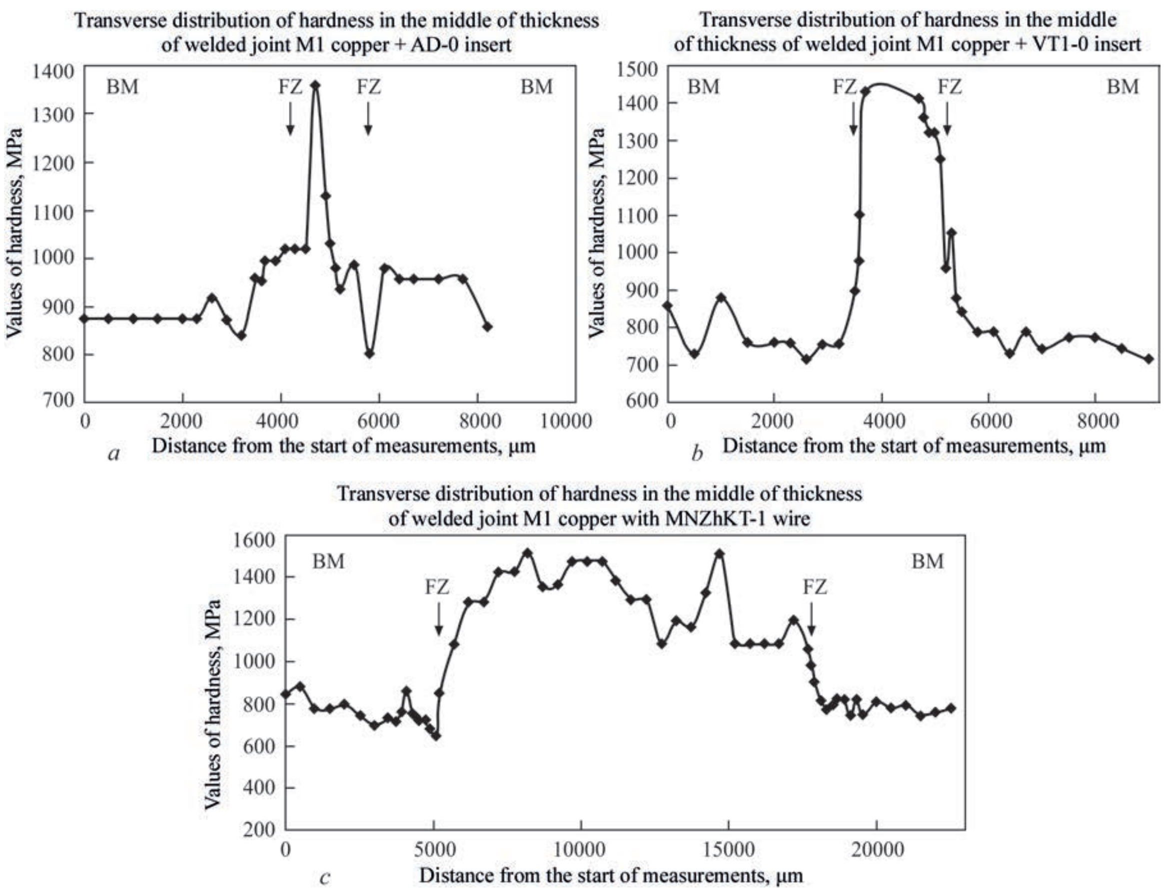

Figure 5. Comparative indices of sizes and level of microhardness: *a*, *b* — electron beam welds; *c* — argon-arc weld

specimens welded using alloying inserts, the hardness of the weld metal increases. The width of the softening areas has no noticeable propagation. It should be noted that the difference in hardness in the characteristic zones for both arc and electron beam welds is proportional. The same cannot be said about their width (Figure 5).

The tests of Mi-12 specimens on static tension at a temperature of +20 °C confirmed that the presence of alloying inserts with AD-0 and VT1-0 in the butt does not deteriorate the level of structural strength, which is typical of joints produced on M1 copper using EBW. The values of tensile and yield strengths of the welded joints and the base metal differ slightly from each other. The higher values of tearing strength of the welded joint modified by titanium can be explained by the degree of refinement and homogeneity of the grain in the cast zone, as well as the absence of defects. The tests of the metal of the welded joints on impact toughness also did not reveal significant deteriorations in the mechanical properties of the weld and HAZ metal as compared to the base metal (Figure 6).

Fractographic analysis was performed using a scanning electron microscope (SEM). In the area of defects located on the fusion boundary, the nature of the fracture is mixed with the degrees of chipping and tears along the grain boundaries and with a combination of micropores («pit» relief) and ridges of a nar-

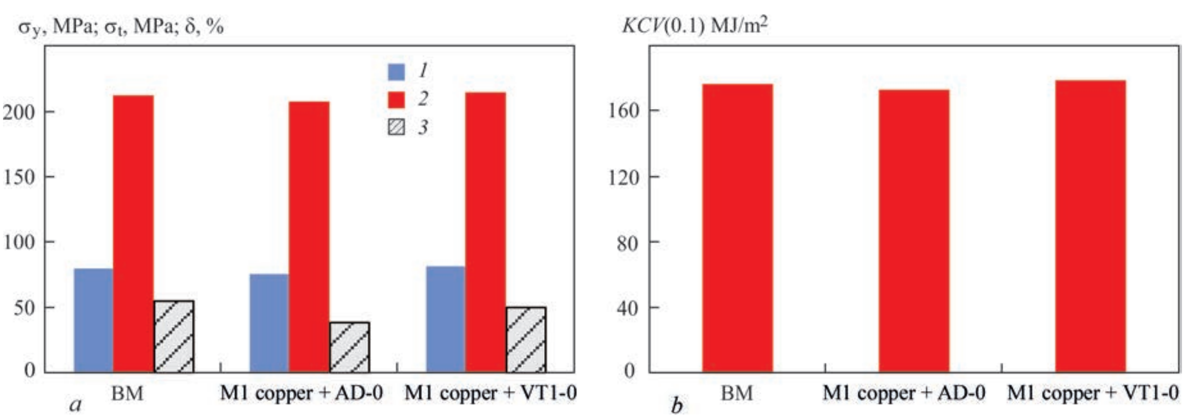

Figure 6. Testing of welded joints and base metal: *a* — static tension (Mi-12): *1* — σ_y, *2* — σ_t, *3* — δ; *b* — impact bending (Mi-50)

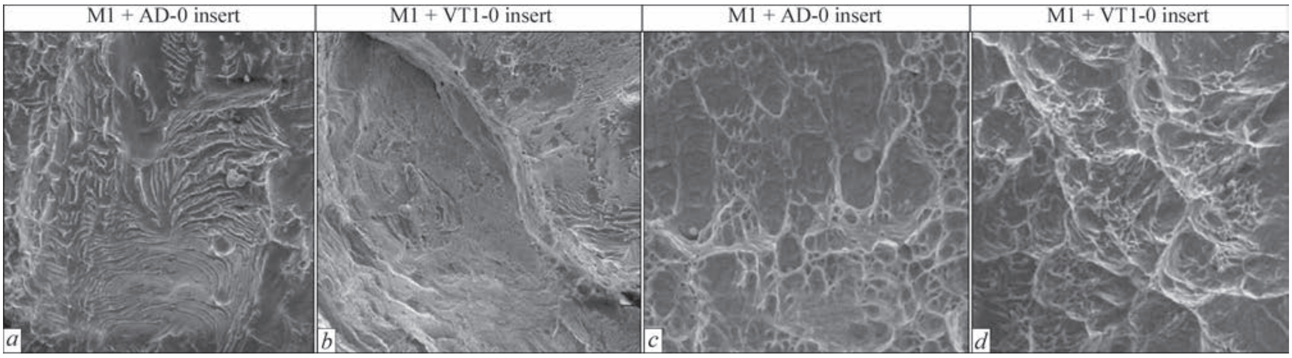

Figure 7. Microfractography of fracture fragments in different zones of welded joint, SEM; *a* — zone of main propagation of Mi-50 cracks (×300); *b* — center of Mi-12 specimen (×300); *c* — zone of main propagation of Mi-50 cracks (×2020); *d* — zone of main propagation of Mi-50 cracks (×500)

row tear (Figure 7, *a*, *b*). The fracture surface has a tough nature of fracture with a length of 100–150 μm with pits of different sizes (1–15 μm). Inside the pits, the particles can be seen, on which the pores arised (Figure 7, *c*). On the specimens alloyed with aluminium, detailed studies showed that in the fracture of the specimens there are areas fractured by the mechanism, which has a lower energy intensity of the fracture as compared to a tough one. Namely, the latter is the cause for some decrease in the ultimate strength of the weld metal as compared to the ultimate strength of the base metal. The action of titanium has a more balanced effect on the structure of the weld metal during its modification, promotes the formation of a more homogeneous fine-crystalline structure and transfers the fracture area at a static loading of the specimens into the base metal. The type of fractures of impact specimens alloyed with titanium is characterized by a tough intragranular fracture in the area of the main crack propagation (Figure 7, *d*). Reduction in the grain sizes limits the microcrack by effective barriers — by the boundaries of grains and crystallites. As a result, the initiated microcrack remains within the subcritical dimensions or under the effect of external forces it changes its direction during the further propagation. Thus, the results of the work show the possibility of using fractographic analysis of all the zones of the welded joint as one of the tools of a complex analysis of their quality and strength.

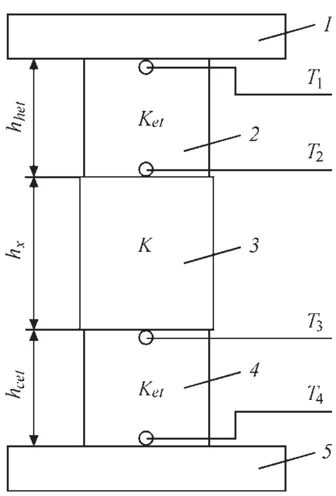

Figure 8. Scheme of measuring thermal conductivity with two reference specimens (see description *1–5* in the text)

An increase in strength and a decrease in the degree of softening of the welds and welded joints can be explained by refinement of the weld structure during welding using inserts of titanium and aluminium. The type of fracture in the near-weld zone and over the base metal is almost identical, which indicates a smooth transition from the zone of overheating to the base metal through a poorly expressed heat-affected-zone.

The study of real operating conditions of the lance for oxygen blasting shows that in its head part, located near the reaction zones of the converter with a temperature of 2700–2900 °C, large thermal stresses arise, caused by a nonuniform heating of different parts of the unit. The nozzles of the head are intensively cooled by water and oxygen, and the tip of the lance, on the contrary, is heated by thermal radiation of a liquid metal pool. Namely, thermal stresses along with mechanical loads (reaction of return effect from oxygen jets flowing from the nozzles) cause fracture of the welds joining the nozzles with the tip. Therefore, to increase the service life of the lance heads, it is necessary to minimize the temperature gradient between the nozzles and the tip. The latter is possible if in terms of thermal conductivity, the weld metal is close to the base metal.

Together with the experts of the ISM of the NASU a procedure of studying thermal conductivity was developed, which applied to the zones of welded joints produced on M1 copper using the AAW and EBW methods with alloying inserts and the design of a cylindrical specimen for measurements was developed.

When measuring the thermal conductivity of metals, a relative (comparative) method was used, which is based on the fact that the same amount of heat pass-

Values of thermal conductivity coefficients of weld metal

Method of welding	K_x, W/(m·K)
Body material of M1 lance	420.53
AAW using MNZhKT5-1 filler wire	181.78
EBW using alloying insert of AD-0 aluminium alloy with a thickness of 0.05 mm	366.60
EBW using alloying insert of VTI-0 titanium alloy with a thickness of 0.05 mm	197.98
Notes. Body material of M1 lance; h_{specimen} — 10 mm; d_{specimen} — $10^{\pm 0.1}$ mm.	

es through the specimen with already known thermal conductivity (reference), located in series with the studied specimen. Heat flux is calculated by the temperature gradient on the reference specimen [11]. As a rule, in the laboratory specialized equipment the scheme with two reference specimens, given in Figure 8, is used.

Between the specimen (*3*), the thermal conductivity of which should be determined and the heat source (*1*), the reference specimen with a known thermal conductivity (*2*) is placed. On the other side of the measured specimen, the second reference specimen (*4*) is placed, which is in contact with the refrigerator (*5*). The measurement error will be smaller, the better the contact between the contacting surfaces. The temperatures are measured using four thermocouples connected to the reference specimen and the measured specimens.

To minimize the contact resistance on all the surfaces of the references and the specimen a special thermal interface (metal alloy based on gallium) is deposited, which at a room temperature is in the state of a viscous fluid (paste), which moistens the contact surfaces. The computer monitoring system in real time records the indices of four thermocouples. The first thermocouple is located in a thin groove on the upper surface of the hot reference directly under the heater. The second thermocouple is located in a thin groove on the lower surface of the hot reference. The arithmetic mean of the readings of the first and second thermocouples is the temperature of the hot reference. The third and the fourth thermocouples are fixed in the grooves on the upper and lower surfaces of the cold reference, respectively. As in the previous case, the arithmetic mean of their readings is the temperature of the cold reference. The average value of readings of the second and the third thermocouples determines the temperature of the measured specimen. When determining the thermal conductivity of the test specimen, the heater temperature does not exceed 30 °C. The formula for the thermal conductivity coefficient K_x of the specimen with the height h_x and cross-sectional area S_x takes into account the presence of both references and the readings of four thermocouples:

$$K_x = \frac{K_{et} S_{et} h_x}{2S_x \left(T_2 - T_3\right)} \left(\frac{T_1 - T_2}{h_{het}} - \frac{T_3 - T_4}{h_{cet}}\right),$$

where h_{het} and h_{cet} is the height of hot and cold references, respectively; S_{et} is their cross-sectional area; K_{et} is the the thermal conductivity coefficient of the reference material.

The measurement takes place after the measuring system starts operating in the stationary mode, the value of the thermal conductivity coefficient of the specimen is averaged over four experiments. During the trial tests of the installation and the procedure on the reference specimens with a known thermal conductivity coefficient, the relative measurement error did not exceed 5 %.

The results of measurements of the thermal conductivity coefficient of M1 copper specimens with different types of welded joints according to the abovementioned formula are shown in Table.

The obtained measurement results were used during computer simulation of the temperature field, that arises in the area of the welded joint in the conditions of operation of copper lances. The results of calculations of the temperature difference in the center line of the weld and on the periphery of the calculation area showed a significant advantage of the joints produced by EBW with alloying of AD-0 aluminium in terms of maximum reduction of the temperature gradient between the nozzles and the tip of a real lance.

Conclusions

1. Results of carried out metallographic examinations showed the prospects for the use of alloying inserts in the manufacture of parts of copper components of lances using EBW.

2. Mechanical tests and factographic analysis of welded joints confirmed that the presence of AD-0 and VT1-0 inserts in the butt does not deteriorate the level of structural strength typical of electron beam joints produced on M1 copper.

3. In the root part of the produced welds, the chemical inhomogeneity inherent in EBW with a non-through penetration is noted. To remove probable root defects of a weld from the zone of acting operation-

al loads in the structure of copper lances, the use of «lock» joint is justified.

4. Along with the positive effect from the introduction of VTI-0 (significant reduction in the level of porosity at high mechanical values), it is unacceptable to recommend it as an alloying element in EBW of lance components because of a low thermal conductivity of the weld metal, commensurable with the argon arc weld (filler wire MNZhKT5-1).

1. Nazarenko, O.K., Kajdalov, A.A., Kovbasenko, S.N. et al. (1987) *Electron beam welding*. Kiev, Naukova Dumka [in Russian].
2. Agarkov, V.Ya., Trofi mova, K.G. (1983) Porosity of welds in electron beam welding of copper. In: Technology, organization of labour, production and monitoring. *Ser.: Tekhnologiya, Organizatsiya i Mekhanizatsiya Mekhanosborochnogo i Svarochnogo Proizvodstva*, **12**, 1–4 [in Russian].
3. Nazarenko, O.K., Agarkov, V.Ya., Ikonnikov, V.I. (1986) Influence of method of edge preparation on pore formation in weld during electron beam welding. *Avtomatich. Svarka*, **2**, 21–25 [in Russian].
4. Agarkov, V.Ya. (1982) Porosity in electron beam welds (Review). *Ibid*., **2**, 63–68 [in Russian].
5. Ilyushenko, V.M., Lukyanchenko, E.P. (2013) *Welding and surfacing of copper and alloys on its base*. Kiev, IAW [in Russian].
6. Zarechensky, A.V., Agarkov, V.Ya., Kolechko, A.A. et al. (1980) Electron beam welding of oxygen converter lance head. *Avtomatich. Svarka*, **10**, 68–69 [in Russian].
7. Stummer, M., Stütz, M., Aumayr, A., Enzinger, N. (2018) Electron beam welding of copper using plasma spraying for filler metal deposition. *Welding in the World*, **62**, 1341–1350. https://link.springer.com/article/10.1007/s40194-018-0637-z
8. Enzinger, N., Loidolt, P., Wiednig, C. et al. (2017) Electron beam welding of thick-walled copper components. *Sci. and Technol. of Welding and Joining*, 22(**2**), 127–132. DOI: https://doi.org/10.1080/13621718.2016.1204516
9. Kanigalpula, P.K.C., Jaypuria, S., Pratihar, D.K., Jha, M.N. (2018) Experimental investigations, input-output modeling, and optimization of spiking phenomenon in electron beam welding of ETP copper plates. *Measurement*, **129**, 302–318. DOI: https://doi.org/10.1016/j.measurement.2018.07.040
10. Kanigalpula, P.K.C., Chatterjee, A., Pratihar, D.K. et al. (2015) Effects of electron beam welding on microstructure, microhardness, and electrical conductivity of Cu–Cr–Zr alloy plates. *J. of Mater. Eng. and Performance*, **24**, 4681–4690. https://link.springer.com/article/10.1007/s11665-015-1790-9
11. Volkov, D.P., Korablev, V.A., Zarichnyak, Yu.P. (2006) *Study guides for laboratory works on course «Thermophysical properties of substances»*. St.-Petersburg, GU ITMO [in Russian].
12. (1986) *Theory of welding processes*. Ed. by V.V. Frolov. Moscow, Mashinostroenie [in Russian].

Received 15.02.2021

https://doi.org/10.37434/tpwj2021.03.08

HIGH-EFFICIENT SOURCES FOR ARC WELDING ON THE BASE OF CAPACITIVE ENERGY STORAGE SYSTEMS

O.E. Korotynskyi, M.I. Skopyuk and **I.V. Vertetska**
E.O. Paton Electric Welding Institute of the NAS of Ukraine
11 Kazymyr Malevych Str., 03150, Kyiv, Ukraine. E-mail: office@paton.kiev.ua

A new class of high-efficient arc welding equipment is proposed, which is based on wide application of capacitive energy storage systems, in which high-capacity capacitors with a double electric layer are used as such storages. The paper is a study of the structure of sources, which are based on switching-modulation conversion of welding current. Procedures of signal conversion in the proposed sources, using the charge transfer method are analyzed in detail. Analysis of dynamic characteristics of this type of sources was performed, and basic equations were derived, which characterize different types of capacitive welding current converters. 13 Ref., 1 Table, 4 Figures.

K e y w o r d s : arc welding, capacitive energy storage system, double electric layer capacitor, charge transfer method, topological structures of the sources, step-down type converter

Modern approaches in designing of welding power sources are based on the following requirements to their parameters: high energy efficiency of welding current conversion, required level of operational reliability, increased generated specific capacity (determined in relation to weight or volume), power factor of not lower than 0.9, high dynamic parameters in the mode of current/voltage stabilization. It is naturally, that the abovementioned requirements can be satisfied only by high-frequency welding converters [1]. But transfer to the conversion of welding current energy at a high frequency raises the problem of electromagnetic compatibility (EMC) [2]. Meeting all these requirements leads to additional costs on hardware, which to some extent reduce the economic efficiency of high-frequency welding equipment.

Basically, modern welding inverters are designed according to the double conversion circuit, when the mains voltage is rectified, smoothed by a capacitive filter and then supplied to the input of the DC/DC converter unit. In capacity of the latter, three types of circuits are mainly used: full-bridge, half-bridge inverters, and most often in the sources of up to 200 A – a single-step bridge inverter, which in the technical literature is often called an «oblique» bridge (OB). The prospects of this structure of welding inverter are indisputable. That is why a number of works [3] devoted to the search for new circuit solutions, as well as to increase the parameters of energy efficiency are devoted to its further investigations and improvement. A particular interest of the works in this area is paid to the dual OB [4], which in terms of technical and economic indices competes even among bridge converters with a phase control.

An important role in welding inverters is played by dynamic parameters of power keys, which mainly determine the losses on switching. Namely these losses limit the switching frequency, to increase which it is necessary to use resonant or «softly» switched technologies [5].

One of the ways to increase the energy efficiency of inverter welding equipment is elimination of a high-capacity filter capacitor in the rectifier circuit and transfer from a double energy conversion to a direct one. As is shown in [6], in case of excluding the function of input voltage rectification, it is possible to obtain high parameters of efficiency (EF) and power factors (PF) of the welding inverter. However, it will not be possible to get rid of a low-frequency transformer. And this causes deterioration of mass and size parameters of the device.

The authors of [7] showed that elimination of this drawback is possible by transfer to sources with a three-phase input. Here the principle of direct conversion of a three-phase voltage of industrial frequency into a high-frequency voltage is realized, which will then be converted in the same way as it is realized in the circuits of conventional welding inverters. However, here additional difficulties associated with the need in using bidirectional keys arise. And this leads to doubling a number of switching elements and circuits of their control, which ultimately reduces the economic indices of such sources.

One more direction in the creation of high-efficient welding equipment is resonance technologies [8]. They are based on a wide range of different types of inductive-capacitive converters (ICC), the circuitry of which is based on a wide range of elements of power electronics. These can be simply resonant LC circuits [9], inducons [10] operating in a wide range of frequencies. It is also necessary to note high-frequency welding converters designed on the base of artificial long lines (ALL) [11], in which EF of up to 90 % is achieved.

Despite such a large number of technical solutions in the field of welding current converters, the search for new methods of manufacturing sources continues. One of the prospective areas is creation of sources, in which inductive energy storages are replaced by capacitive ones. Naturally, a simple replacement is impossible here: it is necessary to develop new circuit solutions that would allow using the functionality of capacitive energy storages (CES) in a full extent. This class of noninductive converters should have the following properties:

- change the polarity of the input voltage;
- increase or decrease its level in accordance with the specified conversion factor;
- carry out the mode of galvanic isolation if necessary.

All these procedures can be realized in switching-modulation devices, when the accumulated charge in accordance with the conversion determined by the law (inversion, summation, multiplication, etc.) is transferred from one capacitor to another. Therefore, this type of sources can be called converters with charge transfer (CCT). The success of their practical realization is primarily associated with achievements in the field of creating powerful electric energy storage devices — supercapacitors (SC) [12], which are characterized by a high quality factor. This provides their increased energy efficiency. In this regard, the

Number	Circuit schemes of switching-modulation converters	Time diagrams
1	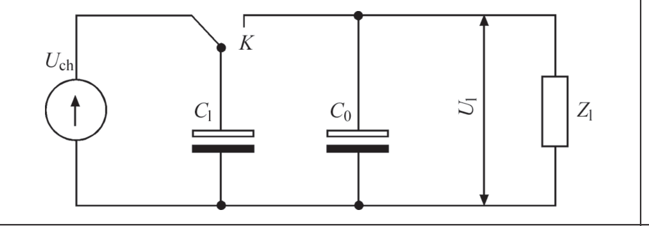	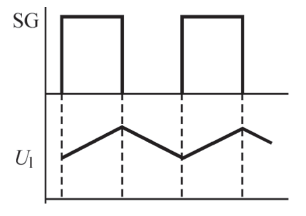
2	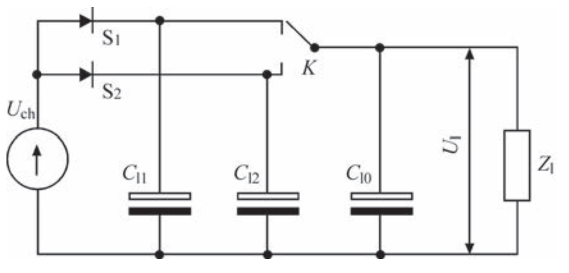	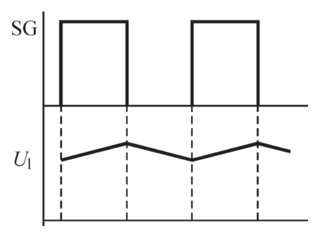
3	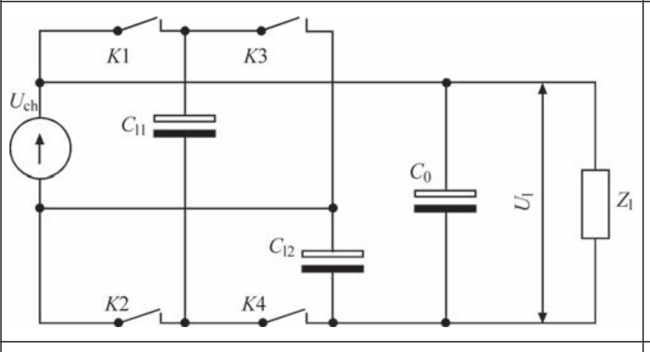	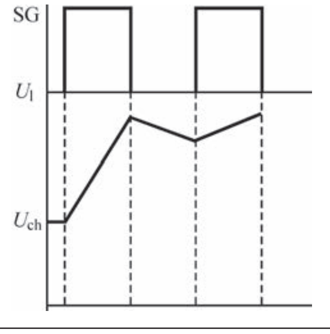
4	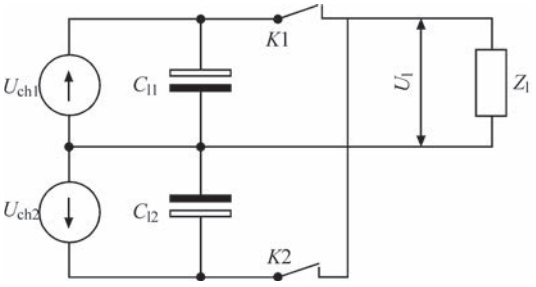	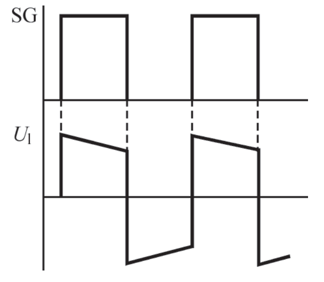

1 — switching-modulation converter (SMC) on the base of conventional circuit of a «flying» capacitor; 2 — SMC on the base of circuit of a two-step «flying» capacitor; 3 — SMC in the mode of voltage doubling; 4 — SMC in the mode of alternating voltage formation.

problem of using capacitive storage systems in creation of sources for arc welding is certainly relevant.

Until now, in welding SC have been used exclusively for pulsed technologies such as resistance spot welding, welding of studs, press welding using magnetically-impelled arc [13], etc. Here, SC was functionally used to form a powerful current pulse in the range of 0.5–10 kA in a single cycle of welding. At present, the experience of using SC in continuous arc welding modes is currently absent. The proposed work is the first attempt to implement this idea in relation to arc welding processes.

Let us consider some of the possible variants of CCT circuits given in Table, on the base of which it is possible to design equipment for arc welding. The circuit 1 represents a converter of type «flying» capacitor, where the storage capacitor [14], preliminary charged to the voltage U_{ch} is discharged with a help of the key K to the capacitor C_0. The latter is used as a power source of the load Z_l. As follows from the time diagram, the voltage on the load U_l is ripple, the level of which is determined by the frequency of the step generator (SG).

A significant reducing of their value is possible by using the circuit 2, which represents a double-step «flying» capacitor. In this circuit, the charge-discharge processes occur in an antiphase. Therefore, the value of voltage ripple on the load can be easily reduced to 1 %. However, the price for this advantage will be installation of additional capacitor C_{l2}.

The converter, designed in accordance with the circuit 3, provides a mode of doubling the voltage on the load. This occurs as follows: in the first step (keys $K1$, $K2$ are closed, and $K3$, $K4$ are open), the charge C_{l1} occurs to the voltage U_{ch}. Then, in the second step (keys $K1$, $K2$ are open, and $K3$, $K4$ are closed), the voltage is transferred to the storage system C_l with a change in polarity. Since the device is designed in such a way that this voltage and U_{ch} are summed, then on the load a double voltage ($U_l = 2U_{ch}$) will act. It is easy to see that the device designed according to this circuit is advisable to be used to create battery welding sources. This is especially prospective for military transport systems, where 24 V batteries are used.

The circuit 4 can be recommended for creating alternating current welding sources on its base. It consists of two charging devices, which form the voltages U_{ch1}, and U_{ch2} equal in amplitude, but opposite in sign, two storage systems C_{l1} and C_{l2}, as well as two keys $K1$, $K2$, which are switched on in an antiphase. When the key $K1$ is closed, a positive half-wave is formed, and when the key $K2$ is closed, a negative half-wave is formed. A distinctive feature of such drivers is the fact that without changing the circuit elements at all

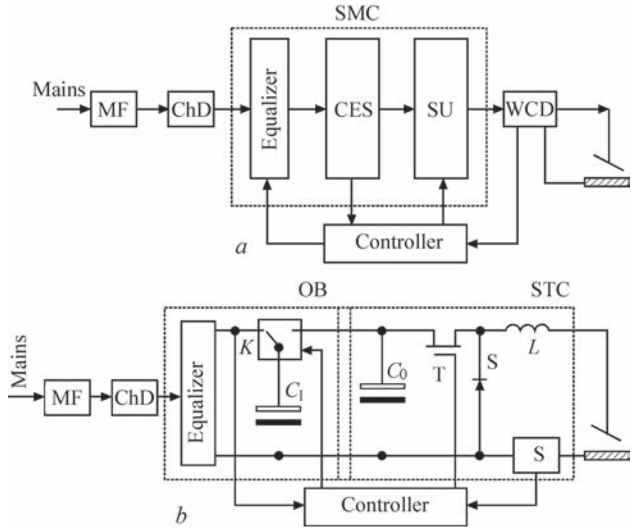

Figure 1. Circuit scheme of the source, that realizes the method of charge transfer (*a*), example of circuit realization of the source, based on a «flying» capacitor and SMC (*b*)

it is possible to adjust the frequency of the voltage supplying the arc in a wide range.

The structural and functional circuit of the source with the energy storage system on SC is shown in Figure 1, *a*. It consists of mains filter (MF), the primary purpose of which is to reduce the level of interferences generated in the mains. The MF output is connected to the charging device (ChD), as any type of direct current converter and also an autonomous power sources, such as batteries, flywheel capacitors, mini-power plants, etc. can be used. The voltage from the output of ChD is then supplied to SMC, which includes an equalizer. Its main purpose is to optimize the charge of CES elements. The switching unit (SU) performs the necessary procedures of an energy flow conversion in accordance with the algorithms specified by the controller. Thus, the obtained voltage is supplied to the input of the welding current driver (WCD), which provides the required volt-ampere characteristic (VAC) for the selected welding method.

An example of practical implementation of the described approach in creation of welding source is shown in Figure 1, *b*. In this device, as SMC, the circuit 1 (mode of «flying» capacitor), designed on the key K and the storage capacitor C_l is used. Then the charge accumulated on it is partially transferred to the capacitor C_0, which is a part of WCD, designed on the base of a step-down type converter (STC), which is known to be one of the most energy-efficient units in the field of power conversion technology.

The formation of the required VAC in accordance with the selected welding method is carried out due to the action of the feedback circuit, which is set by the signals of the current sensor (CS). As a result of action of these signals two control commands are synchro-

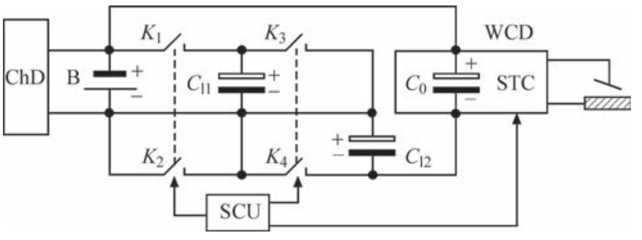

Figure 2. Battery power source

nously formed, which determine the time modes of operation of the key K and the transistor switch (TS) of the converter.

To create battery welding sources, the use of SMC is quite prospective. One of the possible variants of such a device is shown in Figure 2.

Procedurally, the conversion of energy flow occurs in the following order. In the first cycle, with the help of the closed keys $K1$ and $K2$, the storage system C_{l1} is charged from the battery (B). Then in the second phase, the keys $K1$ and $K2$ are opened and the keys $K3$ and $K4$ are closed. In this case, a part of the charge is transferred to the storage system C_{l2}, charging it to the voltage of the battery (B), but of a reverse polarity. As a result, this voltage is summed with the voltage of the battery and we obtain its double value. When the battery with $U = 24$ V is used, the total voltage acting on the storage systems C_0, amounts to 48 V. This is absolutely sufficient to power the STC converter, which is included in the WCD unit. All the described procedures of welding current conversion are realized by the switching control unit (SCU) of the keys, which are a part of SMC, and also the STC switch.

The advantage of this circuit of the battery source as compared to the known [15] is that due to the key decoupling of the battery circuit and the welding circuit, short-circuit currents in the arc do not lead to degradation of the battery, which took place during a direct switching into the welding circuit.

One more interesting technical solution in this class of devices is a source of alternating current for arc welding, in which it is simply enough to change the frequency in a very wide range. And most importantly, in this case the mode of frequency modulation (FM) of the welding current can be applied, which is almost impossible to realize in the conventional circuits of sources. Therefore, the technological properties associated with such a mode of FM have not been studied before.

The circuit scheme of such a source is shown in Figure 3, *a*. It consists of two charging devices ChD1 and ChD2, which form the voltage of positive and negative polarity U_1 and U_2. Therefore, the storage systems C_{l1} and C_{l2} are in the mode of a continuous charge. The voltage on them is periodically connected to WCD, which represents an inductive-capacitive converter (series resonant circuit), which, as is known [8], provides a high stability of welding arc burning.

The frequency of welding current is determined by the frequency selection switch (FSS). Depending on different settings of the circuit L_1, C_1 or L_2, C_2, it is set by the controller software, which controls the switching modes of the keys K_1, K_2 and FSS. The results of the experiments of the source verification in the mode $f = 1.41$ kHz are shown in Figure 3, *b*. The curve *1* is the arc voltage, the curve *2* is the welding current, the amplitude of which $I_w = 180$ A.

Let us consider the energy issues that arise when designing CCT sources. We shall assume that the state of the circuit before closing the key K (Figure 4, *a*) is as follows: C_1 and C_0 are charged. Moreover, $U_m > U_d$. Then at the moment of switching, it is possible to write down:

$$U_m = I(t)r + U_d. \tag{1}$$

If we pass to the charge shape, then (1) can be represented as:

$$-\frac{q_1}{C_1} + \frac{q_0}{C_0} + I(t)r = 0, \tag{2}$$

where $I(t)$ is the current in the circuit; q_1 and q_0 are the charges of the storage systems C_1 and C_0.

If we differentiate (2) in time, we obtain:

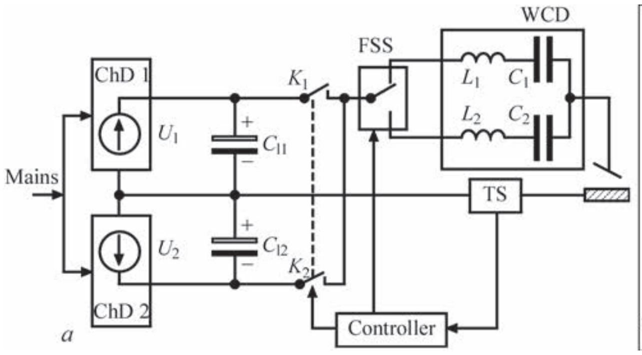

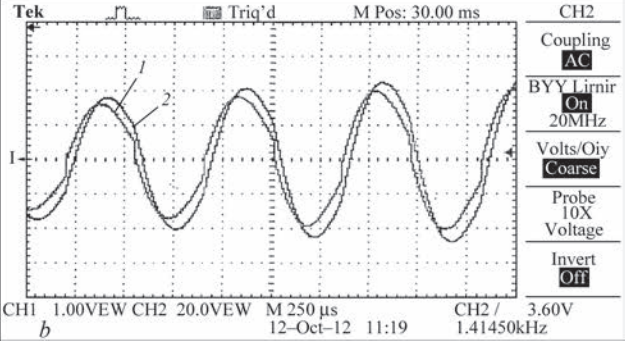

Figure 3. Circuit scheme of ac source (*a*), oscillogram of voltage (*1*) and current (*2*) (*b*)

$$-\frac{1}{C_1}\frac{dq_1}{dt}+\frac{1}{C_0}\frac{dq_0}{dt}+r\frac{dI(t)}{dt}=0. \quad (3)$$

Taken into account the fact that based on the law of charge conservation, current in the circuit is equal to:

$$I(t)=-\frac{1}{C_1}\frac{dq_1}{dt}=\frac{1}{C_0}\frac{dq_0}{dt},$$

(3) can be represented as:

$$\left(\frac{1}{C_1}+\frac{1}{C_0}\right)I(t)+r\frac{dI(t)}{dt}=0. \quad (4)$$

As is known from [16], the solution of equation (4) will be the function

$$I(t)=I(0)\exp\left(-\frac{t}{\tau}\right), \quad (5)$$

where $I(t)$ is the current at the moment of switching; $\tau=r\frac{C_1C_0}{C_1+C_0}$ is the time constant of the discharge circuit.

If we determine $I(t)$ according to the initial values of $U_m(0)$ and $U_d(0)$, it can be written:

$$I(t)=\frac{U_m(0)-U_d(0)}{R}\exp\left(-\frac{t}{\tau}\right). \quad (6)$$

As we agreed, $U_m > U_d$. Therefore, the equations of the discharge C_1 and the charge C_0 in time can be represented by the following equations:

$$U_m(t)=U_m(0)-\frac{1}{C_1}\int_0^t I(t)\,dt = \\ =U_m(0)-\frac{I(0)}{C_1}\int_0^t \exp\left(-\frac{t}{\tau}\right)dt. \quad (7)$$

Taken into account the fact that

$$I(0)=\frac{[U_m(0)-U_d(0)]}{};$$

$$U_m(t)=U_m(0)-\frac{\left[U_m(0)-U_d(0)\right]C_0}{C_1+C_0}\times \\ \times\left[1-\exp\left(-\frac{t}{\tau}\right)\right] \quad (8)$$

similarly, the expression for the voltage on $C_0 - U_d(t)$ can be represented

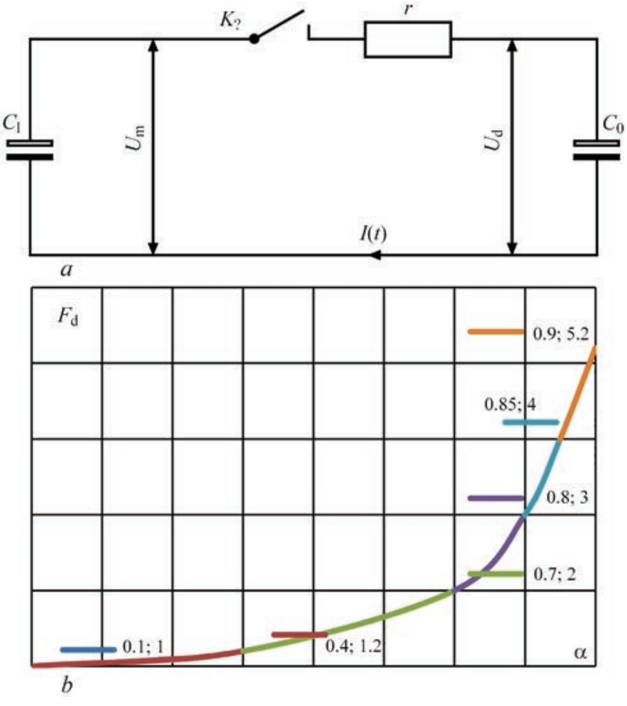

Figure 4. Circuit scheme of storage system discharge (*a*) and function of discharge F_d (*b*)

$$U_d(t)=U_d(0)-\frac{\left[U_m(0)-U_d(0)\right]C_0}{C_1+C_0}\times \\ \times\left[1-\exp\left(\frac{t}{\tau}\right)\right]. \quad (9)$$

The abovementioned formulas (6–9) fully describe the processes of the charge transfer in the sources with SMC.

The subsequent transfer of energy to the load (arc) occurs by the transfer of the charge, which is formed by the storage system C_0 during some time Δt. In terms of power, this can be described by the following formula:

$$\Delta P(t)=C_0/2\left(U_1^2-U_2^2\right), \quad (10)$$

where U_1 and U_2 are the voltage of the charged and partially discharged C_0.

Let us denote $U_2 = \alpha U_1$ where α is the coefficient that characterizes the degree of discharge of the storage system C_0. Then (10) can be represented by the following expression:

$$\Delta P(t)=\frac{C_0}{2}U_1\left(1-\alpha^2\right). \quad (11)$$

From (11) the value of the storage system C_0 capacity can be determined as:

$$C_0=\frac{2\Delta P(t)}{U_1^2}\frac{1}{1-\alpha^2}=\frac{2\Delta P(t)}{U_1^2}F_d, \quad (12)$$

where $F_d = \frac{1}{(1-\alpha^2)}$ will be called a discharge function. It describes the degree of the charge transfer into the welding circuit. Its diagram is shown in Figure 4, *b*. Using the formula (12), it is possible to determine the storage system capacity for a set power of the welding current source.

In order to functionally link all the processes that take place in the sources with the charge transfer, we will use the following considerations. As is known, on the one hand the charge can be represented by the formula $q = C_1U$, on the other hand $q = It$, therefore:

$$C_1U = It. \tag{13}$$

Assuming that the process of energy flow conversion occurs every period, i.e. $t = 1/t$, then (13) can be converted to the form:

$$I / UC_1 f = 1. \tag{14}$$

The expression (14) describes the basic regularities, occurring in this class of sources for arc welding. It links the electrical (U, I) and time (t) characteristics with the storage system (C_1) capacity, and can serve as a base for calculating the parameters of CCT.

Further, the calculations performed in accordance with (14) will be adapted for different topological structures of inverter welding current converters, in which it is rational to use storage systems for realization of the charge transfer method. In our opinion, such an approach is especially prospective for calculations of step-down type converters.

Conclusions

New topological structures of power sources for arc welding, designed on the base of capacitive energy storages, are proposed.

Using the methods of the theory of switching-modulation converters, the theoretical substantiation of the work of this class of sources was carried out, and also the basic analytical expressions, describing the operation of such structures were obtained.

Based on the offered approaches, the working model of an alternating current source, providing a wide range of frequencies of output voltage regulation, was created and experimentally investigated.

It is shown, that an increase in energy efficiency of this class of equipment is achieved due to a high quality factor of capacitive energy storage systems, designed on the base of capacitors with a double electric layer.

1. Lebedev, V.K. (1995) Trends of development of power sources for arc welding. *Avtomatich. Svarka*, **5**, 3–6 [in Russian].
2. Pentegov, I.V., Rymar, S.V., Zhernosekov, A.M., Sidorets, V.N. (2012) Electromagnetic compatibility of power sources of welding arc. *Elektrotekhnika i Elektromechanika*, **3**, 34–38 [in Russian].
3. Borisov, D.A. (2010) *Dynamic processes in power sources for welding at high-frequency alternating current welding*: Syn. of Thesis for Cand. of Tech. Sci. Degree. Saratov [in Russian].
4. Paton, B.E., Korotynsky, O.E., Skopyuk, M.I., Drachenko, M.P. (2009) *Hybrid device for conversion of dc energy at input to ac energy at output*. Ukraine Pat. 41218 [in Ukrainian].
5. Rudyk, S.D., Turchaninov, V.E., Florentsev, S.N. (1999) High-power single-step converter of dc voltage with «soft» commutation of power key. *Elektrotekhnika*, **4**, 55–58 [in Russian].
6. Rudyk, S.D., Turchaninov, V.E., Florentsev, S.N. (1998) Prospective welding current sources. *Ibid*., **7**, 8–13 [in Russian].
7. Burlaka, V.V., Gulikov, V.V. (2012) Three-phase inverter power source with direct conversion and increased power factor. *The Paton Welding J.*, **7**, 35–37.
8. Korotynsky, A.E. (2007) *High-efficient power sources for arc welding based on inductance-capacitance converters*: Syn. of Thesis for Dr. of Tech. Sci. Degree. Kiev [in Russian].
9. Lebedev, V.K., Korotynsky, A.E. (1994) Ac arc in the circuit with inductance and capacitance connected in series. *Avtomatich. Svarka*, **12**, 47–48 [in Russian].
10. Milyakh, A.N., Volkov, I.V. (1974) *Constant current systems based on inductance-capacitance converters*. Kiev, Naukova Dumka [in Russian].
11. Korotynsky, A.E. (1999) Peculiarities of operation of high frequency welding inverters on the basis of an artificial long line. *Avtomatich. Svarka*, **1**, 76–77.
12. *Mark Gebbia* (2013) Dual nature of supercapacitors. *Elektronnye Komponenty*, **6**, 104–107.
13. Korotynsky, A.E., Drachenko, N.P., Shapka, V.A. (2014) Peculiarities of application of supercapacitors in devices for pulse welding technologies. *The Paton Welding J*., **9**, 34–38.
14. Korotynsky, A.E. (2002) State-of-the-art, tendencies and prospects of development of high-frequency welding converters (Review). *Ibid*., **7**, 44–50.
15. Paton, B.E., Dudko, D.A., Korotynsky, A.E., Kisterskaya, L.D. *Autonomous device for arc welding*. Ukraine Pat. 23804 A. Publ. 31.08.98 [in Russian].
16. Pentegov, I.V. (1982) *Fundamentals of theory of charging circuits of capacitive energy storage systems*. Kiev, Naukova Dumka [in Russian].

Received 12.02.2021